N O T I C E

NASA TECHNICAL MEMORANDUM

NASA TM-75753

LEE SIDE FLOW FOR SLENDER DELTA WINGS
OF FINITE THICKNESS

Joachim Szodruch

NATIONAL AERONAUTICS AND SPACE ADMINISTRATION
WASHINGTON, D. C. 20546   MARCH 1980

1. Report No. NASA TM-75753	2. Government Accession No.	3. Recipient's Catalog No.
4. Title and Subtitle LEE SIDE FLOW FOR SLENDER DELTA WINGS OF FINITE THICKNESS		5. Report Date March 1980
		6. Performing Organization Code
7. Author(s)		8. Performing Organization Report No.
		10. Work Unit No.
9. Performing Organization Name and Address .SCITRAN Box 5456 Santa Barbara, CA 93108		11. Contract or Grant No. NASW-3198
		13. Type of Report and Period Covered Translation
12. Sponsoring Agency Name and Address National Aeronautics and Space Administration Washington, D.C. 20546		14. Sponsoring Agency Code

15. Supplementary Notes

Translation of "Leeseiten-stroemung bei schlanken Deltafluegeln endlicher Dicke",Technische Univ., Berlin (West Germany), Inst. fuer Luft und Raumfahrt, Report ILR 23, 1977, 150 pages.

16. Abstract

An experimental and theoretical investigation was carried out to determine the lee side flow field over delta wings at supersonic speeds. A theoretical method to describe the flow field is described, where boundary conditions as a result of the experimental study are needed. The computed flow field with shock-induced separation is satisfactory.

17. Key Words (Selected by Author(s))	18. Distribution Statement Unclassified – Unlimited	
19. Security Classif. (of this report) Unclassified	20. Security Classif. (of this page) Unclassified	21. No. of Pages 161	22.

LEE SIDE FLOW FOR SLENDER DELTA WINGS
OF FINITE THICKNESS[*]

Joachim Szodruch

Summary

An experimental and theoretical investigation was carried
out to determine the lee side flow field over delta wings at
supersonic speeds. The experiments were performed with models
of the same slenderness s/l = 0.3 but different cross-section
shape. The known types of flow, separated by the Stanbrook-
Squire boundary into leading edge and shock-induced separation
have been verified. However, further types of flow exist and a
detailed survey of the boundaries is necessary.

The influence of the cross-sectional shape on the lee side
flow is discussed for the thick wing inside the region of shock-
induced separation. In detail parameters like wedge angle at the
center line, angle between upper and lower surface as well as the
lower side shape are considered.

A theoretical method to describe the flow field is lined out,
where boundary conditions as a result of the experimental study
are needed. The computed flow field with shock-induced separation
is satisfactory. .

[**]Numbers in the margin indicate pagination of original foreign
text.

a	speed of sound
a b c	magnitudes of the components of the vector $\vec{U_2}$
d e	magnitudes of the components of the vector $\vec{U_3}$
C	thickness parameter
c_p	pressure coefficient
F	base area of delta wing
F_{Diff}	diffusion cross-section area
F_{Mess}	test section cross-section area
h	height of delta wing
K	iteration factor
l	wing length
M	Mach number
M*	critical Mach number
p	static pressure
P	total pressure
Re	Reynolds number
s	half span width
T	temperature
V	volume
X Y Z	aerodynamic coordinate system
x y z	body fixed coordinate system
$\bar{x}$ $\bar{y}$ $\bar{z}$	body fixed coordinate system fixed at the leading edge shock

2

$\left.\begin{array}{l}\vec{a}\\\vec{s}\end{array}\right\}$	tangential plane vectors
$\vec{\mathscr{C}}$	normal vector
$\left.\begin{array}{l}\vec{i}\\\vec{j}\\\vec{k}\end{array}\right\}$	unit vectors in aerodynamic system
$\left.\begin{array}{l}\vec{l}\\\vec{m}\\\vec{n}\end{array}\right\}$	unit vectors in body fixed coordinate system
$\vec{M}$	Mach number vector
$\vec{U}$	velocity vector

α	angle of attack
γ	trace angle of internal shock
δ^{*}	displacement boundary layer thickness
ε	density ratio over shock
ϑ_{κ}	wedge angle
Θ	form angle (wedge angle for delta wing in the symmetry plane)
κ	ratio of specific heats
Λ	sweep angle
μ	Mach cone angle
ν	Prandtl-Meyer angle
τ	volume parameter
Φ	inclination angle of shock
ϕ	local flow direction
$\varphi_{s\ell}$	separation line angle
Ψ	leading edge angle
Ω	transformed semi-span

Subscripts

A	values in the region of the nondetached flow
CL	symmetry plane values

e	values perpendicular to internal shock
K	values for wake wedges
N	normal component values
p	values behind perpendicular shock (Pitot values)
PZ	value of the primary vortex center
S	leading edge shock values
SO	values for zero intensity of internal shock
SZ	values of the secondary vortex center
T	tangential component values
∞	incident flow values
O	rest variables
1	values upstream of the leading edge shock
2	values in the expansion region
3	values downstream of the internal shock
4	values in the central region (internal expansion)

1. Introduction

The aerodynamic design of hypersonic aircraft led to slender configurations with delta-shape plan form, strong sweepback of the leading edges and a substantial relative thickness. The aerodynamic properties of such aircraft shapes are determined primarily in the case of supersonic flight by the flow conditions along the lower side. The lift is produced almost exclusively by the overpressure along the underside. Suction forces along the upper side (lee side) have a very small influence. This makes it understandable why only a small degree of attention was given to the flow field along the lee side of delta wings in the supersonic range. There were only a few surprising results in the determination of the aerodynamic heating on the top side of reentry bodies and space shuttle models which led to work on lee side flow. Measurements in the wind tunnel and in free flight tests [1-8] showed that

the temperature values on the upper side of a reentry body have a maximum value for zero incidence angle ($\alpha = 0^{\circ}$) at the tip. Along the symmetry plane, the temperature decreases according to a hyperbolic law to the trailing edge. However, completely different conditions exist when the body has an incidence angle. For example, if the incidence angle is $\alpha = 20^{\circ}$, there is strong temperature drop immediately behind the tip, which is followed by a temperature increase. The maximum value corresponding to $\alpha = 0^{\circ}$ is then exceeded. Within 20% of the wing chord, temperature differences of $\Delta T = 250^{\circ}$ K have been measured. Depending on the incident flow conditions, several temperature peaks could be determined.

The results contrast to a certain extent with conventional ideas about the flow conditions along the lee side of delta-shape bodies. Up to the present it was always assumed, for the most part, that conical flow conditions prevail over delta wings, i.e., the state variables remain constant along rays through the tip of the wing. If one considers a continuous boundary layer development, one expects only slight and basically equivalent temperature variations. The results of the heating measurements show that the flow along the lee side of delta wings was important.

Previously known investigations about the lee side flow re- ferred primarily to thin delta wings. They showed that as the incident Mach number increases, there is a change in the type of flow -- from a flow with a leading edge vortex to a flow with vortices caused by shock-induced boundary layer separations. This type of flow with shock-induced separations, which only occurs at the higher incident Mach numbers, is especially interesting because of the practical heating problems.

The purpose of the present paper was to make a contribution to the problem of understanding the processes along the lee side of delta wings. The experiments attempt to make a close analysis about

the transition from the leading edge to the shock-induced separation. By using thick delta wings with different cross-sections, we wish to investigate the influence of different geometric parameters on the flow field. Using the experimental results, we developed a computation method with which one can describe the lee side flow for shock-induced separation.

2. Present status of the results of lee side flow

The flow field of a delta wing with an incidence angle in a supersonic flow can be broken down into two characteristic regions. The pressure side or underside faces the incident flow and is dominated by the influence of the leading edge shock. The lee side or top side is in the wake of the model, and this is the region which will be described in the following according to our present state of knowledge.

Figure 1 shows four flow models for the lee side of thin, slender delta wings with straight and sharp leading edges. The two figures on the left show the conditions for supersonic flow of the leading edges for both a small and a large angle of attack of the wing. The two sketches on the right show the corresponding conditions for supersonic incident flow of the leading edges. We can then give the following general description of the lee side flow according to Squire [9]. For Mach numbers normal to the leading edge which are substantially below the speed of sound and for small /9 angles of attack, the flow is not separated along the entire top side (Fig. 1a). By increasing the angle of attack, leading edge flow separation occurs with conically, rolled-up vortices and secondary separations (Fig. 1b).

Completely different conditions are found when the flow at the leading edge occurs at Mach numbers which are close to the

speed of sound or even above it. Figure 1c shows that for small angles of attack there is an expansion around the leading edge with nonseparated flow along the top side. A weak shock which runs through the tip of the delta wing is responsible for the deflection of the flow. At higher angles of attack, the shock is so strong that it induces a separation of the boundary layer with conical vortices again (Fig. 1d). In both cases, the separation in the central region of the wing shows a reattachment of the flow.

Figure 2 shows the flow regions of thin delta wings as a function of the angle of attach α_N and the Mach number M_N, both normal to the leading edge. Four flow regions can be distinguished here, which were first discussed by Squire [10] in this diagram with the boundaries shown. Vortex formation at the leading edge and shock-induced separation with attached and separated leading edge shock are known phenomena.

The Stanbrook-Squire region indicates where the transition from the leading edge separation to shock-induced vortex formation occurs. This boundary was determined from experiments with models of different cross-section shapes and sweepback, but with a sharp or a round leading edge. For small angles of attack, the results agree with those of Squire [9] using the investigations of Lindsay and Landrum [11] for profiles with sharp or round leading edges and the Mach number range $0.6 < M_N < 0.8$. The agreement is good.

Considering the papers discussed above, we can see that the two flow types, leading edge separation and shock-induced separation, are very important. Therefore, it seems appropriate to discuss these in more detail in the following and to present existing theories. Furthermore, we would like to discuss a flow field which is very important for this work. At very high angles of attack, the vortex flow above the wing can explode and can produce large

area turbulent fields. This "vortex breakdown" is of interest
especially because of certain experimental results in this paper.
In the last section we will briefly describe aerodynamic aspects
in the heating region along the lee side, because important in-
formation about the top side flow will be given from it.

2.1. Leading edge separation

The leading edge separation of delta wings with a sharp lead-
ing edge can be explained in the following physical terms. There
is a flow around the leading edge from the pressure side to the
leeward side. In this way, a high negative pressure forms in the
region directly adjacent to the leading edge. The large pressure
gradient which is produced in this way between the top side and
the bottom side produces a flow separation. It starts from the
leading edge and develops into a spiral conical vortex above the
lee side. A flow component is produced along the bottom side of
the primary vortex, which is aligned with the leading edge. How-
ever, it is not large enough to overcome the pressure increase be-
tween the underpressure peak induced by the vortex and the leading
edge. There is a secondary separation which occurs, and again it
rolls up into a conical vortex. Figure 3 shows the entire flow
field together with the characteristic stream lines and the pressure
distribution.

First, we will discuss the vortex as the main element of the
lee side flow of leading edge separation. According to measurements
of Earnshaw [12], the primary vortex can be primarily separated into
three parts. First of all, there is a vortex surface which emerges
from the leading edge and which "supplies" the second part, the vor-
tex itself. This can be assumed to be frictionless and conical.
The third part is the vortex chord, a small region in the center of
the vortex in which friction influences are not negligible. In this
region, large gradients of total pressure, static pressure and

8

velocities have been measured. Experiments show, in comparison
with the theoretical analysis of the vortices by Hall [13], that
there is good agreement with respect to the vortex shape and
velocity distribution.

In general, this vortex structure was confirmed in most ex-
periments, for example, the flow field investigations of Drougge
and Larson [14], as well as Thomann [15]. One detail effect we
wish to investigate is how the vortex position and pressure dis-
tribution or life coefficient change under the influence of vari-
ous parameters.

According to Okerbloom and Sarantsev [16], an increase in
the Mach number for fixed angle of attack leads to a displacement
of the vortex centers from the leading edge towards the central
plane. On the other hand, the height of the vortex core above
the model surface remains about the same. From this behavior,
we can see that the underpressure peak also decreases with in-
creasing Mach number and angle of attack. Since the size and
position of the underpressure maximum varies greatly in the vari-
ous experiments and theories, Hurley [17] attempted to find a
correlation of the various data, using the angle of attack, sweep
angle and Mach number.

Influences of geometry of delta wings on the flow conditions
have been reported by Fellows and Carter [18] for wings and wing-
body combinations. Greenwood [19] showed that with differing
sweep angle, large negative pressure coefficients are induced near
the leading edge for all Mach numbers, and there is only a slight
change in the central region of the delta wing.

According to Fig. 1 and oil film image photographs, there
are wall stream lines parallel to the incident flow in the region
of the attach flow near the central plane. In contrast to this,
Morris and Couch [20] found in wind tunnel tests an additional

component in the direction of the symmetry line in the central region after reattachment of the flow with very thick reentry bodies. The oil lines then run tangentially to the central plane downstream.

In the case of asymmetric vortex separations from the top side, one finds a further deviation from the normal behavior of the flow, which can occur primarily for wings in a symmetric, incident and slipping flow. Gapcynski [21] investigated this with elliptical cylinders, for which the asymmetric states were determined when a certain angle of attack was exceeded.

In general, most results show a high similarity of the flow conditions in the subsonic and supersonic range when there is leading edge separation, as experiments of Lee [22] have confirmed.

Most of the calculation methods for the slender delta wing with subsonic leading edg are based on the theory of Jones [23]. The flat delta wing is treated in planes perpendicular to the incident flow, just like a plate with vertical incident flow, using potential theory. In this first paper, the leading edge vortex was not included; therefore, the following theoretical models of Legendre [24], Adams [25] and Edwards [26] were concerned with the extension of the problem to two concentric vortex cores above the lee side in a potential flow. Brown and Michael [27] introduced a further substantial improvement of the vortex model, by connecting the concentric vortex cores with the leading edge using a vortex surface, and the vortex cores are represented as vortex lines starting from the tip of the model. Mangler and Smith [28] extended this model further. In this case a spiral-shaped vortex is divided into an outer part which emanates from the leading edge and an inner part which forms the foundation of the calculations.

10

The two last models, however, did not bring about any substantial improvement in spite of the fact that different models were used, so that both were used as the foundations for further calculations of Smith [29] and Nenni and Chee Tung [30]. The formed and thin delta wings were calculated by Carafoli and Staicu [31], by superimposing known flow fields and flow fields calculated with the method shown above. A refinement of the vortex model is achieved by simulation of the secondary vortex, which is replaced by a stagnation point flow by Pershing [32].

The above models for calculating the leading edge separation are based on the theory of slender bodies and Mach number influences are not considered. In experiments it was shown that as the Mach number increases, the vortex becomes flatter and its height over the leeward side decreases. These results were used by Küchemann [33] and Squire [34] and they replaced the real flow by vortices which are directly above the top side of the wing in their theoretical calculations.

Polhamus [35] gives a completely different solution method. The method is based on the "intuitive" assumption that the normal forces in the case of leading edge separation with flow reattachment in the central range are equal to the suction forces when there is flow around the leading edge with reattachment on the top side. This trial solution also considers Mach number influences. Very similar equations are obtained for the lift coefficient from a mathematical model of Coe [36], even though here the model of concentrated vortex cores is used again. Along the axis of these vortex lines, the effects of mass supply are introduced in the calculation using additional sinks. Even though the results of Polhamus agree much better with experiments compared with those calculated by Coe, the latter method seems to justify the "intuitive" procedure of Polhamus. An additional method of calculating conical flows is the method given by Hummel [37], which determines the flow variables according to the theory of slender bodies in cross-sectional planes with source distributions and vortex distributions

along the contour. In this method, arbitrary body shapes can be used, but the leading edge vortices were not considered in the flow model of this theory.

Table 1a is a summary of the various theories for leading edge separation which deals with new flow models.

Summarizing, we can say that there is a vast amount of knowledge about lee side flow in the case of leading edge separation. In experiments, it was possible to clearly identify the dominating vortex systems. However, simplified flow models were introduced in the theory. The agreement between the theory and the experiments regarding the pressure distribution and position of the vortices is partly unsatisfactory.

2.2. Shock-induced separation

Shock-induced separation along the top side of delta wings occurs in most cases of a supersonic leading edge. If the leading edge shock is attached, then it is possible to consider the top side and the bottom side separately. There is no flow around the leading edge, but instead there is an expansion which can be well-described using the Prandtl-Meyer flow. In this region the flow is attached on the top side. The expansion then causes a deflection in the direction of the central line. Because of symmetry, the flow must be parallel to it in the central plane, i.e., the transverse speed must be zero there. Since this backward deflection is to occur in a supersonic flow, it is created by a compression shock which runs through the tip of the delta wing. If the intensity of the shock is large enough, then there is a separation of the boundary layer downstream and a vortex forms which has a structure similar to the case of leading edge separation (Fig. 4). This model is supported by the investigations of the flow field with special regard for the position and

appearance of the internal shock, which was carried out by Bannink and Nebbeling [38-39]. The pressure measurements of Larcombe [40] clearly show the existence of the expansion with the subsequent internal shock in the vicinity of the symmetry plane. Also, the pressure distributions of Squire [41-42] on delta wings with different cross-section shape and sweepback show this. Here, it was possible to show that changes in the cross-section geometry of the delta wings does not bring about any substantial changes in the overall flow field, which has also been confirmed by investigations on the space shuttle [8, 43-44].

Pike [45], in experiments with round and sharp leading edges, showed that blunt edges change the lift only slightly, but the high pressure in these regions does contribute to the drag. The lowering of the peak of the delta wing [10-12] to reduce the heating also influences the flow in the symmetry plane.

Rao and Whitehead [5] established a flow model for the better understanding of the processes at high Mach numbers. It is shown in Fig. 5 and shows that the flow is not conical over a large part of the delta wing. The basis of this is a hypersonic "two-layer" boundary layer with various momenta. The pressure increase through the internal shock is different for the two layers and in this way a vortex is created inside the boundary layer. The vortex again in turn brings about a rarefaction of the boundary layer in the central region, which is related to a reattachment of the flow in the inner part of the wing. The flow model of Rein [46], shown in Fig. 6, is also not conical. It is the result of oil film photographs. If the leading edge shock is separated, one can observe leading edge vortices in the tip region, which, however, have to be explained here as the result of the mutual influencing of the shock and the separation bubble. The separation bubbles then form downstream at the leading edge, and again internal shocks can occur on them. Since the vortices can no longer be "supplied" by the

leading edge, they appear as free vortices in the central region of the wing. Experiments with two-dimensional wedges have shown that at least qualitatively there is a similar behavior between the flows perpendicular to the leading edge of a delta wing and the flow around a wedge with the same aperture angle, at least in the region of the leading edge.

Large wedge angles between the top side and the bottom side perpendicular to the leading edge or high angles of attack lead to a separated leading edge shock. Because of the subsonic region which is downstream from the shock, leading edge separation can again occur, according to Ghorai [47]. Since the subsonic region is limited to a relatively small region in the vicinity of the leading edge, a shock-induced separation occurs, as was confirmed by investigations of Collis (48) with six delta wings. Figure 7 gives a comparison of the flow models and shows the cross-section flow over a thick (Collis) and a thin (Cross [49]) delta wing in the hypersonic range. The boundary layer shape is different and this is related to the number of internal shocks, which can be one or two along each half of the wing. In both models, the shape of the boundary layer in the region of the symmetry plane seems unrealistic, because here one can assume a continuous transition from one half of a wing to the other. The most important data of the experiments described above are collected in Table 2.

In the following we will now present the most important /16 theories for describing the lee side flow for supersonic leading edges and will compare them with experiments. Maslen [50] discusses the top side flow only as a special case of the general flow around a delta wing with the solution of the nonlinear equations for conical flow. The calculation has no shocks and is divided into Prandtl-Meyer expansion and hyperbolic or elliptic regions, within which it is possible to give a solution of the differential equation using characteristics or relaxation. The conical flow

over a plane delta wing with supersonic leading edge was solved
by Clarke and Wallace [51] using an integral method in second
order terms with respect to the angle of attack. Internal shocks
cannot occur here. On the other hand, Fowell [52] calculated both
the continuous case without a shock as well as the discontinuous
case which, under some conditions, is the only possible solution.
Babayev [53] has proven that continuous flow cannot occur. This
solution consists of Prandtl-Meyer expansion, determination of
the shape of the internal shock and the shape of the adjacent
central region using iteration methods. Pike [54] calculated the
pressure distribution along the top side of a surfboard using the
linearized theory. From parameter studies, he concludes that with
increasing sweepback of the leading edge, the internal shocks in-
crease in intensity. In order to give a correct interpretation of
this result, we have to mention again that the internal shock de-
pends on the additionally induced component during expansion around
the leading edge. The Prandtl-Meyer expansion, in turn, depends
on the angle of attack and Mach number perpendicular to the lead-
ing edge. For a large sweepback, however, the M_N is reduced, but
the angle of attack α_N becomes larger, and in this way the estima-
tion of the intensity of the internal shock is made more difficult.

A three-dimensional characteristic method in which the internal
shock is represented by isentropic compression was established by
Beeman and Powers [55]. The special difference method of Kutler
and Lomax [56] is used in order to solve the three-dimensional,
frictionless and nonlinear basic equations for the top side as well.
An extension by Walkden, et al. [57], using boundary values from
the characteristic method, did result in improvements to the calcul-
ation program, but the internal shocks with a real intensity are
not calculated. Miyazawa [58], using comparisons between experi- /17
ments and modified theory of Kutler and Lomax, showed that on the
lee side of cones, no good agreement could be expected. In par-
ticular, for the hyperbolic region of the cross-section plane,

15

Christophel [59] determines the flow field using the characteristic method. This seems to be limited to the localization of the internal shock. To a limited extent, the "method of lines" of South and Klunker [60] can also be used for the lee side, but poor comparison possibilities result for high angles of attack, because in the real flow friction effects prevail. Extensive flow field investigations of Cross [49] were the foundation of a calculation method which, however, is based in part on empirical data. A model is used in which the flow expands at the boundary layer and it is deflected by a shock. The shock which is attached to the boundary layer produces a separation directly on the surface, which again results in a substantial thickening of the boundary layer behind the shock. The calculation method, however, is restricted only to expansion over the boundary layer, the internal shock and the adjacent central region. The vortex formation inside the boundary layer is ignored. The shape of the boundary layer and a parameter of the area equation of the internal shock must be introduced into the calculation as empirical data.

Table 1b shows the various theories of shock-induced separation as well as the different flow models.

Numerous experiments in the area of shock-induced separation have been carried out, but in only a few papers was it possible to detect the internal shocks. This already indicates that the knowledge about the processes in this type of flow is still deficient and is usually limited to high Mach numbers and thin and flat delta wings. The theoretical models which attempt to calculate the flow field with closed solutions have no shocks. Also, the few papers which include the internal shocks are not satisfactory compared with experiments. As far as is known, the model of Cross is the closest to the real flow, which was selected in the present paper as the basis of the theoretical analysis.

2.3. <u>Transition from leading edge separation to shock-induced</u> separation

Up to the present there is no systematic investigation about the transition from vortex formation at the leading edge to the shock-induced separation. This change in the flow type is very likely continuous and as a first approximation can be assumed to occur within the Stanbrook-Squire region (Fig. 2). This region was determined by considering the different vortex formations from all of the available experiments, both directly at the leading edge as well as inside through an internal shock. However, we should point out that it is difficult to carry out an exact analysis of the flow type because of ambiguities in the experimental investigation methods. For example, oil film photographs have very similar characteristics for leading edge separation and shock-induced separation. This could be the reason why a few experiments, for example, those of Whitehead and Keyes [1], cannot be classified in the boundary region.

Figure 8 gives a possible model on how the transition of the flow fields could occur. It was given by Squire [61], supported by "vapor screen" photographs. Starting with shock-induced vortex formation, the flow perpendicular to the leading edge at small Mach numbers is no longer capable of completely expanding. A separation at the leading edge occurs and, in addition, there is an expansion with subsequent internal shock. If the Mach number drops again, then the leading edge vortex is enlarged, whereas the expansion and the shock decrease in intensity, until finally only leading edge separation occurs with the secondary vortex.

An additional representation of the processes at the bottom side which can be related to the change in the flow type along the top side was also derived by Squire [61] from the "thin shock layer" theory. For a separated leading edge shock, the theoretical

analysis results in a discontinuous transition from a stagnation
line in the symmetry plane to an additional one in the vicinity
of the leading edge. The number of stagnation lines depends on
the flow region, so that according to the leading edge (1 stagna-
tion line) or the shock-induced separation (2 stagnation lines),
we can identify the flow range. The projected stream lines of
the bottom side are also shown in Fig. 8, and a continuous transi-
tion was assumed there.

The change from leading edge-induced separation to shock-
induced separation and the related flow processes at the bottom
side are only to be interpreted as a working hypothesis, because
no experimental investigations have been concerned specifically
with this problem.

2.4. Vortex breakdown

The flow field on the lee side of a delta wing with leading
edge separation can collapse for certain changes in the parameters,
for example, if one increases the angle of attack. This phenomenon,
also called vortex explosion, was explained by Werle [62] as an
expansion of the free, spiral-shaped vortex because of transition
from laminar to turbulent flow. Brooke-Benjamin [63] also does
not interpret the collapse as an instability, as was stated in
other investigations, but as a second dynamic state of the flow.
The "vortex breakdown" usually starts downstream from the trailing
edge and wanders upstream with increasing angle of attack. If a
position is then reached in the vicinity of the trailing edge,
then even small angular changes are sufficient to influence the
position of the bursting point. If the trailing edge is exceeded
and if the angle of attack is increased further, then according to
Lawson [64], a stable position in the vicinity of the tip of the
delta wing occurs and for sweep angles between $\Lambda = 70^\circ$ and 85°,

they are about at 37% of wing length. Peckham [65] determined
that the bursting position depends on a combination of angle of
attack and sweep angle. Since inverse proportionality exists be-
tween the two, in practice this means that "vortex breakdown" is
an upper limit with respect to angle of attack, and a lower limit
with respect to sweep angle for the flow with leading edge separa-
tion.

The results of Wentz [66], Sarpkaya [67] are of interest for
the present experiments. In the critical range, the bursting of
the vortices apparently is very sensitive to disturbances in symme-
try, whereas an increase in the pressure in the direction of the
vortex axis has a destabilizing effect. Even though relatively
little is known about the process of bursting and only a few
parameters can be recognized with certainty, Brooke-Benjamin [68]
and Jones [69] performed a theoretical analysis of this problem.   /20

These phenomena are observed in all subsonic incident flows
and only Elle [70] and Lambourne and Bryer [71] carried out ex-
periments near the speed of sound. For supersonic Mach numbers,
in [72-73] similar flow conditions were found in experiments.
Here again the "vortex breakdown" was noticed because of pressure
fluctuations and a decrease in the underpressure peak downstream
of the bursting point. Oil film photographs of burst vortices in
the subsonic and supersonic range have the same characteristics.
From this we can conclude that supersonic flow shows essentially
the same parameters and flow processes when there is collapse of
the vortex.

Here we have attempted to discuss briefly the special state
of the flow over the delta wing, which can only occur for certain
incident flow conditions. Even in the framework of the present
investigation, the occurrence of the "vortex breakdown" is think-
able, so that experimental results also have to be evaluated from
this point of view.

2.5. Heating

Already in the introduction we mentioned that many problems of lee side flow are the result of heating investigations. The high local temperatures which occur in the central region of the wing are of special interest. Experimental investigations of Whitehead and Keyes [1] led to a flow model for explaining these heating peaks. On the lee side, spiral-shaped vortices are created, and their circulating motions induce components directed downwards in the vicinity of the symmetry plane. On the other hand, near the body surface, a tangential velocity component is produced by the vortices which removes layers with low energy from the central region in the direction of the leading edge. The temperature peaks then result from the type of stagnation point flow in the symmetry plane and the boundary layer thickness which is reduced there. Whitehead [2] was essentially able to confirm these tests and even found two peaks in the temperature distribution along the central plane. One maximum was in the vicinity of the vortex origin and the other was produced by transition of the boundary layer.

The complete suppression, or at least reduction, of the high local temperature peaks by forming of the lee side or the leading edge or by dropping the model tip was not completely possible [3-5].

The essential parameters which influence the temperature peaks were investigated by Whitehead, Hefner and Rao [6] and were summarized by Hefner [8]. In the lower hypersonic range (M < 6), the temperature maxima depend greatly on the Reynolds number, but its local position can only be influenced by the angle of attack. In addition, there is a limiting Reynolds number below which the heating peak is reduced greatly and abruptly with decreasing Re number.

All of the previous experiments have shown that the greatest temperature increases occur along the top side in the low hypersonic range. At higher Mach numbers, the reduction in the boundary layer thickness discussed above in the central region does not occur, and instead there is a thickening. In this way, the flow conditions change so that the temperature peaks are greatly suppressed.

This summary does not assume to be complete, instead we only wanted to indicate the aerodynamic aspects in the area of heating problems.

3.   Experimental facilities

The analysis of the flow field on the lee side is essentially based on experiments in the wind tunnel using models with various design parameters. In the following we will present the wind tunnels, models and various test methods.

3.1.   Wind tunnels

Three different wind tunnels were used for the tests discussed in this report. The first experiments were performed in the supersonic wind tunnel of the Cambridge University Engineering Department (CUED). The tunnel is a blow-down type with a test section cross-section of 0.12 x 0.18 m and was operated at a Mach number $M_\infty = 3.5$ and a Reynolds number $Re = 5.0 \times 10^7$ 1/m.

Additional investigations were performed in the supersonic wind tunnel of the Royal Aircraft Establishment (RAE) in Bedford with a 0.9 x 1.2 m test section and for Mach numbers of $M_\infty = 3.5 - 4.5$

and Reynolds numbers of Re = 2.2 x 10^7 - 2.6 x 10^7 1/m.

The high speed wind tunnel of the Institute for Aerodynamics and Spaceflight (ILR) with a test section of 0.15 x 0.15 m was used in the speed range of M_∞ = 2.0 to 4.0 and for Reynolds numbers around Re = 1.0 x 10^7 1/m to test new and geometrically similar models.

Since we expected large interferences between the quasi-frictionless flow regions and the regions with friction, it is appropriate to compare the order of magnitude of the Reynolds numbers for free flight and in wind tunnels. Figure 9 shows the Reynolds numbers of the wind tunnel models using the present report as well as those of SST aircraft with design Mach numbers between M_D = 2.2 and 3.5 as well as for two reentry bodies. The differences which occur are considered in the discussion of the experimental results.

3.2. Models

All of the models investigated are delta wings with straight and sharp leading edges and conical surfaces. Figure 10 shows the different cross-section shapes of the Models I. These bodies were measured in the Cambridge and RAE wind tunnels and have a slenderness ratio of s/l = 0.31. Therefore, five different top side shapes are available: two delta shapes and two conical shapes, as well as a flat leeward side. The wind tunnel Models II in Fig. 11 have a slenderness ratio of s/l = 0.30 and were tested in the ILR wind tunnel. Two cross-section shapes are the same as for Model I, and in addition several experiments were carried out using the Nonweiler wave rider.

The slightly modified conical model shown in Fig. 12 has a shape which is probably close to a practical shape and it also has

a conical surface.

The pressure traps in the span direction were located at a relative wing chord of x/l = 0.55, 0.70 and 0.80. Further details are shown in the figures.

In all cases of this investigation, the angle of attack is measured with respect to the ridge line or the highest line of the top side.

3.3. Model suspension

The type of model suspension in the wind tunnel can create a disturbance to the flow around the delta wing under some conditions. In order to estimate possible influences, we show the suspensions in the three wind tunnels in Fig. 13. In the CUED tunnel, the wedge-shaped sting only penetrates into the wake on the pressure side of the model. In the RAE wind tunnel, there is a relatively thick suspension wedge, both on the pressure side and on the lee side. In the ILR tunnel, the relatively thin sting is located about three model lengths $x_K/l = 3.0$ downstream of the trailing edge.

3.4. Test methods and errors

In addition to static pressure measurements in the longitudinal and span directions on the model surface, Pitot pressure measurements were carried out at various heights above the body using a probe. It is difficult to estimate the influence on the flow field and the resulting measurement errors if the probe enters the region of the boundary layer or into a region of local subsonic flow. If one uses Pitot rakes, as in the present case, then we also have to consider the interference between the individual

measurement tubes. Quincey and Callinon [74], at a Mach number of $M_{\infty} = 1.6$, carried out experiments with rakes of different geometries. According to this, the intermediate space should be at least three times the external diameter of the tubes in order to avoid influences. The present experiments were performed with a rake where the spacing between the individual Pitot tubes was four times the external diameter, and so that there should be no interferences even for local Mach numbers smaller than $M_e = 1.6$.

In addition, the error which is the result of oblique incident flow to the Pitot tubes has to be estimated, because the probe had the same angle at all points of the flow field with respect to the incident flow. Figure 14 shows the calibration of a Pitot tube for two Mach numbers for angles of attack of up to $\alpha = 23°$. The Pitot pressure measured at different angles of attack deviates by a maximum of 3% compared with the value for $\alpha = 0$. For small angles of attack of up to about $\alpha = 4°$, no Pitot pressure losses could be detected.

In addition, errors occur in the measurements because of the nonuniform flow in the wind tunnel and also because of the measurement apparatus, such as the manometer, pressure transducer, scanner and pressure lines. Also, errors caused by asymmetry in manufacturing the model or nonexact alignment in the wind tunnel can lead to different results on the two wing halves.

An error estimation for the pressure coefficient in the CUED tunnel resulted in $\Delta c_p = \pm .002$ and even smaller values for the RAE wind tunnel.

At low pressures, the measurement is much more problematical, but in the atmospheric ILR tunnel for static pressure of the incident flow of $p_{\infty} = 34$ torr, we only detected a maximum error of $\Delta c_p = \pm .0015$. If we consider all of the error sources, it seems that a deviation of a maximum of $\Delta c_p = \pm .0025$ seems realistic in

24

all tunnels.

Investigation methods for the visualization of the flow included oil film photographs, shadowgraph photographs and Schlieren photographs. In the Cambridge wind tunnel we took oil film photographs after each test run, but before we observed to make sure that no large changes had occurred because the tunnel was turned off. In the ILR wind tunnel, all of the oil film images were taken during the test even though here there is the disadvantage of a reduced contrast and sharpness. Instead, in this method one is able to better recognize the dead-water regions in which the oil collects to form drops in some areas.

Even though we cannot make any definite statements from the analysis of the oil film photographs, we can still make a comparison of several characteristics. If we consider the vortex formation at the leading edge with the secondary vortices and attached flow in the central range, then we give the definitions from an oil film photograph of Fig. 15. The positions shown have been examined using other investigation methods. When specifying the vortex intensity, we assumed that the increase in the vortex intensity was related to a large radial speed, which again makes the wall stream lines run at a larger angle $\emptyset$.

4. Discussion of experimental results

Static and Pitot pressure measurements, as well as flow visualization methods, were used as the most important test methods in the experiments. The results will be used in the following to analyze the flow regions for the delta wings under discussion and to develop models of the processes on the lee side. We assume the already described two flow models for the leading

edge separation and the shock-induced separation.

When analyzing the test results, it has been found to be
appropriate to use the components of the incident Mach number
M_∞ and the angle of attack α in the plane perpendicular to the
leading edge of the wings instead of the values themselves.
These components are found from

$$M_N = M_\infty \sqrt{1 - \sin^2 \Lambda \cdot \cos^2 (\alpha + \Theta)}$$

$$\alpha_N = \arctan \left(\frac{\tan (\alpha + \Theta)}{\cos \Lambda} \right) - \arctan \left(\frac{\tan \Theta}{\cos \Lambda} \right)$$

The angle Θ is in the symmetry plane between the plane of
the leading edges and the ridge line, or the highest line on the
top side through the tip of the model. Therefore, for the flat
lee side we have $\Theta = 0^\circ$ and the equations given reduce to the
equations for the flat delta wing. The equations are given in
Fig. 16. The upper part of the figure shows the normal angle of
attack for different top sides and the lower diagram shows the
normal components of Mach number for the flat top sides as a func-
tion of angle of attack. Figure 17 shows the regions for the
angles α_N and the Mach number M_N which were selected in the ex-
periments. The tests with delta wing for a flat top side coincide
directly with the Stanbrook-Squire region; therefore, they can be
subjected to a detailed analysis. For all other models, the α_N
and M_N values are to the right of the Stanbrook-Squire region. The
experiments with these models attempt to determine the influence
of the cross-section area for shock-induced separation. Before we
can discuss these problems, however, we must clarify whether conical
flow can be assumed under the prevailing conditions.

26

4.1. Conical and non-conical flows

From the present state of knowledge of the lee side flow, we can see that conical and also non-conical flow fields can be distinguished. For most investigations with conically shaped surfaces, conical flow can be assumed as a good approximation. However, Cross [49], Squire [41], based on the models of Whitehead, et al. [6] and Rein [46], assumed non-conical flow over most of the wing. In the following we will examine to what extent these statements apply for the delta wings and the incident flow conditions investigated here.

Figure 18 shows the result of static pressure measurements for six different wing chords on the delta-shaped lee side of Model I. The results are the isobars for two angles of attack. These figures will be associated with the corresponding oil film photographs and can be considered representative for all of the other models. For both angles of attack, there is approximately conical flow, but we have to point out that this assumption is only valid to a limited extent. Deviations from conical flow were found for very small angles of attack as well as for very large angles of attack, especially in the tip region or in the region of the trailing edge. Since the models were relatively /27 small, it is not possible to exactly examine the tip region. Therefore, the investigation was concentrated on the central region, in which to a good degree of approximation there is conical flow for most of the incident flow conditions. It is assumed that in spite of this restriction, the results are representative for the entire flow field.

For wind tunnel tests with fixed model suspensions, one has to especially consider the influence of disturbances in the wake, which, just like the tail flow, can induce a deviation from conical conditions in the region of the trailing edge. This was established in tests and is discussed in a special chapter.

4.2. Results on the transition from leading edge-induced separation to shock-induced separation

The processes involved in the transition from the leading edge-induced to shock-induced separation are, for the most part, unknown and will be discussed in the following. Based on an evaluation of experimental results, Squire [10] gave a transition region called the Stanbrook-Squire region. Figure 17 shows that the models used here with the flat top side cover the Stanbrook-Squire region well for Mach numbers between $M_\infty = 2.5$ and 3.5. The flat lee side was selected so that the normal Mach number is clearly in the supersonic region and also because there is sufficient comparison material from other investigations. First of all, we analyzed the flat top side of the delta model and its flow field on both sides of the Stanbrook-Squire region, in order to then describe the change in the flow types with increasing incident Mach number for a representative angle of attack of the wing.

4.2.1. Separation with leading edge vortex

Leading edge vortices, according to Fig. 17, can be expected at a Mach number of $M_{oo} = 2.5$ and angles of attack between $\alpha = 5^{\circ}$ and 15°. Very large angles of attack were first not observed because the Stanbrook-Squire limit up to the present was only limited to values smaller than $\alpha_N = 50^{\circ}$.

According to known experiments, the following model prevails for the lee side flow for leading edge separation. Directly at the leading edge, a primary vortex separates, which again induces a secondary vortex along the outer wing region. Near the symmetry plane, there is a similar flow which reaches this region from above the vortex. Because of these conditions, a constant pressure is established in the central region, whereas the primary and

28

secondary vortices produce underpressure peaks. This model was confirmed by our own experiments, which is shown in the following for a delta wing with a flat lee side at $M_\infty = 2.5$ and $\alpha = 10^\circ$.

Figure 19 shows the different available information for this incident flow case. A direct comparison allows one to compare the statements many times. Attach flow in the central region was confirmed by oil film tests, Pitot tests and static pressure tests. The position of the primary vortex is found at about $y/s = 0.55$ and $z/s = 0.20$ and can be localized just like the secondary vortex at about $y/s = 0.78$ and $z/s = 0.08$, as well as from oil film photographs and from the different Schlieren photographs. Based on the low intensity of the secondary vortex and the closeness to vacuum conditions, one does not observe any second underpressure peak in the pressure distribution. Therefore, we can establish that the well-known ideas about leading edge separation have been confirmed by the available test material.

From this comparison of the various experiments, we obtained two important indications for interpreting oil film photographs and Schlieren photographs. In oil film photographs, the vortex center has to be assumed above the separation line, so that the typical oil lines only show half of the vortex flow. This is in contrast to the evaluation method of Rao and Whitehead [5], which places the vortex core exactly in the center between the separation line and the attached flow. In Schlieren photographs, we can observe a similar condition. There the dark gray and not-sharply-defined regions only are indications of the upper part of the vortex to the core. The lower vortex region in the vicinity of the wing surface can no longer be seen because of interferences and the fact that the body surface is so close. These observations about the vortex position in oil film photographs and Schlieren photographs are also supported by investigations of Mannerie and Werle [75], as well as of Drougge and Larson [14].

/29

From the result for $M_\infty = 2.5$ and $\alpha = 10^O$, we can now investigate the influence of angle of attack for the same incident Mach number on the flow field. We can expect that leading edge separation in the sense defined above will occur, and only the geometry of the flow field will change. The Schlieren observations for angles of attack between $\alpha = 10^O$ and 25° allow one to analyze the relationship with the Pitot isobars over the wing cross-section. Figure 28 shows that up to $\alpha = 15^O$, the primary vortex separates from the surface, whereas the secondary vortex essentially keeps the same position. The region influenced by the vortices expands further into the direction of the symmetry plane and there reduces the region of attached flow. This development of the flow field up to average angles of attack is normal in the regions of leading edge separation and was to be expected. From Fig. 20b we now find that for higher angles of attack after $\alpha = 17.5^O$, there are sometimes substantial deviations from the initial flow conditions. The primary vortices move away further from the surface and then increase their area of influence, so that no more attached flow occurs in the central region. The vortices on both wing halves are close to one another in the symmetry plane and in this way induce a very large velocity component in the direction of the top side. The flow, however, must again be parallel to the surface in the vicinity of the lee side and therefore is deflected through a shock which can only be found in the direct surroundings of the central plane. As can be seen from the Pitot isobars, for example, at $\alpha = 20^O$, this central plane shock is approximately parallel to the surface of the wing. When the shock occurs or when the vortices meet in the symmetry plane, the secondary vortex could not be found either in oil film photographs and Schlieren photographs or in the Pitot pressure distributions. A dead-water region is formed in the outer wing area which is shown as a shaded region in the Pitot isobars.

The continuity of the flow for transition from small angles
of attack to large angles of attack is confirmed by the pressure
distributions over the span in Fig. 21. From the curves, we show
the positions determined from oil film photographs for attached
flow in the central region (A), secondary vortex (SZ) and primary
vortex center (PZ). Up to $\alpha = 10^{\circ}$, one observes typical pressure
variations for leading edge separation with a constant central
region and a strong pressure drop in the region of the vortex
center. This result was also obtained from the CUED wind tunnel
and shows good agreement with the ILR tests considering the dif-
ferent tunnels and measurement methods. For the higher angle of
attack range, these clear statements can no longer be made. The
entire pressure level lies very close to the vacuum limit, so that
the effect of vortex flows on the pressure distribution is limited
by this. (The pressure increase in the outer wing area at $\alpha = 25^{\circ}$
is already an influence of the disturbance which comes from the
tail region, recognized in Schlieren photographs.) The result
from oil film photographs can be compared very well with the pres-
sure distribution and support previous results and models.

Figure 22 shows the result of oil film photographs in Schlieren
photographs and gives the positions of the attached flow in the
central region and the position of the vortices above the wing for
$M_{\infty} = 2.0$ and 2.5. The typical change in the position of leading
edge vortices with increasing angle of attack is known from tests
by Monnerie and Werle 75 and the theoretical analysis of Pershing
32 . The agreement with the present vortex positions determined
and these results show that for $M_{\infty} = 2.0$ we can draw the conclu-
sion that there is leading edge separation for the angle of attack
region ' up to $\alpha = 20^{\circ}$. For $M_{\infty} = 2.5$, on the other hand, above
$\alpha = 15^{\circ}$ there is an unexpected change in the vortex position, which
indicates that then there is no classical leading edge
separation.

Summarizing, we can say that to the left of the Stanbrook-Squire region between $\alpha = 5^{\circ}$ and 15° there is leading edge separation with primary and secondary vortices. From a further increase of the angle of attack, a flow field results which differs very greatly from the previous ideas, which show a dead-water region in the region of the former secondary vortex and which has a shock in the symmetry plane parallel to the surface. Since similar changes also occur for $M_{\infty} = 2.0$ but at higher angles of attack $(\alpha > 20^{\circ})$, here we have to specify a new limit. This result is given here in this paper only as an indication, because the purpose of our investigation is to give a detailed analysis of the flow regions inside and to the right of the Stanbrook-Squire boundary.

/31

4.2.2. The Stanbrook-Squire region

Since the flow regions to the left of the Stanbrook-Squire region have now been discussed and the typical characteristics of leading edge separation have been mentioned, we will now investigate the transition to shock-induced separation. For this purpose we will again assume the same incident flow conditions with the angle of attack of $\alpha = 10^{\circ}$ and the Mach number $M_{\infty} = 2.5$.

The pressure coefficients on the flat lee side are shown in Fig. 23 over the span for different Mach numbers but for a fixed angle of attack $\alpha = 10^{\circ}$. One can see large differences in the pressure distributions only along the outer wing region where the vortex dominates. The pronounced underpressure peak, already discussed somewhat for $M_{\infty} = 2.5$, becomes flatter for higher Mach numbers until finally the entire region only has a constant pressure. Even at higher Mach numbers outside of the Stanbrook-Squire limit, the form of the pressure distribution no longer changes but the pressure level only is displaced to higher values. In the central region where attached flow is assumed, the position of the separa-

tion point (A) only changes slightly. The pressure in this region
is constant and is only changed slightly with a change in Mach
number. An additional evaluation of the pressure distribution
is given in Fig. 24. Here the pressure in the region of attached
flow, as well as the minimum pressure coefficient (vortex center),
is shown for increasing normal Mach numbers M_N. In the region of
the Stanbrook-Squire boundary, the pressure coefficients reach a
maximum in the central plane. The pressure in the vicinity of the
vortex center decreases ahead of and behind the Stanbrook-Squire
boundary more steeply than inside of this region. In addition, we
show the corresponding values for the delta-shaped lee side, which
can be correlated with the other results, at least for the pressure
near the symmetry plane.   /32

From the pressure distribution we can see that the central
region with the parallel flow remains unchanged with increasing
Mach number, which is indicated by the combined oil film photo-
graphs and Schlieren photographs of Fig. 25. The vortex center, on
the other hand, is displaced towards the central plane so that the
diameter of the vortex must become correspondingly smaller. In
addition, these figures show that inside the Stanbrook-Squire bound-
ary, the intensity of the secondary vortex becomes smaller and it
is hardly perceptible at $M_\infty = 2.8$. When the secondary vortex
vanishes, only a dead-water region exists between the leading edge
and the primary vortex.

In addition, the Schlieren photographs show the approach of
the leading edge shock to the wing. In this way the Mach number
component M_N reaches values above one. It is to be expected that
immediately downstream of the leading edge there will be supersonic
conditions above the dead-water region and the character of the
lee side flow is changed in this way.

Two Schlieren photographs of the flow at $\alpha = 10^\circ$ and different
Mach numbers are given in Fig. 26. The dark regions which can be

interpreted as the upper halves of the vortices on the lee side are quite sharply limited first at M_∞ = 3.0 in the direction of the wing surface, but become more diffused at higher speeds. Two dark lines emerge from the trailing edge at the lee side of the model, which have to be the result of different wing regions. The upper region is in the form of a fan and can be interpreted as an expansion of the flow in the central region at the trailing edge. The second narrow line is almost parallel to the top side and can be interpreted as a wake dead water from the leading edge region of the wing.

Figure 27 shows an evaluation of the Schlieren and oil film photographs as a function of Mach number and gives the position of the vortices. We should mention that up to the present only little information about the Mach number dependence of the vortex position is available. The only systematic investigation of Okerbloom and Sarantsev [16] showed an almost constant height of the vortex above the wing between M_∞ = 2.0 and 4.0. This result was not confirmed here but one can observe that the vortex moves closer to the top side, which agrees with Monnerie and Werle [75]. Only when the Stanbrook-Squire region is crossed does the position become fixed for a fixed angle of attack.

Summarizing, we can establish the following for the transition region (Stanbrook-Squire region). The present results for an angle of attack α = 10° and different Mach numbers confirm a change in the type of flow above the Stanbrook-Squire region. This is a continuous process which is characterized by the following flow behavior: At low incident Mach numbers there is clearly a leading edge separation with primary and secondary vortices, as well as a parallel flow in the region of the symmetry plane. The increase in the incident speed and the increase in the normal component with respect to the leading edge means that the higher energy flow can resist the separation at the leading edge longer

and then a deflection around the leading edge becomes possible. In this way the separation angle between the surface and the feeding vortex surface becomes smaller and the entire vortex becomes flatter. In this way the diameter of the primary vortex becomes smaller and therefore the region of attached flow near the central plane can remain constant for the most part. Because the height as well as the intensity of the primary vortex decreases with increasing Mach number, the velocity components which trigger the secondary vortices are greatly reduced. About in the center of the S-S region ($M_\infty \approx 3.0$), the secondary vortex can no longer exist and the region between the leading edge and the primary vortex has to be interpreted as a dead-water region.

In addition to the flow conditions in these regions with high friction, one can also observe changes in the external flow. In the investigated models, there is a separated leading edge shock, but within the S-S region the speed of sound is reached at the leading edge. Above the layers with friction, a supersonic expansion occurs in the vicinity of the leading edge which determines the pressure level in this region.

The greater the incident flow speed, the flatter the layer /34 with friction becomes over which the expansion occurs. In this way the expansion is intensified and there is a substantial deflection of the flow in the direction of the central plane. The symmetry condition in the central plane can be satisfied by the deflected flow only by means of a shock. During the increase in Mach number, the shock intensity increases and the vortex intensity decreases.

Summarizing, we can say that the following events characterize the transition region for constant angle of attack and increasing Mach number:

-- The vortex is flatter above the surface and reduces its influence region whereas at the same time the intensity of the secondary vortices is decreased.

35

-- When the secondary vortex no longer occurs, a dead-
water region is formed inside the layer with friction.

-- The flow in the leading edge region reaches supersonic
conditions and the starting expansion over the friction
layer results in an internal shock.

-- Even though a continuous transition occurs and therefore
one cannot give a fixed boundary for the change in the
flow types, at least for $M_\infty = 3.0$ we established that
this results in the most noticeable changes in experi-
ments.

A detailed analysis of the flow conditions to the right of
the Stanbrook-Squire region has to be added to the above and will
therefore be carried out in the following section.

4.2.3. <u>Separation with a shock</u>

In the following we give an example of an analysis of the
flow field in the region of the so-called shock-induced separa-
tion for $\alpha = 10^\circ$ and $M_\infty = 3.5$ and in a discussion of the present
experiments. Figure 28 shows different test results for the
multiple comparisons. From this we can see that a dead-water
region exists directly on the surface in the outer wing region.
Between it and the external flow there is a type of boundary
layer which is probably highly turbulent. In the central region,
there is attached flow which is aligned parallel to the symmetry
plane.

Figure 29 gives an additional evaluation of Pitot pressure /35
measurements and also an additional model. We show the Pitot
pressure ratios over height for different span positions. In
these experiments one can assume that the Pitot probes aligned
parallel to the incident flow will provide reliable measurements

because of the high incident flow speed and the slender models, because in this case the transverse speeds are of secondary importance. This means that Pitot pressure ratios of $P_H/P_{P_\infty} \approx 1.0$ represent conditions like in the region of undisturbed incident flow or if the value is zero, they can be interpreted as dead-water regions. Figure 29 gives an evaluation in the flow model.

Based on the experimental results, we can establish the following model. At the leading edge there is flow separation just like before, but its intensity and momentum is very small and therefore can be called dead water. Since the separation is assumed to be a turbulent boundary layer, one can count on a re-attachment (according to the separation bubble in profile theory). On the other hand, the processes in the outer flow also influence the boundary layer. The supersonic flow which exists at the leading edge expands over the contour of the separated layers and for symmetry reasons, has to be deflected backwards again by means of a shock. The pressure jump through the inner shock affects the boundary layer and results in a reattachment of the separated flow. Because of this forced premature reattachment, according to profile theory we can speak of a separation bubble. Therefore, a stagnation results, which separates the dead-water region from the attached flow in the central region. Within the separation bubble there is a reverse flow which occurs, which has a certain circulation and which again can be called a vortex.

Therefore, we have established that in contrast to the original assumption, there is no shock-induced separation. In the case of the wings investigated here, the flow separation is not produced by a compression shock, but is a leading edge separation and the separated flow is made to reattach because of the shock in the external flow. It is quite possible, as found for small angles of attack, that a separation can occur at the leading edge without a shock. /36 On the other hand, just like for high Mach numbers, a supersonic

expansion at the leading edge and a deflection over a weak internal shock is thinkable without having a separation occur. The wings which are being discussed have been investigated in exactly this state range, where there is both separation at the leading edge as well as supersonic expansion with subsequent internal shock. Both flow components occur independent of one another, but influence each other until an equilibrium state is established between them.

Therefore, we have shown that for the wings under discussion, the Stanbrook-Squire region is only a boundary with respect to the flow in the frictionless region, because to the left and the right of the boundary there is a separation at the leading edge. The region to the right of the transition region will be called "separation with shock" region according to the results discussed.

Based on the previously developed flow model, we will now investigate the changes which occur for a variation of the angle of attack if we assume a fixed incident Mach number $M_\infty = 3.5$. As shown from Fig. 2, experiments are located in the region which up to the present was called "shock-induced separation" region. The oil film photographs in Fig. 30 show the development of the lee side flow for $M_\infty = 3.5$ for small-to-medium-sized angles of attack. For angles of $\alpha = 1^\circ$ the flow field appears to be non-conical and is quite similar to the experiments of Rein [46], and its flow model shown in Fig. 6. A second interpretation of these oil film photographs is that the transition from laminar to turbulent boundary layer causes the observed differences. However, for each of these possibilities, we can assume a vortex formation at the leading edge, until an angle of attack of $\alpha = 5.5^\circ$ is reached. For this angle of attack, the oil film photographs already have characteristics which were found when crossing the S-S boundary. For $\alpha = 8^\circ$, we again have the typical situation of a separation bubble with an internal shock, which exists up to angles of attack of $\alpha = 16.5^\circ$. However, at these angles there is already a great influence of the tail region, so that only the region near the tip

38

has to be considered as not being influenced.

The observations of the oil film photographs made are well-
confirmed by the pressure distributions in Fig. 31. The vortex
positions (WZ) taken from the oil film photographs and the regions
of attached flow in the central plane (A) are shown on the corre-
sponding curves. For small angles ($\alpha = 1^\circ - 3.5^\circ$), one obtains
pressure variations along the leading edge which are typical for
vortex formation. At $\alpha = 5.5^\circ$ the transition to the solution
bubble with internal shock seems to appear. The discrepancy in
the pressure distribution and the oil film photograph can be ex-
plained by the testing technique, because in all experiments the
models have almost zero angle of attack when the wind tunnel is
started and later on the desired angle is regulated using the
pneumatic system, i.e., in the start-up position certain oil lines
already form which will hardly change afterwards. At higher angles
of attack, again the influence of the tail becomes noticeable,
which at $\alpha = 12^\circ$ produces a pressure increase first in the outer
wing area. This disturbance from the wake is investigated in a
special chapter as far as it is relevant for the present experi-
ments, and will be critically analyzed.

Figure 32 shows the vortex positions for different angles of
attack. The position of the attached flow in the central region
is also shown and only has a large change for small angles. The
further development decreases continuously up to the angle of
attack $\alpha = 13^\circ$, where the vortex extends to the symmetry plane.

The position of the vortex is displaced between $\alpha = 3.5^\circ$(or
5.5°) and 8° very greatly towards the central plane, and when
there is a further increase in the angle of attack, its position
remains almost unchanged. This indicates a different flow field.
For small angles of attack, the position in the span direction is
comparable with incompressible ($M_\infty = 0$) results, so that here vor-
tex formation at the leading edge can be assumed. This was con-

firmed by experiments of Squire [41], as well as Monnerie and Werle [75], in which both the pressure distribution as well as the oil film photographs show the same characteristics, as occur here when the angle of attack is increased between $\alpha = 4^\circ$ and 8°.

For $\alpha = 8^\circ$ we can already expect the separation bubble with the internal shock. Up to $\alpha = 12^\circ$ there is only parallel attached flow in the central plane. At higher angles of attack, the vortex center again is displaced in the direction of the leading edge and also separates from the surface, without the occurrence of parallel flow in the symmetry plane. The vortex therefore expands its region of influence and apparently at $\alpha = 20^\circ$ again takes on values according to an approximation from the available data as is given by incompressible flow. This tendency of a separation line moving downwards was also demonstrated by Cross [49], who established leading edge separation for angles of attack of $\alpha > 20^\circ$ for relatively thin delta wings at $M_\infty = 10$. However, this contrast with the static pressure measurements in which the pressure increase measured near the central plane is displaced with increasing angle of attack in the direction of the symmetry plane. On the other hand, it is quite possible that the internal shock in the external flow moves somewhat inwards and the related pressure is felt up to the top side. At the same time, in this angle of attack region the close vacuum again influences the pressure level.

We already described how one can derive information about the vortex intensity from the oil film photographs. Figure 33 shows the relative flow angle for the investigated Mach number range which characterizes the vortex intensity, and it is plotted as a function of angle of attack. For all of the regions to the right and left of the S-S region, we can observe a maximum in intensity which is related to a meeting of the vortices in the symmetry plane and the related displacement of the attached flow. For Mach numbers up to the center of the S-S boundary ($M_\infty \approx 3.0$), these intensity

40

maxima are equivalent to the last occurrence of the shock in the symmetry plane. This central line shock at higher Mach numbers can no longer occur, and it is caused by the change in the flow type. This is because the intensity of the vortex and therefore the velocity component towards the surface is too small. A comparison of the vortex intensities for the different incident Mach numbers allows one to guess that at about $M_\infty = 2$ the maximum vortex intensity is reached.

Summarizing, we can describe the flow type "separation with shock" as follows for the case of a varying angle of attack:

-- For small angles of attack the vortex separation from the leading edge could be observed ($\alpha = 0^\circ$ to 3.5°).

-- After a transition region similar to the S-S region, /39
there is a separation bubble at the leading edge and an internal shock ($\alpha = 8^\circ$ to 14°) up to medium-sized angles of attack.

-- For high angles of attack we found an enlargement of the vortex and a new vortex formation from the leading edge. However, clear data are not available in this case, because the strong tail influences falsify the investigations ($\alpha < 14^\circ$).

4.2.4. Classification of the flow types

In the previous sections, we investigated the flow region for the flat leeward side, which according to Fig. 17 includes the Stanbrook-Squire region. The consequences drawn from this and the models developed are shown in Fig. 34 in a $\alpha_N - M_N$ diagram. In contrast to the previous S-S region, the region differs for small angles of attack. Here there is leading edge separation also on

the right side of the S-S region, and the new transition region approaches the M_N axis with increasing Mach number. Accordingly, there is also an upper boundary at which the transition from the separation bubble with internal shock to the leading edge vortex formation occurs. However, here we can also assume that above the vortices, shocks are produced. These models can be derived from the extreme case $\alpha = 90^\circ$, where the dead water is closed off by shocks, similar to a tail flow.

Comparisons between the discontinuities in the "thin shock layer" theory and experiments made Squire [61] assume that for thicker wings, the boundary between the regions B and D is displaced to smaller angles of attack α_N. With the present results, we can draw the conclusion that with increasing wing thickness, i.e., greater angle between the top side and the bottom side perpendicular to the leading edge, the Stanbrook-Squire boundary runs into the region B for large and small angles of attack, as is also shown in Fig. 34. The region B of the "shock-induced vortex formation" is limited on the left side for all wing thicknesses primarily by the Mach number, but for thick wings it is also limited upwards and downwards by the angle of attack.

Summarizing, we can therefore delimit the complex lee side flow field, not only by the Stanbrook-Squire region but also by regions which depend primarily on α or M_∞.

4.3. The influence of the cross-section shape on the flow for separations with internal shock

In the previous discussion, the flow field of the delta wing was treated with a flat (plane) leeward side. The bottom side of the wing was delta-shaped. In the following, we will consider delta wings with non-flat (delta shaped or conical) top side. The purpose of this investigation is to obtain information about the influence of the cross-section shape on the lee side flow. The ex-

42

periments are restricted to the range "separation bubble with internal shock," i.e., to the region to the right of the Stanbrook-Squire region. In most results it was assumed that the bottom and top side can be treated separately in the analysis. In a further section we will briefly discuss the influence of the bottom side on the lee side flow.

4.3.1. The delta shaped lee side

The delta shaped lee side was selected as the representative top side for investigating the influence of geometry. The shape was used primarily in the few known experiments, so that there is some capability of making comparisons. For a delta-shaped lee side, there are two plane model halves and therefore it can be assumed that only the angle θ (between the leading edge plane and the ridge line) is a geometric parameter which has any influence.

In the description of the flow fields for the delta-shaped lee side, we select an incident state with $M_\infty = 2.5$ and $\alpha = 10°$ as the initial example. After this we will demonstrate the influence by changing the angle of attack and increasing Mach number.

Figure 35 shows a flow model for the initial case which is the result of experiments. In the plane perpendicular to the leading edge, we find an angle between the incident flow and the top side of $\alpha_N = 17°$. The angle of attack α_N is therefore about half as large as was was the case for the corresponding incident flow states with the flat lee side. Among other things, this means that at the leading edge there is a Prandtl-Meyer expansion with attached flow on the top side, i.e., in the region of the leading edge there is no separation. The flow is deflected by means of the Prandtl-Meyer expansion, however, so that the resulting flow direction goes towards the symmetry plane. An internal shock, i.e., a series of /41 compression waves, provides the reverse deflection which is required

43

to satisfy the symmetry condition. The compression, however, re-
sults in a separation with the vortex. These processes are re-
stricted to the outer wing regions and the vortex has a relatively
small size, so that again there is attached flow in the vicinity
of the ridge line.

This model is only partly applicable for the flow, if the
angle of attack is changed together with a constant Mach number.
Figure 36 shows the results of Pitot pressure measurements for
$M_\infty = 2.5$ and different angles of attack, and it also shows the
results of oil film photographs and Schlieren photographs. For
small angles of attack up to $\alpha = 7^O$, there is leading edge vortex
formation. Their feeding vortex surfaces approach the surfaces
with increasing angle of attack and finally they attach. Between
$\alpha = 7^O$ and 11°, the normal component of the incident speed is so
large that there is no leading edge separation and the attached
flow exists in the outer wing region. Up to an angle of attack
of $\alpha = 14^O$, we can therefore assume a similar flow, as already de-
scribed for $\alpha = 10^O$. When the angle of attack is increased further,
the vortex center on the one hand moves in the direction of the
central plane and, on the other hand, moves away from the wing sur-
face. Since the internal shock does not change its position so
much, a dead-water region forms which increases inside between the
separation line and the vortex center. The vortices of the two
wing halves are then so close to the ridge line, that there is no
attached flow in the central region anymore.

The Mach number influence on the lee side flow for a delta-
shaped surface and fixed angle of attack $\alpha = 10^O$ will be discussed
using the pressure distribution shown in Fig. 37. An increase in
the Mach number here results in a correspondingly larger normal
component M_N, which is decisive for the expansion at the leading
edge. Based on the greater expansion rate, the internal shock and
therefore the separation caused by it are displaced in the direction
of the central plane. These processes can be observed for Mach

44

numbers of up to $M_\infty = 3.0$.

The flow conditions which prevail at higher Mach numbers /42
can best be explained using the model shown in Fig. 38. The
most characteristic feature is the oil film photograph shown
there, which shows that the flow is only partially conical.
Here there is a certain similarity with the flow around the flat
lee side at $M_\infty = 3.5$ in the lower angle of attack range. There,
there was a partial non-conical flow field (Fig. 30) along the
flat leeward side in the tip region of the wing, apparently
caused by the transition of the boundary layer. This transition
from laminar to turbulent boundary layer is also influencing the
states on the top side in the case of the delta-shaped lee side.
In the conical tip region, just like before, one finds an expan-
sion in the region of the leading edge with a subsequent internal
shock, which brings about a separation of the laminar boundary
layer. After about 30% of the wing chord, the transition to the
turbulent boundary layer starts. At the leading edge, a short
separation bubble is formed. By means of this change, the vortex
which occurs in the tip region of the wing loses its "supplying"
vortex surface and exists as a free vortex downstream of the transi-
tion region. This region of the wing has to be considered non-
conical.

For a critical evaluation of the flow model, we should indi-
cate that for $M_\infty = 3.5$, we carried out the greatest number of tests
with bodies having $\Theta \neq 0^\circ$ in the CUED wind tunnel. It is known
that the transition from the laminar to turbulent boundary layer
is influenced substantially by the Reynolds number, which in the
CUED wind tunnel is about 5 times greater in the ILR tunnel. This
aspect has to be considered for the flow field analysis carried
out here, especially for transition to the higher Mach numbers.
Therefore, in the following discussion we will separately discuss
the tests in each wind tunnel, in order not to have to consider

Re number effects which also occur in this flow range.

Starting with the results for M_∞ = 3.5 and α = 10°, using
the pressure distributions of Fig. 39, we investigate the in-
fluence of the angle of attack for a fixed Mach number. The out-
line pressure distributions are complemented by information ob-
tained from oil film photographs about the position of the
attached flow (A), the vortex center (PZ) and the separation
bubble (B). At α = 0° the flow is attached along the entire top
side and only near the leading edge does a weak expansion influence
the pressure values. Already at α = 3° one can notice a conical
vortex pair in the tip region of the wing, whose intensity, however,
is so weak that after transition in the central region there are
almost no more influences anymore. With increasing angle of attack
the intensity of the free vortex increases, but at the same time
its region of influence decreases. The separation bubble (B) at
the leading edge, on the other hand, becomes greater for higher
angles of attack, whereas the internal shock and therefore the
region of the attached flow is displaced further towards the central
plane.

The span positions of the vortex center and the attached flow
are shown in Fig. 40 for all angles of attack and Mach numbers.
From the vortex positions and by means of a comparison with the
values for the flat lee side (M_∞ = 0 and 2.5), we can see that for
the delta-shaped lee side for small Mach numbers and small angles
of attack, there is also vortex formation at the leading edge. The
position of the vortices develops quite differently as soon as
supersonic expansion occurs at the leading edge and therefore the
internal shock and separations occur with vortex formation. It
seems possible to find a limit which characterizes the transition
between the flow types. This region is shown in the diagram by a
shaded surface and shows good agreement with the transition regions
shown in Fig. 34 from the flow around flat delta wings with small

angles of attack. The position of the vortices is relatively in-
dependent of the Re number influence because it is always created
in the vicinity of the model tip. When we consider the attached
flow, we again have to consider the different wind tunnels.

Summarizing, we can say the following about the flow field
of the delta-shaped lee side in the investigated Mach number range:

-- In contrast to the flat top side and caused by the shape
   of the lee side, small angles of attack α_N and large Mach
   numbers M_N occur perpendicular to the leading edge. From
   this, attached flow results at the leading edge, together
   with a supersonic expansion. The internal shock induces
   a separation.

-- For small angles of attack, there is again vortex formation
   at the leading edge.

-- For certain incident flow conditions (M_∞-, Re-influence),   /44
   there can be a change in the flow field described above.
   Near the wing tip there is a transition from laminar to
   turbulent boundary layer. Downstream of this region, a
   short separation bubble is created which is closed off by
   the internal shock. The separation produced in the tip
   area exists as a free vortex above the wing.

4.3.2. <u>The influence of different shape parameters (angle Θ)</u>

In order to describe the influence of various top side shapes
on the flow field of the lee side, we first assume that the differ-
ences in the cross-section shapes are essentially described by the
angle Θ (between the leading edge plane and the ridge line).

Four different lee side shapes with angles between $\Theta = 0^\circ$ and

14° were available. This means we can describe the transition of the flow fields from the flat lee side to the delta shaped lee side. Figure 41 shows oil film photographs of the top sides for $M_{\infty} = 3.5$ and $\alpha = 10^{\circ}$, and the corresponding pressure distributions are also shown. With increasing angle Θ, the normal Mach number M_N becomes larger, whereas at the same time the normal angle of attack α_N becomes smaller. From the pressure distributions, we can see that the pressure level also decreases with increasing Θ. The values shown from the Prandtl-Meyer expansion with the cross-flow components around the leading edge confirm this tendency. Quantitatively, however, there are substantial differences between these calculated pressure values and the measured pressure values, which among other things are due to the influence of the leading edge shock. All of the investigated wings have differently shaped lower sides and therefore give a different position and shape to the shock. In this way, behind the shock, different values for M_N and α_N are created than calculated for the incident flow in the normal plane.

Figure 42 shows the influence of the shape angle Θ on the flow field for different top side shapes. Both the positions of the vortex centers as well as the attachment line vary slightly linearly with increasing Θ angle in the direction of the central plane. We should note that a reduced semi-span has been introduced which is the ratio of the lee side span for flat ($\Theta = 0^{\circ}$) and super-elevated wing ($\Theta > 0^{\circ}$).

$$\frac{y_{s_{\Theta > 0^{\circ}}}}{y_{s_{\Theta = 0^{\circ}}}} \cdot \sqrt{\frac{\tan^2 \Theta}{\tan^2 (90 - \Lambda)} + 1} \qquad \underline{/45}$$

For the transition from a flat to a delta-shaped lee side, we can develop the following model for the flow processes. Starting with the flow model with separation bubble at the leading edge,

48

internal shock and attached flow in the central region (Fig. 39), the Mach number in the normal plane M_N becomes greater as the shape angle Θ increases, whereas the angle α_N decreases. The flow therefore has more energy and the separation bubble at the leading edge becomes flatter. In this way the intensity of the circulation inside the separation is changed, so that the radial velocities decrease compared with the velocities in the axial direction. The reattachment line of the separation bubble is displaced toward the central plane and the region of the attached flow is reduced in size. Using the previous flow models, we must conclude that the internal shock changes its position only slightly. For sufficiently high transverse speeds, the transition of the boundary layer starts and determines the processes on the lee side already discussed in the previous chapter. The boundary layer transition is such that already for $\Theta = 9^{\circ}$ it can be observed along the rear part of the wing.

The following can be stated about the influence of the shape parameter Θ for plane top sides:

-- With increasing angle Θ the separation bubble becomes flatter and moves in the direction of the central plane. The intensity of vortex motion decreases. The inner shock barely changes its position.

-- For higher angle Θ incident flow states are reached which can bring about a transition of the boundary layer.

-- The geometric changes of the flow field are linear in the shape parameter Θ.

-- For the same incident flow conditions α_N and M_N, we observe basic changes in the flow field for the top sides, with different angle Θ (within the boundaries mentioned here). /46

The present experiments were all carried out in the range of flow with the separation bubble and internal shock. For the investigation of these wings inside the Stanbrook-Squire region, we can therefore no longer assume a linear dependence on the shape parameter. The boundaries in the α_N - M_N diagram therefore can only be assumed to be valid for a single angle .

4.3.3. The influence of different leading edge shapes (angle Ψ)

In the previous section we discussed the effects of different top side shapes on the lee side flow field in such a manner that we found a direct dependence on the shape angle Θ. In the following we will fix the angle Θ and discuss the influence of different leading edge angles Ψ (measured perpendicular to the leading edge between the top side and the bottom side), i.e., different curvatures of the lee side. Two wind tunnel models were used for this: the cone model (Fig. 43) and the modified cone model (Fig. 44). The results are compared with those for the delta model because all three wings have the same shape angle ($\Theta = 14^O$). The leading edges of the individual wings are shaped in such a manner that the conical delta wing has the largest angle ($\Psi = 75^O$) and the modified cone model has the smallest angle ($\Psi = 18^O$), whereas in the delta model we measured $\Psi = 40^O$.

The delta wings described here all have flat undersides and the plane of the leading edge is the same as the lower side plane. If one assumes a delta model with a plane lee side half, then the angle of attack in the plane perpendicular to the leading edge is described by the angle between the normal speed and the lee side. Therefore, for $\alpha = 0^O$ we also have $\alpha_N = \Psi$. If we have curved surfaces for a fixed shape angle Θ, then we also find different angles between the normal speed and the tangential plane in the region of the leading edge.

Very large leading edge angles Ψ, as are found for the cone model, result in a flow in the region of the leading edge where the lee side is seen under a negative angle. In this way, as shown in Fig. 43, a stagnation point is formed on the top side. Downstream of it, the flow field found from Pitot isobars and oil film photographs show mostly agreement with the flows along the lee side of circular cones with angles of attack. From these investigations, we can see that at least for small and medium angles of attack the leading edge no longer belongs to the lee side. In contrast to the delta wings used up to the present with a sharp leading edge and therefore a fixed separation line, the leading edge is of secondary importance for the lee side.

The other extreme case is a very small leading edge angle Ψ, as for example occurs for the modified cone model (Fig. 12). In the vicinity of the leading edge, the cross-section shape is conical with the angle $Ψ \approx 18^O$, whereas the central part consists of a cone segment. Here again the size and direction of the incident flow component perpendicular to the leading edge is unchanged compared with the delta shaped lee side, so that for an angle of attack of $α = 10^O$ an expansion angle of $α_{Nex} \approx 38^O$ is achieved in the leading edge region. As an example, Fig. 44 shows the pressure distribution and the characteristic flow model for two angles of attack. For angles of attack around $α = 10^O$, there is an expansion at the leading edge which induces a low pressure. Downstream the flow is uniform and the pressure distribution is constant. Only a very strong change in the flow direction caused by the body contour results in an internal shock whose intensity is greater than that found for previously observed delta wings. In the conical central region, we can again observe the vortex system which is typical for this shape. For angles of attack of $α > 15^O$, we can only achieve an incomplete deflection and expansion of the flow, so that total separation starting at the leading edges occurs. Inside of the separated region, there is subsonic flow and neither the internal shock nor other influences change the distribution here, which is

approximately constant over the wing. For higher Mach numbers, this flow field can already be observed for smaller angles of attack than $\alpha = 15°$.

From these examples we already can see that for a thick delta wing with a fixed shape parameter Θ the angle Ψ between the top side and the bottom side perpendicular to the leading edge substantially influences the aerodynamic properties such as lift, drag and efficiency of the control elements. Excessively large angles can lead to stagnation points in the leading edge region and therefore to overpressures on the lee side. On the other hand, the flow /48 for small angles Ψ and therefore large flow angles of the leading edge have a tendency to incomplete expansion or to complete separation at the leading edge.

4.3.4. The influence of the cross-section shape of the lower side

The lee side flow can only be influenced by the underside if the leading edge shock is separated. This applies for all delta wings in the investigated measurement range and means that it is necessary to estimate the influence of the lower side shape on the lee side flow. The position of the leading edge shock is primarily determined by the shape of the underside. Therefore, the inclination of the shock near the leading edge is, for the most part, determined by the shock distance in the vicinity of the central plane of the delta wing. Since the separated shock causes a deflection of the incident flow, different inclination angles of the leading edge shock can lead to substantial changes in the flow field on the lee side.

Figure 45 shows the different shock shapes of concave (wave rider) and flat (delta model) undersides for the identical lee side shape. At the same time, the Pitot isobars allow an analysis of the flow field on the top side for different shapes of the leading edge shock. For small angles of attack ($\alpha \approx 9°$) and for the flat

52

delta model, there is already a separation with an internal shock and vortex formation above the wing. On the other hand, the wave rider has a completely different behavior. On its top side, there is a type of separation bubble in the vicinity of the leading edge, and there is attached flow over large parts of the wing. This discrepancy must result primarily from the position and shape of the leading edge shock. For a flat underside, this lies both in the plane of the leading edge as well as in the symmetry plane at the same distance from the wing. The shock is almost perpendicular to the leading edge plane in the region of the leading edge plane and therefore brings about a deflection of the flow. The deflection angle at the leading edge becomes larger, whereas the corresponding local Mach number is reduced but remains in the supersonic range. For the wave rider, the shock is relatively close to the plane of the leading edges and is barely curved. The flow component perpendicular to the leading edge therefore reaches an almost perpendicular shock and retains its initial direction, approximately. At the leading edge, there is no expansion but a separation bubble is formed. For average angles of attack ($\alpha = 14^\circ$), the shock for the wave rider is substantially more curved in the region of the leading edges, so that we find a similar flow picture as was found for the lee side of the delta model. Nevertheless, because of the separation of the shock from the leading edges, we still find differences which are characterized by the vortex position and the size of the attached flow in the central region.

Theoretical results of Squire [61] represent a further indication about the relationship between the flow fields on the top side and the bottom side. The calculations showed that on the underside of thin delta wings, there is a sudden transition from a stagnation line in the symmetry plane to a second one which is near the leading edge. This change only occurs for certain incidence angle conditions and from comparisons with known experiments we can correlate this result with the transition from leading edge separation to

shock-induced separation on the lee side. These theoretical re-
sults are supported in the following by means of an example for
the delta model. Assuming that the change in the flow type on the
lee side is directly related to the change from the case with a
stagnation line in the symmetry plane to two stagnation lines on
the lower side, the change has to be continuous in contrast to
the theoretical results. This assumption is supported by Fig. 46,
which gives the stagnation line positions on the flat pressure
side as a function of Mach number. According to this, because of
symmetry reasons, a stagnation line in the central plane is ob-
tained and, depending on the incident flow conditions, there is an
additional one in the region of the leading edge. For the region
of separation with internal shock, we have two stagnation lines.
For attached leading edge shock as well as in the region of the
leading edge vortex, there is only the symmetry stagnation line.
These changes, first of all, only depend on the incident Mach num-
ber. However, there is also a tendency that an increase in the
angle of attack again leads to flow fields with a stagnation line,
which is at least apparent for small Mach numbers. However, the
proof that again leading edge vortices are created has not yet been
given.

For the flat pressure side, we can give the following physical
explanation for the position changes of the stagnation line. For
large Mach numbers, the shock is almost parallel to the underside
in the central region and is only curved in the vicinity of the
leading edge. In this outer region, the stream line has to be lo-
cated whose continuation through the shock makes up the stagnation
line. For a fixed angle of attack, the increase in the Mach num- /50
ber then causes the shock to approach the bottom side. The almost
plane central part of the shock is enlarged, whereas the curved
part and therefore the stagnation line again are displaced in the
direction of the leading edge. The reverse process can be observed
both by reducing the Mach number or by increasing the angle of attack.

The position of the stagnation line can therefore be considered as an element which determines the lee side flow. The closer it is to the leading edge, the less the underside shape can influence the lee side flow. This is clarified by a result from experiments. In the region of separation with internal shock, a comparison of the flat lee sides showed that both the pressure distribution of the top side as well as the flow field (oil film photographs) are almost identical for the delta model and the cone model. Here we can see that for higher Mach numbers, the stagnation line is immediately adjacent to the leading edge and the influence of different undersides (delta shape with $\Psi = 40^\circ$ and conical with $\Psi = 75^\circ$) is not important for the lee side flow.

Summarizing, we can say that depending on the incident flow conditions the shape of the bottom side has a non-negligible influence on the lee side flow. For the higher Mach number range, because of the position of the stagnation lines, the influence is small, so that the top and bottom side can be considered separately.

4.3.5. Additional remarks about the influence of the cross-section shape

We have previously discussed special geometric variables of the cross-section shape and in the following we will compare the investigated shapes.

An evaluation of the oil film photographs (according to Fig. 15) can be done here by interpreting the inclination angle of the wall stream lines Φ_p in the vortex region as the intensity of circulation. With this assumption, Fig. 47 shows the vortex intensities on the top side of various delta wings as a function of the angle of attack. We find a good correlation of the values shown with the angle φ_{st} , which is measured in the cross-section plane between the

plane of the leading edges and the separation point. The angle $\varphi_{s\ell}'$ is used as an average value in Fig. 47 for the different lee sides and for a fixed angle of attack ($\alpha \approx 10^\circ$), even though in general it depends on the angle of attack because of the position change of the separation line. Nevertheless, up to average angles of attack ($\alpha \sim 12^\circ$) the vortex intensities of different lee sides can be compared. Higher angles of attack then lead to the already mentioned collapse of the top side flow and the values can no longer be correlated.

In the previous sections, we have shown that the flow fields for example for delta shape lee sides basically do not change, but are only influenced by means of the angle Θ , which changes the geometry. This is also supported by the separation line angle $\varphi_{s\ell}$, which apparently is directly dependent on the shape angle for the plane top side shapes with $\varphi_{s\ell} \approx 2 \cdot \Theta$. Such a relationship can no longer be derived for curved lee sides, because then additional influences modify the flow field because of the shape.

The effects of the different cross-section shapes of the delta wings can also be felt in a collective representation of the pressure distributions for two angles of attack, shown in Fig. 48. In the separation region with leading edge vortex ($M = 3.5$ and $\alpha = 5.5^\circ$), the pressure distributions are very different in the external wing regions up to the leading edge, because the shape, position and intensity of the primary vortices vary greatly. In the central region, on the other hand, one finds attached flow for almost all wings and one finds comparable pressure coefficients. In the region of separation with internal shock ($M_\infty = 3.5$, $\alpha = 10^\circ$), the pressure distributions over the bodies with different angle Θ are very similar qualitatively, but do have clear quantitative differences. This has to be interpreted in the following way. In spite of different cross-section shapes, the individual elements of the flow field, such as expansion, internal shock, etc., are fixed more at certain positions in this region. The vortex is

no longer the dominant element and only has a small influence on
the pressure distribution. In contrast to this model, the delta
wings have a different behavior with special cross-section shapes.
The cone model with a stagnation point on the lee side only reaches
the pressure level of the other wings in the central plane. For
the modified cone model, in the vicinity of the leading edges we
find pressure values which are comparable with other models. Be-
hind the steep pressure increase caused by the internal shock, we
find a similar tendency and a similar pressure drop as in the cone
model. This indicates that for delta wings with cross-sections
which are constructed from simple geometric shapes, in part the
corresponding flow fields can be superimposed in order to obtain
models of the flow processes.

The aerodynamic coefficients are important for the practical
use of delta wings as aerodynamic bodies. As an example shown in
Fig. 49, we will demonstrate how from the integration of the pres-
sure distributions, certain lift coefficients of different wings
will change with angle of attack. Four different cross-section
shapes were selected and for two cases, we show the additional lift
gain on the lee side. The comparison of the convex delta model and
the flat delta model shows that in the region of separation with
vortex formation ($\alpha < 5.5^{\circ}$), the lee side lift of the flat surface
($\Theta = 0^{\circ}$) is greater than that of the delta-shaped wing ($\Theta = 9^{\circ}$).
On the other hand, the values in this region of separation with
internal shock are almost equal in size, as can already be con-
cluded from the already mentioned similarity of the flow fields.
Most of the lift coefficient is the result of the pressure side,
of course, so that flat or slightly curved shapes will result in
the highest C_A value, whereas delta shape and conical undersides
lie substantially below these values. Therefore, it is understand-
able that out of the wings considered here, those with a slightly
convex bottom side ($\Theta = 5^{\circ}$) and a delta-shaped lee side ($\Theta = 9^{\circ}$)
will have the highest lift coefficient in the investigated angle of
attack range. In order to evaluate the wing shapes, however, one

57

has to consider further aerodynamic coefficients and speed ranges. Therefore, it seems that this cross-section area is a favorable design for the underside and the top side with simultaneously an acceptable volume distribution.

The lift coefficient which is also shown for two theories for flat delta wings~shows good qualitative agreement for the linearized supersonic theory and good quantitative agreement for the "thin shock layer" theory. For $\alpha = 0$, we already have finite lift coefficients, because only in this way can one make a comparison with thick delta wings where the underside already has an inclination towards the incident flow because of its form $(\theta > 0^\circ)$.

Additional information in Fig. 50 shows the different development /53 ment of the vortex positions for different wing shapes. For the wave rider, the influence of the leading edge shock is very dominant for the lee side flow, so that compared with other wings, the vortex is displaced only slightly in the direction of the central plane for moderate angles of attack. Oil film photographs show that large area separations occur more easily than for other delta wings. On the other hand, there is a very stable flow field over the cone model. The internal shock changes its position hardly at all for average angles of attack, so that there is an almost constant vortex position. It is interesting that at the high angles of attack, in the present case $\alpha = 20^\circ$, the vortex separations are about the same for all of the wings. From this we have to conclude that here again we have a phenomenon which is independent of the delta wing geometry, which was already observed elsewhere.

Summarizing, we can state the following important influences of cross-section shape on the lee side flow field:

-- For a fixed shape angle θ, the leading edge angle Ψ has to be selected for stable flow states in such a manner that neither excessive flow angles occur at the front

side (total separation on the lee side) nor do negative values occur (stagnation point on the lee side).

-- Strong and discontinuous changes in the cross-section area can lead to substantial pressure increases and temperature increases.

-- By a favorable combination of the surface shape and the volume distribution, we find the maximum lift coefficient for the convex delta model (with delta-shaped lee side) out of the delta wings investigated here.

The transfer of the results obtained here for practical applications of thick delta wings as aircraft body forms has to be complemented by the following remark. Basically a certain volume has to be available for an aircraft. One characteristic quantity might be the volume parameter $\tau = V/F^{3/2}$ (V = volume, F = base area). If one assumes that in practice one requires at least a volume parameter of $\tau = 0.08$, and the values of $\tau > 0.65$ are no longer of interest, then this can be specified for a wing with a delta-shaped cross-section by means of the angle Θ. For a delta wing with a sweepback of $\Lambda = 73°$, we then find $\tau_{\Theta=8°} = 0.085$ and $\tau_{\Theta=20°} = 0.658$.

/54

If we consider the example of a cruise Mach number of $M = 4$, then the flow region of interest on the lee side in the $M_N - \alpha_N$ diagram can first be limited by curves corresponding to $\Theta = 8°$ and $\Theta = 20°$, Fig. 51. In order to provide stable flow states without large area separations, we conclude from the present discussion that a maximum normal angle of attack of $\alpha_{Nmax} = 30°$ cannot be exceeded. In addition, experiments have shown that on the one hand no basic changes of the flow field can be expected when the angle Θ is varied and, on the other hand, for angles of attack of $\alpha \sim 25°$, large separated regions occur on the lee side. In this case, there was a tendency to separations already for small angles

of attack in contrast to thin wings, so that there is a further re-
striction caused by the angle of attack α_{max}. As the lower limit
for this example, we will assume the case where α_N becomes nega-
tive and a stagnation line with a high pressure is created on the
lee side. Therefore, we have specified $\alpha_{Nmin} = 0^\circ$. The remain-
ing region inside the shaded lines is characterized by two differ-
ent flow types, which are divided between separation with vortex
formation and internal shock by means of the boundaries established
in the present report. The sketched diagram is only an example for
two parameters which have to be considered as restrictions for the
top side in the design of delta wings in order to obtain stable
flow states.

5. Influencing of the lee side flow by disturbances in the tail region

Some of the experiments showed that even for supersonic speeds
the flow on the lee side can be influenced by disturbances down
stream of the trailing edge. For example, experiments in the Cam-
bridge wind tunnel at angles of attack of $\alpha = 15^\circ$ showed an increase
in the static pressure on the lee side, which sometimes was above
the incident flow values [76]. Possible causes of this might be the
interference or blocking in the tunnel or changes in the lee side
flow, for example the bursting of the vortices and formation of
shock systems. In order to clarify these questions and in order to
avoid influences of the tunnel itself, we performed experiments in
different wind tunnels. In the following we give a brief summary
about these tests.

As an introduction, Fig. 52 shows the pressure coefficient
along the flat and delta-shaped lee side as a function of angle of
attack. The results are from the three wind tunnels and show a
pressure increase for certain angles of attack, which sometimes is
above the values for the incident flow. One remarkable feature of

the results from the RAE tunnel is that higher angles of attack again lead to underpressures on the lee side. A comparison of the suspensions of the models shows that in the Cambridge channel there is a relatively thick sword with a wedge in the pressure side wake. On the other hand, in the RAE tunnel the wings were suspended on a wedge with a very large aperture angle, which penetrates into the lee side wake as well as into the pressure side wake (Fig. 13). The ILR measurements were carried out with a suspension configuration similar to that which was used in Cambridge and therefore show comparable results. Experiments for other longitudinal positions show that first in the vicinity of the trailing edge, the pressure values increase but further upstream one still cannot find any influences.

The static pressure on the underside of the wings, the pressure at the channel wall upstream and downstream of the model, as well as Schlieren photographs, prove that these phenomena cannot be contributed to a collapse of the flow in the test section. Experiments in different wind tunnels show that this cannot be explained by specific tunnel disturbances. As Fig. 52 allows one to conclude, and from experiments with similar models [41], in which such a phenomenon was not observed, the different wing suspensions can be looked upon as a possible explanation for this. First of all, we have to assume that there is an influence on the lee side flow because of disturbances from the tail region. /56

In order to estimate possible disturbances of the lee side by the influences of the flow in the tail region, we carried out two groups of experiments: First of all, the effects of perturbing bodies on the lee side flow were investigated and then we investigated the influence on the tail flow. In the following, we give a brief summary about the results, and some of them were already reported in [77].

First of all, experiments were performed with and without pressure hoses or coverings to simulate these hoses. We were able

to show that already by means of changes in the immediate vicinity of the tail, i.e., without any obstacles which penetrate beyond the top side, the influence on the lee side vortices is great. Similar observations were made by Richards [78] with a cone model (2). It was found that the vortices are non-conical for a certain angle of attack and then become conical again for higher angles of attack. Already Lukosiewicz [79] indicated conical separation on a Pitot tube.

Further experiments were performed with wedges or blunt bodies [80] directly on the lee side or in the wake of the bottom side or the top side. Both the aperture angle and the height of the wedges as well as their position upstream and downstream of the trailing edge were varied. However, in these experiments it was not possible to obtain qualitative information about the influences of the different parameters. In all of the cases with perturbing bodies, we found an increase in the static pressure as well as a bursting of the lee side vortex. The pressure increase also occurred on one symmetry half of the wing even for asymmetric incident flow states, and overall it was dependent on whether the perturbing body was located in the wake of the underside or the top side.

In addition, the effects of perturbing bodies on the tail flow were investigated (see also [81]). As a function of angle of attack in all cases there is a substantial increase in the tail pressure when wedges are installed either in the underside wake or the top side wake.

6. Calculation of the flow field

Up to the present there has been no theoretical calculation method known which gives a complete and realistic description of the flow field on the lee side in the region of "separation with shock." This is essentially based on the fact that very complex

processes occur on the top side, such as boundary layer separation
with vortex formation and compression shocks with interaction with
the boundary layer, and this makes it difficult to obtain a closed
system of equations which can be solved.

It will be shown that a calculation based on a flow model de-
termined from the experiments is very difficult. For this reason
it seems appropriate to introduce models which are based on a
highly simplified flow model. A comparison of the two calculations
and a comparison with the experimental results will verify that the
great effort to determine the lee side flow is justified.

6.1. Determination of the flow variables based on a highly-simplified lee side model

In order to compare and estimate the present experimental
and theoretical results, we will determine the Mach numbers, pres-
sure coefficients and the position of the internal shock using a
simple calculation method.

The flow model shown in Fig. 66 is similar to the one of
Fowell [52], where in a plane perpendicular to the leading edge
the flow variables are first determined. These are then the basis
for the subsequent Prandtl-Meyer expansion around the leading edge.
The additional component in the direction of the central plane
which is created must then be equalized again by means of an in-
ternal shock, as already mentioned. The internal shock is assumed
to be flat in this case and perpendicular to the wing surface.

The Mach number perpendicular to the leading edge is already
known as

$$M_N = M_\infty \sqrt{1 - \sin^2 \Lambda \cdot \cos^2 \alpha}$$

with the corresponding angle of attack

$$\alpha_N = \arctan \frac{\tan \alpha}{\cos \Lambda}$$

With the assumption that the expansion is complete, as already shown in Fig. 66, we obtain the Mach number M_{Ne} from the Prandtl-Meyer function

$$\nu(M_{Ne}) = \nu(M_N) + \alpha_N$$

The pressure coefficient is then

$$c_{Pe} = \frac{\frac{p_e}{p_\infty} - 1}{0.7 \, M_\infty^2} \quad \text{mit} \quad \frac{p_e}{p_\infty} = \left[\frac{1 + \frac{M_N^2}{5}}{1 + \frac{M_{Ne}^2}{5}} \right]^{7/2}$$

The angle at which the flow is inclined in the direction towards the central plane is found to be

$$\gamma = \arctan \left(\frac{M_{Ne}}{M_\infty \cdot \cos \alpha \sin \Lambda} \right) - (90 - \Lambda)$$

Since this is also the deflection angle for the internal shock, we have $\delta = \bar{\gamma}$, and therefore from

$$M_e = \sqrt{M_{Ne}^2 + (M_\infty \cdot \cos \alpha \sin \Lambda)^2}$$

we can determine the remaining quantities through the shock, such as the Mach number $\hat{M}_e$, the shock angle Θ and the static pressure ratio

$$\frac{p}{p_e} = \frac{7 \, M_e^2 \sin^2 \Theta - 1}{6}$$

The pressure coefficient is then

$$c_{p_s} = \frac{\frac{p}{p_\infty} - 1}{0.7\, M_\infty^2} \quad \text{mit} \quad \frac{p}{p_\infty} = \frac{p}{p_e} \cdot \frac{p_e}{p_\infty}$$

The position of the internal shock is found from the angle which it forms with the symmetry plane $\gamma = \Theta - \delta$

and therefore $\quad y_s/s = \dfrac{\tan(90 - \Lambda)}{\tan \gamma}$

From these quantities, we have specified the pressure distribution over the wing and this is then available for comparison with experiments and the calculation method now described.

6.2. Determination of the flow field based on an experimental lee side model

Before we discuss the developed calculation methods, we will first give the basic flow model. In order to remain within the region of separation with the shock and also to obtain comparison possibilities which are known from other calculation methods and experiments, the range of validity of the calculation is restricted as follows. We will only consider delta wings with a plane flat lee side and sweep angles between $\Lambda = 65°$ and $85°$. Over the entire flow region, we assume supersonic leading edges ($\alpha = 0°$) so that we always have

$$\frac{\cos \Lambda}{\sin \mu_\infty} > 1$$

where $\sin \mu_\infty = 1/M_\infty$

The calculation method is therefore only valid for Mach numbers between $M_\infty = 3.5$ and 7, as well as for angles of attack of $\alpha = 12°$ to $25°$. The shape of the underside is then introduced in the calculation only for determining the separated or the attached leading

65

edge shock, because in this Mach number range the lee side flow is, for the most part, independent of the underside (see Sec. 4.3.4) because of the fact that the stagnation lines are adjacent to the leading edge. The assumption of conical flow has been confirmed, for the most part, by experiments (see Sec. 4.1), so that in the calculation we can assume a cross-section area perpendicular to the leading edge. The experimentally determined flow model is shown in Fig. 67 in this plane, and only for one-half of the wing because of symmetry, and it can be divided into the following regions.

1. Incident flow in the cross section plane;
2. separated leading edge shock;
3. flow behind the shock perpendicular to the leading edge;
4. boundary layer above the wing within which recirculation is formed;
5. Prandtl-Meyer expansion over the boundary layer in the vicinity of the leading edge;
6. internal shock;
7. flow above the boundary layer which is thickened by the internal shock in the central region of the wing;
8. parallel flow, at least in the symmetry plane.

The flow field being described can be divided into two characteristic regions: The region of the boundary layer with friction is considered in the calculation as the surface of the wing, so that only the contour is determined, and the flow inside the boundary layer is ignored. When determining the Pitot pressure isobars in planes perpendicular to the wing surface, we introduce a simple trial solution for the state variables inside the boundary layer in order to have a possibility of making comparisons with the experiment in the region with friction. The frictionless region can /60 again be divided into two regions, separated by a compression shock. The outer region of the wing is limited by the leading edge shock and the inner shock, whose shock front runs along conical lines through the tip of the model. A separation of the inner and outer

66

wing region exists because disturbances in the central region outside of the boundary layer cannot propagate through the inner shock. The calculation of the flow field is done separately and in the order of regions shown above. Essentially, the theory contains the computation steps shown in the macro-flow diagram of Fig. 68, which will now be discussed. The incident flow conditions and the geometry of the body are introduced as input data. After this, one decides about the leading edge type and the question of whether there is an attached leading edge shock or a separated one. After the shock relationships have been used using the leading edge shock, the calculation of the expansion above the boundary layer has to be carried out in three dimensions, in order to finally obtain a velocity field parallel to it in the symmetry plane. Since the expansion creates an additional velocity component, an internal shock is created from the mentioned symmetry conditions on the wing, which causes a deflection of the flow. The subsequent flow around the "thickened" boundary layer is calculated with different methods, depending on the speed range. In the supersonic range, the Prandtl-Meyer expansion is used, but in the subsonic range the panel method is used. The final flow field can only be determined by means of an iteration.

Coordinate Systems

The coordinate system is selected according to various criteria. First of all, it should be possible to have a direct comparison between theoretical and experimental results, but on the other hand one should obtain the simplest possible solution of the equations in the calculation method.

First of all, we will select an aerodynamic and cartesian coordinate system whose origin is at the type of the model. The x-axis with a unit vector $\vec{i}$ is parallel to the incident flow, the y- and z-axes with the unit vectors $\vec{j}$ and $\vec{k}$ are shown in Fig. 69.

The analytical treatment of the flow field is carried out in a
plane perpendicular to the leading edge of the model. Therefore,
it seems appropriate to introduce a body-fixed coordinate system,
and the x-axis is parallel and the y-axis is perpendicular to the
leading edge. This second coordinate system is obtained from the
aerodynamic system in which the X-Z plane is rotated by the angle
$(90° - \Lambda)$ and the X-Y plane is rotated by the angle α. The unit
vectors here are $\vec{l}, \vec{m}, \vec{n}$. The transformation equations from
the body-fixed system to the aerodynamic system are therefore:

$$X = x \cdot \cos \alpha \sin \Lambda + y \cos \alpha \cos \Lambda - z \sin \alpha$$
$$Y = -x \cos \Lambda + y \sin \Lambda \qquad (1)$$
$$Z = x \sin \alpha \sin \Lambda + y \sin \alpha \cos \Lambda + z \cos \alpha$$

If we include the separated leading edge shock in the calcula-
tion, we find a third coordinate system whose $\bar{x}$-axis is parallel
and its $\bar{y}$-axis is perpendicular to the shock trace in the plane
on the top side of the model. The rotation angles for a similar
coordinate transformation as in (1) are the angle of attack α and
the shock angle Λ_s .

The leading edge shock

The question of whether there is an attached or a separated
leading edge shock at the leading edge is made based on the "thin
shock layer" theory of Squire [82]. First of all, two new parame-
ters are introduced by using a density ratio through a shock

$$\varepsilon = \frac{\varkappa - 1}{\varkappa + 1} + \frac{2}{(\varkappa + 1) M^2 \sin^2 \alpha} \qquad (2)$$

as well as the transformed semi-span

$$\Omega = \frac{b}{\varepsilon^{1/2} \cdot \tan \alpha} \qquad (3)$$

and the thickness parameter

68

$$C = \frac{h}{\epsilon^{1/2} \cdot b} \tag{4}$$

From boundary layer considerations, we then find that in the
$C-\Omega$ plane, as shown in Fig. 70, the line $\Omega - C = 2$ delimits sepa-
rated and attached leading edge shocks.

For the attached leading edge shock, we can have no influence
of the top side on the bottom side, so that we can justify a sepa-
rate calculation. The initial values for expansion at the leading <u>/62</u>
edge are found directly from the values of the undisturbed flow.
The Mach number components in the body-fixed coordinate system are
obtained from scalar multiplication of

$$\vec{M}_{01} = (M_\infty \cdot \vec{l}) \circ \left\{ \vec{l}; \vec{m}; \vec{n} \right\} \, .$$

Therefore, the component parallel to the leading edge is

$$M_{0T} = M_\infty \cos \alpha \sin \Lambda \tag{5}$$

and the component normal to the leading edge in the plane of the
top side is

$$M_{0M} = M_\infty \cos \alpha \cos \Lambda \tag{6}$$

and the component normal to the top side is

$$M_{0N} = -M_\infty \sin \alpha \tag{7}$$

The Mach number component perpendicular to the leading edge
is then the vector sum of (5) and (6)

$$M_{N1} = M_\infty \cdot \sqrt{1 - \sin^2 \Lambda \, \cos^2 \alpha} \tag{8}$$

The important angle of attack in this plane is also found from
the Mach number components

$$\tan \alpha_N = \left| \frac{M_{0N}}{M_{0M}} \right| = \frac{\tan \alpha}{\cos \Lambda} \qquad (9)$$

For the case of a separated leading edge shock with $(\Omega - C) < 2$, we have to determine the shape and the position of the shock. The exact determination of the shock geometry is very complex even for simple bodies. For the present problem, we selected a simplified approximate solution. A first support of this are experiments with which the shock form was determined for different angles of attack. For a rhombic delta wing at $M_\infty = 7$, the results of Collis [48] are shown in Fig. 71. In the plane of the leading edges, the changes in the shock separation $y_s/s = 1.1$ at $\alpha = 0°$ and $y_s/s = 1.2$ at $\alpha = 17°$ or $25°$ are very small. Figure 72 shows an additional example of our own test results for $M_\infty = 3.5$. In addition to evaluations of Schlieren photographs, we also show results of the theory of Moeckel [83] and the "thin shock layer" theory. The latter has the disadvantage that only values within the wing span $y_s/s < 1$ can be determined and therefore the interesting region near the leading edge is not covered. On the other hand, the theory of Moeckel only gives the shock separation along the symmetry axis of the incident flow, /63 whereas the shock shape is assumed to be approximately a hyperbola. Figure 73 gives an evaluation of this theory for two-dimensional and rotationally symmetric bodies in conjunction with our own experiments. It is exactly in the lower Mach number range that there is a strong change in the shock separation, whereas above $M \sim 2.5$ there is approximately a constant value. If we use this knowledge and the experimental results, we can approximate the shock separation referred to the span of the delta wing in the form of a hyperbola by the following relationship:

$$\frac{y_s}{s} = \frac{0.748}{M_\infty - 1} + 1$$

Therefore, it becomes possible to calculate the shock trace angle Λ_s in the plane of the leading edges (see Fig. 69) as a function of the incident Mach number M_∞ and the angle of attack α.

$$\Lambda_s = \pi/2 - \arctan\left[\left(\frac{0.748}{M_\infty \cdot \cos^4\left(\frac{3}{2}\alpha\right) - 1} + 1\right)\tan\left(\pi/2 - \Lambda\right)\right] \qquad (10)$$

The variation of this curve for different sweep angles is shown in Fig. 74 and is compared with available experiment data. Equation (10) shows that the influence of the angle of attack is small compared with that of Mach number which was already mentioned in the discussion of Fig. 71.

In addition to knowing the shock separation from the shock trace angle Λ_s , we only have to know the inclination angle of the shock with respect to the top side Φ_s to continue the calculation, which is shown in Fig. 75. This angle is determined in the plane perpendicular to the leading edge shock and is referred to the normal to the top side plane of the wing. The inclination angle in general differs only slightly from zero degrees, i.e., the shock is almost perpendicular to the plane of the top side. For the calculation, we set $\Phi_s = 5^\circ$ in all cases, which is an estimation which seems to be justified based on experimental knowledge. This means we have specified all the parameters of the leading edge shock required for the calculation.

In order to determine the flow variables above the separated leading edge shock, we define a coordinate system $\bar{x}$, $\bar{y}$, $\bar{x}$ in the plane of the top side in such a manner that the $\bar{x}$-axis is on the shock trace at an angle of Λ_s , as shown in Fig. 75. Just like in the attached shock, the Mach number component in the y-z-plane is found from

$$M_{s_i} = M_\infty \cdot \sqrt{1 - \sin^2\Lambda_s \cdot \cos^2\alpha} \qquad (11)$$

and the effective angle of attack is

$$\alpha_s = \arctan\left(\frac{\tan\alpha}{\cos\Lambda_s}\right) \qquad (12)$$

The shock angle for the use of the oblique relationships is

$$\beta_s = 90° - \alpha_s + \phi_s \tag{13}$$

Behind the shock in which it is to be considered plane, we obtain the following deflection angle

$$\delta_s = \pi/2 - \arctan\left[\tan\beta\left(\frac{(\gamma+1)\ M_{S_1}^2}{2(M_{S_1}^2\ \sin^2\beta_s - 1)} - 1\right)\right] \tag{14}$$

and the Mach number

$$\hat{M}_{S_1}^2 = \frac{36\ M_{S_1}^4\ \sin^2\beta_s - 5(M_{S_1}^2\ \sin^2\beta_s - 1)(7 M_{S_1}^2\ \sin^2\beta_s + 5)}{(7 M_{S_1}^2\ \sin^2\beta_s - 1)(M_{S_1}^2\ \sin^2\beta_s + 5)} \tag{15}$$

The total Mach number behind the shock in the X-Y-Z coordinate system is then

$$\begin{aligned}
\vec{M}_1 = \ &\vec{i}\,(M_\infty\cos^2\alpha\,\sin^2\Lambda_s + \hat{M}_{S_1}\cos(\alpha_s+\delta_s)\cos\alpha\,\cos\Lambda_s \\
&+ \hat{M}_{S_1}\sin(\alpha_s+\delta_s)\sin\alpha) \\
&-\vec{j}\,(M_\infty\cos\alpha\,\sin\Lambda_s\,\cos\Lambda_s - \hat{M}_{S_1}\cos(\alpha_s+\delta_s)\sin\Lambda_s) \\
&+\vec{k}\,(M_\infty\sin\alpha\,\cos\alpha\,\sin^2\Lambda_s + \hat{M}_{S_1}\cos(\alpha_s+\delta_s)\sin\alpha\,\cos\Lambda_s \\
&- \hat{M}_{S_1}\sin(\alpha_s+\delta_s)\cos\alpha)
\end{aligned} \tag{16}$$

In order to determine the initial quantities for the Prandtl-Meyer expansion, we make a scalar multiplication of Mach number $\vec{M}_1$ and the unit vector of the body fixed coordinate system. From the tangential component

$$M_{1T} = \vec{M}_1 \circ \vec{l}$$

the component perpendicular to the leading edge in the top side plane

$$M_{1M} = \vec{M_1} \circ \vec{m}$$

and the component perpendicular to the top side

$$M_{1N} = \vec{M_1} \circ \vec{n}$$

we obtain from the scalar summation of M_{1M} and M_{1N} the magnitude M_{N2} of the Mach number perpendicular to the leading edge. (If in the lower M_∞ range there is subsonic flow perpendicular to the VK, then nevertheless we can specify that the component required for the expansion is at least $M_{N2} = 1$, otherwise there would be a flow around the VK. Squire [10] also argued that because of the proximity of the VK shock, the sonic line starts at the VK.) The effective angle of attack is

$$\alpha_N = \arctan\left(\frac{M_{1N}}{M_{1M}}\right), \tag{17}$$

and the corresponding sweep angle is

$$\Lambda_N = \arccos\left(\frac{\sqrt{M_{1M}^2 + M_{1N}^2}}{(\vec{M_1})}\right) \tag{18}$$

In this way, from the oblique shock relationships we can determine all of the other flow variables, for example, Pitot pressure ratio and static pressure ratio.

Boundary layer

In the present calculation method, it will be found that it is not necessary to carry out detailed boundary layer calculations. As already mentioned, the displacement boundary layer is used as a fixed boundary for an isentropic (Prandtl-Meyer) expansion. Within the framework of this analysis, it seems sufficient to assume a simple two-dimensional boundary layer and to use the displacement thickness for a flat plate, as was done in [84]

$$\delta^* = \varepsilon \cdot \left(0.664 + 1.73 \frac{T_w}{T_0} \right) M_\infty^2 \left(\frac{C \cdot y}{U_\infty / \nu_\infty} \right)^{1/2}$$

Using the following rest variables, which prevail in the ILR tunnel,

rest temperature $T_0 = 293^\circ$ K

wall temperature $T_w \approx T_\infty \, (1 + 0.169 \, M_\infty^2)$, with $T_\infty = T_0 / (1 + \frac{M_\infty^2}{5})$

speed of sound $a_\infty = 343.2 \, \frac{m}{s}$ (at T_0)

kinematic viscosity $\nu_\infty = 14.9 \cdot 10^{-6} \, \frac{m^2}{s}$ (at T_0 and $P_0 = 760$ torr)

Sutherland constant $C = \frac{T_0 + S}{T_w + S}$ with $S = 110^\circ$ K)

we obtain

$$\frac{\delta^*}{s} = \varepsilon \left[0.664 + 1.73 \, (1 + \frac{M_\infty^2}{5}) / (1 + 0.169 \, M_\infty^2) \right] M^{3/2} \sqrt{\frac{C \cdot y \cdot \nu_\infty}{s^2 \, a_\infty}}$$

where ε = density ratio over a perpendicular shock.

From experiments, we find that in addition to the Mach number, the angle of attack also has a substantial influence on the displacement thickness of the boundary layer. The ratio of these thicknesses for a wing with angle of attack and without angle of attack is found from

$$\frac{\delta^*_\alpha}{\delta^*_{\alpha = 0}} = 43.3 \cdot (\frac{y}{s})^{1/2} \cdot \alpha^{9/4} + 1$$

The overall boundary layer displacement thickness is given by

$$\frac{\delta^*_{ges}}{s} = \frac{\delta^*}{s} \, (2 + 43.3 \, (\frac{y}{s})^{1/2} \, \alpha^{9/4}) \tag{19}$$

In order to calculate the flow field, we require the contour of the boundary layer displacement thickness, which is first given by (19).

This relationship is only used in order to determine the displacement thickness at a certain point. The position of the point can be found in the vicinity of the base point of the internal shock and is described by means of the angle γ, which is between the symmetry plane and the corresponding trace line. This angle is found from experiments based on an evaluation of oil film photographs as follows:

$$\gamma_s = \mu_\infty - \Lambda \cdot (0.305 \cdot a + 0.085)$$ (20)

Here we have $\mu_\infty = \text{arc sin}(1/M_\infty)$, which is the Mach angle. From the angle γ, we obtain the required distance from the leading edge γ_{so}, which is required to calculate the displacement thickness from

$$\frac{\gamma_{so}}{s} = \frac{\tan(90 - \Lambda - \gamma)}{\tan(90 - \Lambda)}$$ (21)

This means that from equation (19), we can determine the displacement thickness $\frac{\delta^*_{so}}{s}$ in the vicinity of the internal shock. Comparison calculations, however, give a negligibly small error if instead of equation (19), one uses a simple parabolic shape of the boundary layer displacement thickness, using the coordinates at the point $(y^*_{so} / \delta^*_{so})$, determined above:

$$\delta^* = \delta^*_{so} \left(\frac{y}{y_{so}} \right)^{1/6}$$ (22)

In this way we can determine the expansion from the displacement boundary layer determined here.

Expansion in the leading edge region

The flow variables determined in the plane perpendicular to the leading edge are used as initial values for the expansion above the boundary layer. The parabolic displacement thickness along the span given by equation (22) is replaced by straight-line segments.

In steps, the flow variables in this region of the wing are determined using Prandtl-Meyer expansion.

The local flow angle ϕ is equal to the angle α_N for an attached VK shock for the first value of expansion. Also, the expansion Mach number here is $M_{E1} = M_{N2}$. The corresponding position on the boundary layer is determined using the inclination

$$\tan \varphi_{GS} = \frac{d\delta^*}{dy} = \frac{1}{6} \delta^*_{S0} \cdot (y \cdot y_{S0})^{-5/6} \tag{23}$$

in such a manner that $\varphi \doteq \varphi_{GS}$

The division of the boundary layer into segments by specifying a fixed angular amount $\Delta\phi$ allows one to determine the velocity distribution. The local flow direction is specified by

$$\varphi_i = \varphi_{i-1} - \Delta\varphi$$

The Prandtl-Meyer angle is therefore

$$\nu_i = \nu_{i-1} + (\varphi_i - \varphi_{i-1})$$

and the Prandtl-Meyer function is

$$\nu = \sqrt{\frac{\varkappa+1}{\varkappa-1}} \cdot \arctan \sqrt{\frac{\varkappa-1}{\varkappa+1}(M^2-1)} - \arctan \sqrt{M^2-1} \tag{24}$$

and we can then determine the Mach number M_{E1} through an iteration as discussed in Appendix 1.

This does specify the required flow variables in the cross-section plane, but we still have to introduce the tangential component into the calculation. This three-dimensional analysis is required because in the region of the symmetry plane, the flow direction must again be parallel to the incident flow, i.e., the scalar

multiplication of the velocity vector and the unit vector perpendicular to the central plane has to equal zero.

The vector of the incident flow can be divided into the following components

$$\vec{U}_{\infty} = \vec{U}_{l0} + \vec{U}_{m0} + \vec{U}_{n0}$$

and also behind the leading edge shock

$$\vec{U}_1 = \vec{U}_{l1} + \vec{U}_{m1} + \vec{U}_{n1}$$

The tangential component is constant over the shock and is

$$\vec{U}_{l0} = \vec{U}_{l1}$$

and we obtain

$$\vec{U}_1 = \vec{U}_{\infty} + (\vec{U}_{m1} - \vec{U}_{m0}) + (\vec{U}_{n1} - \vec{U}_{l0}) \qquad (25)$$

By dividing through the magnitude of the incident flow speed, we find

$$\frac{\vec{U}_1}{|\vec{U}_{\infty}|} = \frac{\vec{U}_{\infty}}{|\vec{U}_{\infty}|} + \frac{(\vec{U}_{m1} - \vec{U}_{m0})}{|\vec{U}_{\infty}|} + \frac{(\vec{U}_{n1} - \vec{U}_{n0})}{|\vec{U}_{\infty}|}$$

$$(25a)$$

The unit vectors are given by

as well as
$$\frac{\vec{U}_{m0}}{|U_{m0}|} = \vec{m} \quad \text{und} \quad \frac{\vec{U}_{m1}}{|U_{m1}|} = \vec{m}$$

$$\frac{\vec{U}_{n0}}{|U_{n0}|} = -\vec{n} \quad \text{und} \quad \frac{\vec{U}_{n1}}{|U_{n1}|} = -\vec{n}$$

For the y-direction, we refer these unit vectors $\vec{m}$ to the

absolute magnitude of $|\vec{U}_\infty|$

$$\frac{\vec{U}_{m1} \cdot \vec{U}_{m0}}{|\vec{U}_\infty|} = \left[\frac{\vec{U}_{m1}}{|\vec{U}_{m1}|} \cdot \frac{|\vec{U}_{m1}|}{|\vec{U}_{m0}|} - \frac{\vec{U}_{m0}}{|\vec{U}_{m0}|} \right] \frac{|\vec{U}_{m0}|}{|\vec{U}_\infty|}$$

where

$$\frac{|\vec{U}_{m1}|}{|\vec{U}_{m0}|} = \frac{\hat{M}_{S1} \cdot \cos \varphi}{M_{S1} \cdot \cos \alpha_S} \cdot \frac{a_{S1}}{\hat{a}_{S1}} = \frac{\hat{M}_{S1} \cos \varphi}{M_{S1} \cos \alpha_S} \cdot \sqrt{\frac{1 + \frac{\varkappa-1}{2} M_{S1}^2}{1 + \frac{\varkappa-1}{2} \hat{M}_{S1}^2}} \qquad (26)$$

and

$$\frac{|\vec{U}_{m0}|}{|\vec{U}_\infty|} = \cos \alpha_S \cdot \cos \Lambda_S .$$

Here, ϕ is the local flow angle which is defined directly behind the shock with $\varphi = \alpha_S + \delta_2$ and which is reduced by $\Delta\phi$ during the Prandtl-Meyer expansion. Also, the Mach number M_{s1} directly behind the leading edge shock is given by equation (15), but during the expansion the prevailing Mach number M_{E1} is substituted in equation (26).

If this trial solution is also introduced in the z-direction and if we consider that

$$\frac{\vec{U}_\infty}{|\vec{U}_\infty|} = \vec{i}$$

then for the vector in the outer region of the wing, we find

$$\frac{\vec{U}_2}{|\vec{U}_\infty|} = \vec{i} + \left[\vec{m} \left(g(M_E) \cdot \cos \varphi - \cos \alpha_S \right) \right. \\ \left. - \vec{n} \left(g(M_E) \cdot \sin \varphi - \sin \alpha_S \right) \right] \cos \Lambda_S \qquad (27)$$

According to equation (26), the function $g(M_E)$ is defined by

78

$$g(M_E) = \frac{M_E}{M_{S1}} \sqrt{\frac{1 + \frac{\varkappa-1}{2} M_{S1}^2}{1 + \frac{\varkappa-1}{2} M_E^2}}$$

In the aerodynamic coordinate system with the transformation

and

$$\vec{m} = \vec{i} \cos \alpha \cdot \cos \Lambda_S + \vec{j} \sin \Lambda_S + \vec{k} \sin \alpha \cos \Lambda_S$$

$$\vec{n} = -\vec{i} \sin \alpha + \vec{k} \cos \alpha$$

we obtain the equation (27) shown completely in Appendix II.

In order to determine the overall Mach number M_2 in this region, we exploit the fact that the critical speed of sound does not change above the shock. Therefore, we have the following relationship between the local and the critical Mach number:

$$M_2 = \left(\frac{2}{\varkappa+1}\right)^{1/2} \cdot M_2^* \cdot \left(1 - \frac{\varkappa-1}{\varkappa+1} \cdot M_2^{*2}\right)^{-1/2} \tag{28}$$

where

$$M_2^* = \frac{|U_2|}{a^*} = \frac{|U_2|}{|U_\infty|} \cdot \frac{|U_\infty|}{a^*}$$

and

$$\frac{U_\infty}{a^*} = \sqrt{\frac{\varkappa+1}{2} M_\infty^2 \left(1 + \frac{\varkappa-1}{2} M_\infty^2\right)^{-1}} \tag{28a}$$

The internal compression shock

During expansion over the boundary layer in the outer wing region, an additional velocity component is created in the direction of the central plane. Since symmetric flow fields occur for the delta wing under consideration, the direction of the velocity must be parallel to the incident flow at least in the symmetry plane.

Accordingly, in the central region of the wing, there has to be a deflection of the flow through a shock. The shock shape and position are not known a priori and are determined from an iteration. The different velocity ranges which are the result of the expansion (see Fig. 67) lead to a curved shock surface. Since we have assumed conical flow, the shock surface is formed by straight lines which all run through the model tip. In the following, we will determine the position and shape of the shock and the vector of the speed behind the shock. With the assumption that the tangential component over the shock is constant, we obtain the following for the speed:

$$\vec{U}_3 = \vec{U}_2 + (\vec{U}_{e3} - \vec{U}_{e2}) \tag{29}$$

where $\vec{U}_{e2}$ and $\vec{U}_{e3}$ are the components perpendicular to the shock front. In order to evaluate equation (29), we first have to specify the direction of the normal components. In an arbitrary point on the shock surface, we can define a tangential plane using two vectors α and β which are perpendicular to one another.

$$\alpha = \vec{i} \cos \gamma - \vec{j} \sin \gamma$$
$$\beta = \vec{i} \sin \gamma \sin \Phi + \vec{j} \cos \gamma \sin \Phi - \vec{k} \cos \Phi$$

Here γ is the projection of the shock trace angle in the x-y-plane and Φ is the local inclination angle of the shock with respect to the y-z-plane rotated by γ. The vector product is then the normal vector which is perpendicular to any point of the shock front.

$$\alpha \times \beta = \xi = \vec{i} \sin \gamma \cos \Phi + \vec{j} \cos \gamma \cos \Phi + \vec{k} \sin \Phi \tag{30}$$

The velocity components using equation (29) are then found from

$$U_{e3} = \vec{U}_3 \circ \xi \quad \text{and} \quad U_{e2} = \vec{U}_2 \circ \xi$$

and therefore

$$(\vec{U}_{e3} - \vec{U}_{e2}) = (\vec{U}_3 \circ \xi - \vec{U}_2 \circ \xi) \circ \xi$$

80

The Prandtl relationship gives the relationship between the normal components in front of and behind the shock

$$\vec{U}_3 \circ \mathfrak{k} \cdot \vec{U}_2 \circ \mathfrak{k} = a^{*2}$$

If we again introduce unit vectors, then we obtain the following for equation (29)

$$\frac{\vec{U}_3}{|U_\infty|} = \frac{\vec{U}_2}{|U_\infty|} + \left(\frac{1}{M_{c2}^{*2}} - 1\right) \cdot \left(\frac{U_2}{|U_\infty|} \circ \mathfrak{k}\right) \circ \mathfrak{k} \tag{31}$$

With the relationship between the local and critical Mach number /71

$$M^{*2} = \frac{\varkappa - 1}{2} \cdot \frac{M^2}{1 + \frac{\varkappa - 1}{2} M^2}$$

and equation (27)

$$\frac{\vec{U}_2}{|U_{c\infty}|} = a\vec{i} + b\vec{j} + c\vec{k}$$

we can then write

$$\frac{\vec{U}_3}{|U_\infty|} = a\vec{i} + b\vec{j} + c\vec{k} + \left(\frac{2}{\varkappa + 1} \cdot \frac{1 - M_{c2}^2}{M_{c2}^2}\right)\left(\frac{\vec{U}_2}{|U_\infty|} \circ \mathfrak{k}\right) \circ \mathfrak{k}$$

If we use the condition that in the central region behind the shock the flow is parallel to the symmetry plane, i.e.,

$$\frac{\vec{U}_3}{|U_\infty|} \circ \vec{j} = 0 \tag{32}$$

we then obtain

$$0 = b + \left(\frac{2}{\varkappa + 1} \cdot \frac{1 - M_{c2}^2}{M_{c2}^2}\right)\left(\frac{\vec{U}_2}{|U_\infty|} \circ \mathfrak{k}\right) \cdot \cos \gamma \cos \phi \tag{33}$$

For the solution, we can express the term $\left(\frac{\vec{U}_2}{|U_{c\infty}|} \circ \mathfrak{k}\right)$ in two

different equations, which when substituted in (33) then result in two equations for the unknowns M_{e2}, γ and Φ . By using equation (30, we have

$$\frac{\vec{U_2}}{|U_\infty|} \cdot \vec{\varphi} = a \sin \gamma \cos \Phi + b \cos \gamma \cos \Phi + c \sin \Phi \qquad (34)$$

If we use the magnitudes of the Mach numbers, then we obtain

$$\frac{\vec{U_2}}{|U_\infty|} \circ \vec{\varphi} = \frac{|U_e|}{|U_\infty|} \cdot \frac{M_{e2}\, a_2}{|U_e|} \cdot \frac{|U_2|}{M_2 \cdot a_2} = \frac{M_{e2}}{M_2} \cdot \frac{|U_2|}{|U_\infty|} \qquad (35)$$

Then we obtain the following two equations

$$\frac{2}{\varkappa + 1} \frac{M_{e2}^2 - 1}{M_{e2}} = \frac{b \cdot M_2}{\dfrac{|U_2|}{|U_\infty|} \cdot \cos \gamma \cos \Phi} \qquad (36)$$

and

$$\frac{\varkappa + 1}{2} \frac{M_{e2}^2}{M_{e2}^2 - 1} = \cos^2 \gamma \cos^2 \Phi + \frac{c}{b} \cos \gamma \sin \Phi \cos \Phi$$
$$+ \frac{a}{b} \sin \gamma \cos \gamma \cos^2 \Phi \qquad (37).$$

By specifying an initial value, we can determine the unknowns in (36) and (37) using an iteration (Appendix III). The leading edge shock gives an additional velocity component in the negative y-direction, whereas the subsequent Prandtl-Meyer expansion gives components in the positive y-direction. Therefore, an expansion surface has to exist on which the direction vectors are parallel to the incident flow. Wherever the expansion surface intersects the shock surface, the shock intensity has to be zero. At this position, we have $M_{e2} = 1$ and $\vec{U_2} \circ \vec{i} = 0$, , so that from equations (34) and (35), we find

/72

$$a \sin \gamma \cos \Phi + c \sin \Phi = \frac{1}{M_2} \cdot \sqrt{a^2 + c^2} \qquad (38)$$

82

The velocity vector is

$$\frac{\vec{U}_{so}}{|U_{\infty}|} = a_{so}\vec{i} + c_{so} \cdot \vec{k},$$

and is parallel to the symmetry plane with the inclination

$$\alpha_{so} = \arctan\left(\frac{c_{so}}{a_{sc}}\right).$$

The corresponding Mach number M_2 forms a Mach cone, and the tip of the model or the coordinate origin is located on its generator. In this way the shock angle γ_{so} can be given as follows in the x-y-plane

$$\gamma_{so} = \arctan\sqrt{\tan^2\mu_{so} - \tan^2\alpha_{so}}$$

The inclination angle Φ_{so} has to be determined from a solution of equation (38). If we calculate the corresponding positions in the coordinate system, then all initial values are given for iteration to determine the internal shock.

In this iteration, we first assume that the inclination of the shock Φ is constant, or the value is used from the previous calculation. From equations (36) and (37), we then find an additional point of the shock surface in the cross-section plane. The connection line between the new and the old shock points produces the inclination angle which has to be varied until the value used in the calculation equations and which is the result of the geometry coincides within certain limits.

The shock shape and positions can then be determined in the manner described. The velocity vector behind the internal shock is then found from equations (31), (35) and (36)

$$\frac{\vec{U_3}}{|U_\infty|} = a\vec{i} + b\vec{j} + c\vec{k} + \frac{b}{\cos\gamma\,\cos\phi}\,(\vec{i}\,\sin\gamma\,\cos\phi + \vec{j}\,\cos\gamma\,\cos\phi + \vec{k}\,\sin\phi)$$

from which it follows that

$$\frac{\vec{U_3}}{|U_\infty|} = \vec{i}\,(a - b\tan\gamma) + \vec{k}\,(c - b\,\frac{\tan\phi}{\cos\gamma}) \tag{39}$$

The magnitude of Mach number is determined in a similar way as was done with equation (28), so we obtain

$$M_3 = (\frac{2}{\varkappa+1})^{1/2}\cdot M_3^*\,(1 - \frac{\varkappa-1}{\varkappa+1}\cdot M_3^*)^{-1/2} \tag{40}$$

where

$$M_3^* = \frac{|U_3|}{a^*} = \frac{|U_3|}{|U_\infty|}\cdot\frac{|U_\infty|}{a^*}$$

and $|U_\infty|/a^*$ is defined by equation (28a).

The pressure increase above the internal shock is the reason for the thickening of the boundary layer in the central region. Here there is an expansion which results in a velocity component in the direction towards the symmetry plane. Therefore, the equations for the internal shock have to be expanded so that a larger deflection of the flow is achieved and so that $\vec{U_4}\circ\vec{i} = 0$ only occurs after the expansion.

Using the condition $\vec{U_3}\circ\vec{j} \neq 0 = -K$, instead of equation (33) we obtain

$$-K = b + (\frac{2}{\varkappa+1}\,\frac{1-M_e^2}{M_e^2})(\frac{\vec{U_2}}{|U_\infty|}\circ\vec{k})\cdot\cos\gamma\,\cos\phi \tag{41}$$

and therefore for equation (36), we obtain

$$\frac{2}{\varkappa+1}\,\frac{M_{e2}^2-1}{M_{e2}} = \frac{(b+K)\,M_2}{\frac{|U_2|}{|U_\infty|}\cdot\cos\gamma\,\cos\phi}$$

and finally the velocity vector behind the internal shock is

$$\frac{\vec{U_3}}{|U_\infty|} = \vec{i}\,(a - (b + K)\tan\gamma) + \vec{j}\,(b - (b + K))$$
$$+ \vec{k}\,(c - (b + K))\,\frac{\tan\vartheta}{\cos\gamma} \qquad (42)$$

With an appropriate iteration, we have to determine the value K in such a manner that after the internal expansion, one obtains a vector parallel to the symmetry plane, as discussed above.

The inner expansion

The displacement boundary layer downstream of the internal shock is again considered as a fixed body surface at which the internal expansion occurs. The form of the boundary layer in this region is given in various ways (Cross, Collis: Fig. 7) and will be described by means of an ellipse with a principal axis in the symmetry plane. The equation of the ellipse can be determined from two points. From the intersection point between the internal shock and the boundary layer, we find the "separation point" which is also on the thickened boundary layer. The second point is defined by the displacement thickness in the symmetry plane δ_{cL}^{*} which was determined in various experiments. Figure 76 shows the dependence of the thickening on angle of attack for different Mach numbers. As an approximation, we can obtain the following equation from this:

$$\frac{\delta_{cL}^{*}}{s} = 0.97 \cdot M_\infty^{1/2} \cdot \alpha + 0.001\, M_\infty^2 \qquad (43)$$

If the coordinates of the separation point $S\,(\,y_{0s}/z_{0s}\,)$ and of the point on the symmetry plane $S_{cL}\,(\,y_{cL}/\delta_{cL}^{*}\,)$ are known, then the ellipse equation is

$$\frac{(y - y_{CL})^2}{a^2} + \frac{z^2}{\delta_{CL}^{*2}} = 1 \tag{43a}$$

where

$$a^2 = (y_{OS} - y_{CL})^2 \cdot \left(\frac{\delta_{CL}^{*2}}{\delta_{CL}^{*2} - z_{OS}^2} \right)$$

In the continued calculation in the central region of the wing, we have to distinguish whether the velocity components reach supersonic or subsonic speeds in the cross-section plane. We will discuss both cases.

In the case of supersonic speeds, the calculation is similar as already given for the expansion above the boundary layer in the outer region, in which first the ellipse is replaced by small straight-line segments. Starting from variable behind the internal shock, the Prandtl-Meyer expansion then gives the Mach number M_{4e} and the local flow angle ϕ_4.

The velocity vector and the total Mach number are then found from the following trial solution. The velocity vector behind the internal shock was

$$\frac{\vec{U_3}}{|U_\infty|} = \vec{i} \cdot d + \vec{k} \cdot e$$

where d and e are defined by equation (39).

In the cross-section plane perpendicular to the inner shock. we than find

$$\begin{aligned}
\frac{\vec{U_3}}{|U_\infty|} = \vec{l}_i (d \cdot \cos \alpha \sin \gamma + e \sin \alpha \sin \gamma) \\
+ \vec{m}_i (d \cos \alpha \cos \gamma + e \sin \alpha \cos \gamma) \\
+ \vec{n}_i (-d \sin \alpha + e \cos \alpha)
\end{aligned} \tag{44}$$

Since again we assume that the tangential component above the internal shock does not change, we obtain the following for the speed

$$\vec{U}_4 = \vec{U}_3 + (\vec{U}_{4e} - \vec{U}_{3e})$$

If we define

$$\frac{\vec{U}_{4e}}{|U_{4e}|} = \vec{m}_4 \cos \varphi_4 - \vec{n}_4 \sin \varphi_4$$

and if $\vec{U}_{3e} / |U_\infty|$ is given by the $\vec{m}_4$- and $\vec{n}_4$-components in equation (44), then we find

$$\frac{\vec{U}_{4e} - \vec{U}_{3e}}{|U_\infty|} = (\vec{m}_4 \cos \varphi_4 - \vec{n} \cdot \sin \varphi_4) \cdot g(M_{4e})$$
$$- \vec{m} (d \cos \alpha \cos \gamma + e \sin \alpha \cos \gamma)$$
$$- \vec{n} (e \cos \alpha - d \sin \alpha)$$

with

$$g(M_{4e}) = \frac{M_{4e}}{M_\infty} \sqrt{\frac{1 + \frac{\varkappa-1}{2} M_\infty^2}{1 + \frac{\varkappa-1}{2} M_{4e}^2}}$$

In this way, we can write the velocity vector in the central region of the wing as follows:

$$\frac{\vec{U}_4}{|U_\infty|} = \vec{\ell}_4 (d \cos \alpha \sin \gamma + e \sin \alpha \sin \gamma)$$
$$+ \vec{m}_4 (g(M_{4e}) \cos \varphi_4) - \vec{n} (g(M_{4e}) \cdot \sin \varphi_4) \qquad (45)$$

The complete equation in the aerodynamic coordinate system /76 is contained in Appendix IV.

The magnitude of the Mach number is found from

87

$$M_4 = \left(\frac{2}{\varkappa+1}\right)^{1/2} \cdot M_4^* \left(1 - \frac{\varkappa-1}{\varkappa+1} M_4^{*2}\right)^{-1/2} \qquad (46)$$

with

$$M_4^* = \frac{|U_4|}{a^*} = \frac{|U_4|}{|U_\infty|} \cdot \frac{|U_\infty|}{a^*}$$

For low incident speeds, around $M_\infty \approx 4$, we obtain subsonic speed in the central part of the wing in the plane perpendicular and downstream of the internal shock. The calculation of the flow variables in this case is done using the panel method and will now be described.

The velocity field can be represented as the sum of the velocity behind the shock $\vec{U}_3$ and the perturbation velocity $\vec{U}_s$ given by the elliptical thickening of the displacement boundary layer,

$$\vec{U}_4 \quad \vec{U}_3 + \vec{U}_s \quad .$$

The calculation of the perturbation field $\vec{U}_s$ is done using potential theory, and a disturbance potential is introduced, which for example can be produced by a source distribution on the surface of the boundary layer. Then we can establish an integral equation

$$2\pi q_i - \iint \frac{\partial}{\partial n}\left(\frac{1}{r_{ij}}\right) \cdot q_j \, d0 = -\vec{n}_i \, \vec{U}_3 \qquad (47)$$

whose physical meaning is shown in Fig. 77. The right side of this equation is the normal component of the incident flow at the point i. The left side, first of all, consists of the term $2\pi q_i$, which is the normal velocity component directed outwards, caused by the source intensity in the immediate vicinity of the same point. The surface integral, on the other hand, is the component which results from the source distribution at the points j on the remaining body surface at the point i.

Since equation (47) cannot be solved analytically for arbitrary body shapes, the panel method [85] is used, and the body surface is divided into a number of plane surfaces. On each of these panels, one assumes a constant source intensity with an unknown value, and then q_1 can be placed ahead of the integral. The integral over the individual point is then reduced to a geometric problem which can be solved simply. We then find a system of linear equations

$$\sum_{j=1}^{N} q_j \cdot a_{i,j} = -\vec{n}_i \cdot \vec{U}_3 \tag{48}$$

which is an approximation to the integral equation (47). The physical meaning of the individual terms is also shown in Fig. 77. An additional description of the method used here is given in [86].

The solution of equation (48) gives the velocity field in the cross-section plane so that together with the tangential speed, the total vector $\vec{U}_4$ can be represented by

$$\frac{\vec{U}_4}{|\vec{U}_\infty|} = \vec{l}_4 \, (d \cos \alpha \sin \gamma + c \sin \alpha \sin \gamma)$$
$$+ \vec{m}_4 \, (\vec{U}_s \circ \vec{m}_4) + \vec{n}_4 \, (\vec{U}_s \circ \vec{n}_4) \tag{49}$$

The corresponding Mach number distribution is then found again from equation (46).

In the previous section, we already discussed that the flow around the boundary layer thickening induces an additional component in the direction of the symmetry plane and therefore $\vec{U}_4 \circ \vec{i} \neq 0$ ist. The shock has to be iterated in such a manner that it produces an additional component in the direction of the leading edge. According to equation (42), in the calculation of the inner expansion we have to include the $\vec{j}$-component of the vector $\vec{U}_3$. The speed $\vec{U}_4$ then only changes in the $\vec{l}_4$ direction. This equation is also discussed for the aerodynamic coordinate system in Appendix V.

89

Static pressure and total pressure in the flow regions

In the previous sections, we discussed the velocity vectors and Mach numbers in the entire flow field, and therefore we can now calculate the static pressures and the total pressures in the individual regions. In the following the index (∞, 1,2,3,4) refers to the flow region and (p) refers to the Pitot pressure behind a normal shock.

Behind a leading edge shock, we obtain the following for the /78 static pressure ratio:

$$\frac{p_1}{p_\infty} = \frac{2\varkappa\, M_{s_1}\cdot \sin^2 \beta_s - (\varkappa - 1)}{\varkappa + 1} \tag{50}$$

For the total pressures, it makes more sense to give the ratio of the Pitot pressures in order to make comparison with experiments

$$\frac{p_{p_1}}{p_{p_\infty}} = \frac{p_{p_1}}{p_1} \cdot \frac{p_1}{p_\infty} \cdot \frac{p_\infty}{p_{p_\infty}} \tag{51}$$

so that according to the shock relationships, we have

$$\frac{p_{p_1}}{p_1} = f\,(\hat{M}_{s_1})$$

$$\frac{p_1}{p_\infty} = f\,(M_{s_1}\cdot \sin \beta_s)$$

$$\frac{p_p}{p} = f\,(M_{s_1})$$

In the outer expansion region in the vicinity of the leading edge, the static pressure ratio is found from a series expansion for an expansion over small deflection angles $\Delta \nu$. The Mach number $M_{E_{1-1}}$ is the one of the preceding expansion

90

$$\frac{p_2}{p_1} = 1 - \frac{\varkappa M_{E_{i-1}}^2 \frac{i+1}{2}}{\sqrt{M_{E_{i-1}}^2 - 1}} \cdot \Delta v + \varkappa M_{E_{i-1}}^2 \frac{(\varkappa+1) M_{E_{i-1}}^4 - 4(M_{E_{i-1}}^2 - 1)}{4(M_{E_{i-1}}^2 - 1)^2} \Delta v^2 - \ldots \qquad (52)$$

from which we find

$$\left(\frac{p_2}{p_\infty}\right)_i = \left(\frac{p_2}{p_1}\right)_i \cdot \left(\frac{p_2}{p_1}\right)_{i-1} \cdot \frac{p_1}{p_\infty}$$

For the Pitot ratio, we can then essentially use equation (51). The outer expansion only causes the Mach number behind the leading edge shock to change and therefore we have

$$\frac{P_{P2}}{P_{P_\infty}} = \frac{P_{P2}}{P_2{}'} \cdot \frac{P_2}{P_1} \cdot \frac{P_1}{P_\infty} \cdot \frac{P_\infty}{P_{P_\infty}} \qquad (53)$$

where

$$\frac{P_{P2}}{P_2} = f(M_E)$$

and $P_2/P_1 = 1$ is an isentropic state change.

The static pressure ratio over the <u>internal shock</u> is again /79 given by the shock relationships and is the following, referred to the incident flow pressure:

$$\frac{p_3}{p_\infty} = \frac{p_3}{p_2} \cdot \frac{p_2}{p_\infty} \qquad (54)$$

where $P_3/P_2 = f(M_{e2})$, where M_{e2} is the perpendicular component ahead of the internal shock. The Pitot pressure ratio can then be determined from

$$\frac{P_{P3}}{P_{P_\infty}} = \frac{P_{P3}}{P_3} \cdot \frac{P_3}{P_2} \cdot \frac{P_2}{P_{P2}} \cdot \frac{P_{P2}}{P_{P_\infty}} \qquad (55)$$

where

$$\frac{P_{P3}}{P_3} = f(M_{e3})$$

and

$$\frac{P_3}{P_2} = f(M_{e2})$$

where M_{e3} is the normal component behind the internal shock.

In the region of <u>internal expansion</u> in the vicinity of the symmetry plane, as already discussed in the previous section, there will be subsonic speeds and supersonic speeds. Therefore, in the case $M_{4e} > 1$, we use the equations of Prandtl-Meyer expansion for the static pressure, as already done in (52).

If subsonic speed prevails $M_{4e} < 1$, then we find

$$\frac{P_4}{P_\infty} = \left[0.7 \, M_{e3}^2 \left(1 - \frac{U_4^2}{U_3^2}\right) + 1 \right] \cdot \frac{P_3}{P_\omega} \qquad (56)$$

The Pitot pressure ratio in supersonic flow is

$$\frac{P_{P4}}{P_{P_\infty}} = \frac{P_{P4}}{P_4} \cdot \frac{P_4}{P_3} \cdot \frac{P_3}{P_{P3}} \cdot \frac{P_{P3}}{P_{P_\infty}}$$

where

$$\frac{P_{P4}}{P_4} = f(M_{e4})$$

and $p_4/p_3 = 1$, because here again an isentropic state change has occurred. For the case where subsonic Mach numbers $M_{4e} < 1$ exists, the Pitot pressure ratio does not change and then corresponds to P_{P3}/P_{P_∞}.

In all regions of the wing, we wrote the static pressure as a <u>/80</u> coefficient C_p to better compare it with experiments, which is

92

defined by

$$c_p = \frac{\dfrac{p}{p_\infty} - 1}{0.7\, M_\infty^2}$$

This means we have now given the most important flow variables for a comparison with experimental results and other theoretical results on the lee side.

7. Discussion of the theoretical results and comparison with experiments

In the discussion of the theoretical results, we will first describe the influence of the simplifications used in the calculations in the form of empirical equations or fixed data. For an example, we will then describe the complete theoretical flow field which was determined and will carry out a variation of the most important input variables. Finally, we will give a comparison with other theories and experiments, including those which are outside of the definition region of the present calculation.

The empirically determined equations which were used in the calculation method agree quite well with the various experiments, but at this point we have to examine whether deviations have an effect on the theoretically calculated flow field. Four components of the flow model have been determined empirically: thickening of the boundary layer behind the internal shock, displacement thickness ahead of the internal shock, inclination angle Φ_s and trace angle Λ_t of the leading edge shock.

The thickening of the boundary layer downstream of the internal shock in the vicinity of the symmetry plane has a very small effect on the remaining flow field. We will discuss the effects on the pressure coefficient due to this when we make comparisons with experiments.

The determination of the displacement boundary layer upstream of the internal shock was based only in part on empirical knowledge, because the thickness was derived from the simplified boundary layer equations [84]. This trial solution seems to be justified for the flow model, as the evaluation of control calculations in Fig. 78 shows. Here, we summarize the influences of various /81 displacement thicknesses $\delta_{s_0}^*/s$ on the pressure coefficients and the position of the internal shock. In addition to the value $\delta_{s_0}^*/s$ from equation (19), which in the figure is indicated by ①, we show a comparison value which is about twice as large, indicated by ② . From the sketch on the left of the figure in the upper diagram, we can see that the initial point of the internal shock A varies greatly in the z-direction, which however barely has an influence on the further calculation. The base point of the internal shock F (a measure for the trace angle γ) changes only slightly in the y-direction. In the upper diagram, we show a pressure coefficient upstream of the internal shock which changes only a maximum of 3% with respect to the value at ① . The greatest influence when varying the displacement thickness is exerted on the pressure coefficient just downstream of the internal shock. Here we can observe deviations from the value at ① which amount to between 5% and 10%, which however still lie within the order of magnitude of the measurement accuracy of the experiments.

The influence of the inclination angle Φ_s of the leading edge shock is treated in the same way in Fig. 79. The average empirical value is $\Phi_s = 5°$, which was used in the calculations, and it is marked in the figure. The lower diagram shows the effects of various inclination angles on the position of the internal shock. The initial point A changes its position in the z-direction only inconsequentially. Also, the base point of the internal shock is almost constant and only at large inclination angles Φ_s can we find deviations of around 10% in the average value. This is also true for pressure coefficients in front of and behind the internal shock which are shown in the upper diagram. As already shown in the displacement thickness variation discussion, influences on the pressure

coefficient are greater downstream than upstream of the internal shock. Nevertheless, we can still find a small deviation in the pressure coefficients compared with the comparison values. The angle $\Phi_s = 5^\circ$ can therefore be further used in the calculation equations, because even for changes in the real flow by $\Delta\Phi_s = \pm 5^\circ$ we only find small influences on the flow field determined from theory.

The greatest effects on the pressure coefficients and position of the internal shock are obtained when one varies the trace angle Λ_s of the leading edge shock. This is understandable if we consider that the values perpendicular to the shock plane form the departure values for the entire calculation. Figure 80 shows an evaluation made for the other parameters, and the trace angle Λ_s was varied between 65° and 70°. The value determined from equation (10) for the prevailing incident flow conditions and geometric conditions is $\Lambda_s = 67.3^\circ$. From Fig. 73, in which according to equation (10) the angle Λ_s is represented as a function of Mach number, we can see that for the selected delta wing sweepback, in the range $\Lambda_s > 68^\circ$, small changes in the trace angle lead to a strong increase in Mach number. For $\Lambda_s > 68^\circ$, a change in the trace angle has a small influence. This result is also reflected in the lower diagram of Fig. 80 for the position of the internal shock. For $\Lambda_s > 68^\circ$, the initial point and base point change more with increasing trace angle than in the range $\Lambda_s > 68^\circ$. For the pressure coefficients (upper diagram), this means that the values ahead of the internal shock are influenced relatively little, but according to the position change, strong pressure differences downstream of the internal shock occur. This means that we have a substantial influencing of the flow field by the parameter Λ_s , so that it seems unavoidable to carry out the most accurate calculation of this value possible. On the other hand, Fig. 73 has shown that with equation (10), we can obtain quite a good approximation, which results in a deviation of $\Delta\Lambda_s = \pm 1^\circ$ with respect to experiments. The resulting error is justifiable for the pressure distributions

but for the base point of the internal shock, we obtain position changes of a maximum of 30% referred to the comparison value. At this point, with the available information we cannot yet decide about the feasibility of the calculation method. Only a subsequent comparison of theoretical and experimental results will allow a complete evaluation.

The theoretically determined flow field on the lee side of a delta wing is shown in Fig. 81 for $M_\infty = 3.5$ and $\alpha = 14.5^\circ$. For the selected incident flow conditions, we have a separated leading edge shock, through which the velocity component in the cross-section plane undergoes an additional deflection. Along the displacement boundary layer, the flow expands, and over the wing, regions with different velocity result. On the first expansion wave shown, we find the initial point A of the internal shock, which here at the same time is part of the Mach cone of the incident flow. The further course of the internal shock is described by a curved line. Downstream of the internal shock, we again have a deflection of the flow because of the thickened boundary layer, until   symmetry conditions are achieved in the central plane.   /83 Arrows indicate the most interesting positions and they indicate the size and direction of the speed. This flow field is, in principle, maintained for all of the incident flow conditions specified.

Figure 82 shows the pressure coefficients over the span from experiment and theory at two Mach numbers. We can see that for an average angle of attack ($\alpha \sim 12^\circ$), the pressure coefficients are comparable both in the expansion region and in the central region. At high angles of attack ($\alpha \sim 20^\circ$) in the expansion of the wing, we still find a similar pressure level for the experiment and the theory, but from the theory we find pressure increases over the internal shock which are too high. In contrast to the theoretical results, the pressure distributions which are the result of experiments are continuous over the span. Discontinuous pressure increases from the calculation are obtained in the region of the

96

internal shock. In the real flow, there is a pressure equalization inside the boundary layer in this region. If we also assume that the shock in the vicinity of the boundary layer consists of individual compression waves, then we find the variation of an isentropic compression which is indicated in the upper diagram.

When introducing the calculation method in the previous chapter, we first presented a simple method based on expansion equations and shock equations. The flow model was greatly simplified. For $M_\infty = 4$ and $\alpha = 12.2^\circ$ we then obtained a result which is also given as an example in Fig. 82. It will be shown that compared with experiment, we have an expansion which is too great and that the shock positions and pressure increases are not comparable.

A comparison with the theory of Babayev [53] is shown in Fig. 83. On the basis of the inclusion of the displacement boundary layer in the previous report and the centered Prandtl-Meyer expansion at the leading edge in the theory of Babayev, we find substantial differences in this wing region. Ahead of the internal shock, we achieve almost the same pressure coefficients but different positions and intensities of the internal shock. The other pressure distributions shown are quite close to one another in the expansion region and are very different in the central region. On the other /84 hand, the linear theory is already outside of its validity range $(M_\infty^2 < 10)$ and results in pressure coefficients which are below those of a vacuum. Oil film photographs of Rao and Whitehead [5] (with somewhat changed sweepback and angle of attack) give an indication of the position of the internal shock. This is indicated by an arrow in the diagram. We have shown, therefore, that the individual theories give completely similar results. However, in this calculation example, we have no experimentally determined presssure distributions and we cannot evaluate the individual trial solutions.

In the previously discussed pressure distributions, it has become clear that the vortex position and shock position cannot be

determined uniquely. The pressure distributions show a pressure equalization over the boundary layer and the oil film photographs also only give wall stream lines within the boundary layer. It can be assumed that the position of the vortex and the shock will occur in the same direction when the incident flow conditions are changed. On this basis, Fig. 84 gives a comparison of the position of the base point of the internal shock and the positions of the vortex centers determined from oil film photographs. The basis for this are the results from the CUED wind tunnel shown in Fig. 32 for a fixed Mach number and different angles of attack. We find a good agreement between the change in the vortex center and the internal shock in the span direction. The assumption of Cross [49] that the separation lines are displaced in the direction of the leading edge is therefore supported. This is not necessarily contradictory to the available pressure distributions if one assumes that because of the thicker boundary layers, the influence of a shock on the surface is greatly decreased. The pressure increase in the central region is created essentially by the vortices inside the boundary layer and is substantially below the values which were achieved above the internal shock. We have to point out that with increasing angle of attack, the shock intensity in the present calculation as well as according to the theory and experiments of Fowell [52] increase.

When one varies the angle of attack, one finds quite good agreement (see lower diagram in Fig. 84) between the height positions of the vortex center and of the base point of the internal shock. Based on the flow model, it is understandable that the base point of the shock will always be above the vortex center.

From the previous results, we can already see that the calculation results in usable results even for angles of attack of $\alpha < 12^\circ$, i.e., outside of the definition range. As an example of this, we show the experimental Pitot isobars determined by Monnerie and Werle [75] as well as the theoretical flow field, Fig. 85. As

98

already described above with the ILR results, even here the Pitot pressure values show a separation bubble (Mannerie and Werle, separated region) at the leading edge and attached flow in the central region, and their positions from oil film photographs and Schlieren photographs are also indicated. From the theory, we find that the displacement thickness ahead of the internal shock is almost identical with the dimensions of the separation bubble, but downstream of the internal shock we assumed a boundary layer (i.e., a thickening) which is parallel to the surface. Overall, we find good agreement between the expansion region and the position of the internal shock, but for the central region we cannot make any determination except the indication flow direction (in a plane perpendicular to the internal shock).

Finally, in Fig. 86 we show how the flow field changes when one varies the angle of attack or the incident Mach number. For a fixed angle of attack $\alpha_1 = 14.5^\circ$, the figure shows on the left side the Mach number which was increased from $M_\infty = 4$ to 7. The leading edge shock moves in the direction towards the wing and therefore slightly increases the normal angle of attack ($\Delta\alpha_N \sim 3^\circ$). The simultaneous increase in the normal component of Mach number brings about a strong increase in the deflection angle through the leading edge shock, so that a stronger expansion is necessary until that expansion surface is reached on which the internal shock has zero intensity. The expansion of the internal shock in the z-direction is smaller based on the thicker displacement boundary layer, whereas at the same time there is a slight displacement in the direction of the symmetry plane.

As already mentioned, the influence of the angle of attack on the leading edge shock is small, so that for it we have an almost constant position on the right sketch of Fig. 86. The variation in the angle of attack from $\alpha = 12.5^\circ$ to 20° brings about a relatively continuous increase in the normal angle of attack, whereas

the corresponding Mach number changes only slightly. Based on these conditions, even behind the leading edge shock one obtains an almost continuously changing flow parameter collection, so that the internal shock is displaced uniformly in the direction of the leading edge. In this way we were able to show how the flow field behaves when one varies two incident flow parameters. /86
The trends which were found have been confirmed by experiments.

Summarizing, we can say here that the empirically determined equations used in the calculation for the most part have a small influence on the most important quantities of the flow field. One exception to this is the trace angle of the leading edge shock Λ_s, which greatly influences the position of the internal shock. However, comparisons with the experiments have shown that the position of the internal shock is well represented by the present calculation method. As far as the pressure distribution is concerned, over the entire definition region we find good agreement for the pressure level in the expansion region. The pressure values downstream of the internal shock in the central region of the wing are comparable up to a maximum angle of attack of $\alpha \sim 15°$. The relatively high complexity of the calculation method compared with other theories with greatly simplified flow models is therefore justified, because both the flow field as well as the pressure distribution, for the most part, agree better with experiments.

8. Summary

In the present report we discussed lee side f⁻ w over delta wings under supersonic conditions, both experimentally and theoretically. Since not much work has been done in this area, it was the purpose of this investigation to review present-day knowledge and to extend the information known about the flow field.

The experimental part included thick delta wings with different

cross-section shapes, and the experiments were essentially carried out in two different wind tunnels. The experiments with the delta wing with a flat top side were used to analyze the flow types for the different incident flow conditions. The Stanbrook-Squire region was used as a basis of this, which separates leading edge vortex formation and shock-induced vortex formation. The evaluation of the experiments showed the following:

O   Confirmation of the region to the left of the Stanbrook- /87
     Squire region (M_∞ = const, α = variable) with leading edge
     separation into primary and secondary vortices. However,
     at the higher angles of attack, we found a change in the
     type of flow. Here we find a shock which is almost
     parallel to the surface in the symmetry plane, which is
     the result of the downwards directed velocity components
     of the primary vortex. Instead of the secondary vortex,
     we only observe a dead-water region here.

O   Inside the Stanbrook-Squire region (M_∞ = variable, α = const)
     the flow field changes continuously, so that no fixed bound-
     ary for the change in the flow types can be given. However,
     the most noticeable change in the experiments was observed
     around the center of the transition region ($M_\infty \approx 3.0$).

O   To the right of the Stanbrook-Squire region (M_∞ = const, α =
     variable), we again found leading edge vortex formation for
     small angles of attack. When the angle of attack is in-
     creased, we find a flow type which deviates from the shock-
     induced vortex formation flow type after crossing a transi-
     tion region. Here we find a separation bubble at the lead-
     ing edge and an internal shock on top, for the most part in-
     dependent of one another. This type of flow is called
     "separation with shock" and lies to the right of this
     Stanbrook-Squire boundary only for average angles of attack,
     because at higher angles of attack we again assume vortex
     formation from the leading edge.

The experimental investigations with delta wings for non-flat (conical, delta-shaped) top sides were performed in the "separation bubble with internal shock" region. We were able to establish the following:

O   The lee side shape gives changed incident flow conditions in the cross-section plane. From this we find attached flow at the leading edge for the delta-shaped lee side together with a supersonic expansion. Downstream, the internal shock induces a separation with vortex formation.

O   The angle Θ between the ridge line and the plane of the leading edges can be defined for flat top sides and can define how "greatly delta-shaped" a lee side is. A change in this parameter only has a small influence on the geometry of the flow field.

O   In general the cross-section shape of the delta wings influences the aerodynamic properties very greatly. Excessively large angles Ψ between the top side and the bottom side perpendicular to the leading edge lead to stagnation points on the lee side, whereas the flow leads to complete separation over the wing for small angles Ψ . /88

O   For separated leading edge shocks, the shape of the underside has an influence on the lee side flow which should not be ignored. However, in the higher Mach number range, because of the position of the stagnation lines on the underside, it is justified to treat both sides separately.

In a few experiments, we observed strong pressure increases above the entire span which had not been previously observed and therefore we made additional investigations of this phenomenon.

For certain incident flow conditions, we found that even for supersonic speeds, disturbances in the tail region can influence the lee side flow downstream of the trailing edge.

The theoretical results were restricted to the "separation bubble with internal shock" region and are based on a flow model which was determined from the available experimental data. Empirically determined equations for the position and shape of the leading edge shock, as well as for the displacement boundary layer, were substituted. The resulting calculation equations for the velocity distribution over the lee side had to be solved using an iteration process. Comparisons with experimental pressure distributions and flow fields show good agreement for the expansion region and for the position of the internal shock up to medium-sized angles of attack ($\alpha \sim 15^{o}$). At higher angles of attack, on the other hand, the pressure jump over the internal shock is very strong and can hardly be compared with the measured pressure distributions over the span which are almost uniform. However, the flow conditions are, for the most part, not clarified for this region.

For future work, therefore, we have shown that the Stanbrook-Squire region is not the only limit between the various flow types. In particular, we should point out the region of small or very large angles of attack, in which apparently substantial changes in the flow field exist. In addition, we have to point out the influence of the Re number, which in the present report was only discussed with regard to the different wind tunnels. In addition, the knowl- /89 edge of the flow fields allows one to investigate the influence of the tail region disturbances on the lee side flow. We have not obtained a thorough understanding about the mechanism of this phenomenon.

1. Whitehead, A. H., Keyes, J. W. Flow phenomena and separation over delta wings with trailing-edge flaps at Mach 6. AIAA Journ. vol. 6, No. 12, pp. 2380, Dec. 1968.

2. Whitehead, A. H. Effect of vortices on delta wing lee side heating at Mach 6. AIAA Journ., Vol. 8, No. 3, pp. 599, March 1970.

3. Whitehead, A. H., Bertram, M. H. Alleviation of vortex induced heating to the lee side of slender wings in hypersonic flow. AIAA Journ. Vol. 9, No. 9, pp. 1870, Sept. 1971.

4. Rao, D. M. Hypersonic lee surface heating alleviation on delta wings by apex drooping. AIAA Journ. Vol. 9, No. 9, pp. 1875, Sept. 1971.

5. Rao, D. M., Whitehead, A. H. Lee side vortices on delta wings at hypersonic speeds. AIAA Journ. Vol. 10, No. 11, Nov. 1972.

6. Whitehead, A. H., Hefner, J. N., Rao, D. M. Lee surface vortex effects over configurations in hypersonic flow. AIAA Paper 72-77, 1972.

7. --- Space Shuttle Aerothermodynamics Technology Conference, Vol. II - Heating, NASA TMX-2507, Dec. 1971.

8. Hefner, J. N. Lee surface heating and flow phenomenon on space shuttle arbiters at large angle of attack and hypersonic speeds. NASA-TND-7088, Nov. 1972.

9. Stanbrook, A., Squire, L. C. Possible types of flow at swept leading edges. Aeron. Quarterly, Vol. XV, Feb. 1964.

10. Squire, L. C. On the flow over delta wings. Gastvortrag am ILR, TU Berlin, June 1974.

11. Lindsey, W. F., Landrum, E. J. Compilation of information on the transonic attachment of flows at the leading edges of airfoils. NASA-TN-4204, Feb. 1958.

12. Earnshaw, P. B. An experimental investigation of the structure of a leading edge vortex. ARC R & M 3281, 1962.

13. Hall, M. G. A theory for the core of a leading-edge vortex. Journ. Fluid Mech., Vol. 11, 1961.

14. Drougge, G., Larson, P. O. Pressure measurements and flow investigation on delta wings at supersonic speed. FFA Rep. 57, 1956.

15. Thomann, H. Measurements of heat supply, eigen temperature and pressure distribution of delta wings at M = 3, FFA Rep. 93, Dec. 1962.

16. Okerbloom, T. I., Sarantsev, A. I. Some experimental results on the influence of Mach number on the vortical flow picture around a triangular wing and circular cone. IZV. AN SSSR, Mekh. Zhidk. i Gaza, No. 6, 1968.

17. Hurley, F. X. Vortex separation above delta leading edges. Journ. of Aircraft, Vol. 4, No. 2, March-April 1967.

18. Fellows, K. A., Carter, E. L. Results and analysis of pressure measurements on two isolated slender wings and slender wing-body combinations at supersonic speeds. ARA Rep. No. 12, Vol. 1, Nov. 1969.

19. Greenwood, G. H. Free flight measurements of pressure and heat transfer on the lee surface of a delta wing of incidence. (M = 1.0 to 3.6). RAE TR 68246, Oct. 1968.

20. Morris, D. W., Couch, L. M. Experimental pressure distribution on a blunt lifting-entry body at Mach 3.71. NASA TN D-4494, April 1968.

21. Gapcinski, J. P. Investigation of the flow phenomena over bodies at high angles of attack at a Mach number of 2.01. NASA RM L55 H29, Oct. 1955.

22. Lee, G. H. Notes on the flow around delta wings with sharp leading edges. ARC R & M 3070, 1955.

23. Jones, R. T. Properties of low aspect ratio pointed wings at speeds below and above the speed of sound. NACA Rep. 835, 1946.

24. Legendre, R. Flow near the tip of a highly swept-back A wing at moderate incidence angles. La Recherche Aeronautique, Bulletin Bimestriel, Nov. 1952 - Feb. 1953.

25. Adams, M. C. Leading edge separation from delta wings at supersonic speeds. Journ. Aeron. Sci., Vol. 20, No. 6, 1953.

26. Edwards, R. H. Leading edge separation from delta wings. Journ. Aeron. Sci., Vol. 21, No. 2, 1954.

27. Brown, C. E., Michael, W. H. On slender delta wings with leading edge separation. NACA TN 3430, April 1955.

28. Mangler, K. W., Smith, J. H. B. Calculation of the flow past slender delta wings with leading edge separation. RAE Rep. Aero 2593, May 1957.

29. Smith, J. H. B. Improved calculations of leading edge separation from slender delta wings. RAE TR 66070, 1966.

30. Nenni, J. P., Chee Tung. A second order slender wing theory for wings with leading edge separation in supersonic flow. NASA CR 1860, Sept. 1971.

31. Carafoli, E., Staicu, St. On the symmetrically deformed delta wing considering the flow separation at the leading edges. Rev. Roumaine des Sciences Techn. Serie de Mecanique Appliquee, Vol. 16, No. 6, 1971.

32. Pershing, B. Separated flow past slender delta wings with secondary vortex simulation. SSD - TDR - 64-151, Aug. 1964.

33. Küchemann, D. A non-linear lifting surface theory for wings of small aspect ratio with edge separations. RAE, Rep. Aero. 2540, 1955.

34. Squire, L. C. The estimation of the non-linear lift of delta wings at supersonic speeds. Journ. Roy. Aeron. Soc., Vol. 67, Aug. 1963.

35. Polhamus, E. C. Predictions of vortex-lift characteristics by a leading-edge suction analogy. Journ. of Aircraft, Vol. 8, No. 4, April 1971.

36. Coe, P. L., Jr. A vortex entrainment model applied to slender delta wings. AIAA Journ. Vol. 12, No. 1, Jan. 1974.

37. Hummel, D. Calculation of pressure distributions over slender bodies with arbitrary plan form and cross-section form in subsonic and supersonic flow. Inst. für Stromungstechnik, TU Braunschweig, Report 68/1, 1968.

38. Bannink, W. J., Nebbeling, C. An experimental investigation of the expansion flow field over a delta wing at supersonic speed. Rep. VTH-167, Delft Univ. of Techn., Sept. 1971.

39. Bannink, W. J., Nebbeling, C., Reyn, J. W. Investigation of the flow field on the expansion side of a delta wing with supersonic leading edges. Rep. VTH-128, Delft Univ. f. Techn., Aug. 1965.

40. Larcombe, J. M. Pressures near the centre-line of leeward surfaces on delta wings and conical bodies high supersonic speeds. ARC CP 1153, 1971.

41. Squire, L. C. Pressure distributions and flow patterns on some conical shapes with sharp edges and symmetrical cross-sections at M = 4.0. ARC R & M 3340, 1963.

/93

42. Squire, L. C. Pressure distributions and flow patterns at M = 4.0 on some delta wings. ARC R & M 3373, 1964.

43. Hefner, J. N. Effect of geometry variations on lee-surface vortex induced heating for flat-bottom three-dimensional bodies at Mach 6. NASA TN-D-7447, Nov. 1973.

44. --- Space shuttle aerothermodynamics technology conference. Vol. I Flow fields, Vol. III Aerodynamics, NASA TM X-2506 and 2508, Dec. 1971.

45. Pike, J. Experimental results from three cone-flow wave-riders. AGARD CP No. 30, Paper 12, May 1968.

46. Rein, J. A. Flow over the suction surface of sharp edge delta wings with detached leading edge shock waves. WRE TECHN. NOTE HSA 102, Australia, Dec. 1964.

47. Ghorai, S. C. Leading-edge vortices and shock-detachment flow over delta wings. Journ. of Aircraft, Vol. 6, May - June 1969.

48. Collis, D. C. A hypersonic wind tunnel study of a thick delta wing. ARI Aerodyn. note, no. 232, Nov. 1964.

49. Cross, E. J. Experimental and analytical investigation of the expansion flow field over a delta wing at hypersonic speeds. ARL 68-0027, Aerospace Research Lab., Feb. 1968.

50. Maslen, S. Supersonic conical flow. NACA TN 2651, March 1952.

51. Clarke, J. H., Wallace, J. Uniform second order solution for supersonic flow over delta wings using reverse flow integral methods. Journ. Fluid Mech. 18, pp. 225-238, 1964.

52. Fowell, L. R. Exact and approximate solutions for the supersonic delta wing. Journ. Aeron. Sci., Vol. 23, No. 8, Aug. 1956.

53. Babayev, D. A. Numerical solution of the problem of flow around the upper surface of a triangular wing by a supersonic stream. Zh. vych.mat., vol. 2, no. 2, 1962.

54. Pike, J. The flow past flat and anhedral delta wings with attached shockwaves. RAE TR 71081, April 1971.

55. Beeman, E. R., Powers, S. A. A method for determining the complete flow field around conical wings at supersonic and transonic speeds. AIAA 69-646, 1969.

56. Kutler, P., Lomax, H. A systematic development of the super-
       sonic flow fields over and behind wings and wingbody con-
       figurations using a shock-capturing finite-difference
       approach. AIAA Paper 71-99, Jan. 1971.

57. Walkden, F., Laws, G. T., Caine, P. Shock capturing numerical
       method for calculating supersonic flows. AIAA Journ.,
       Vol. 12, No. 5, pp. 642-647, May 1974.

58. Miyazawa, M. Lee surface flow phenomena over space shuttle
       oriented configurations at large angles of attack and
       hypersonic speeds. Ph.D. Thesis, New York Univ. University
       Microfilms No. 74-15931, 1974.

59. Christophel, R. G. Flow field on the lee side of a delta
       wing. AD-753 389, Air Force Institute of Technology,
       Dec. 1971.

60. South, J. C., Klunker, E. B. Methods for calculating non-
       linear conical flows. NASA SP 228, Paper 8, 1969.

61. Squire, L. C. Flow regimes over delta wings at supersonic
       and hypersonic speeds. Aeron. Quarterly, Vol. 27, pp. 1-1"
       Feb. 1976.

62. Werle, H. The bursting of apex vortices of a delta wing at
       low speeds. La Recherce Aeronautique, No. 74. Jan/Feb.
       1960.

63. Brooke-Benjamin, T. The explanation for the vortex breakdown
       phenomenon. ARC 22 802, May 1961.

64. Lawson, M. V. Some experiments with vortex breakdown. Journ.
       Roy. Aeron. Soc., Vol. 68, May 1964.

65. Peckham, D. H. Low speed wind tunnel tests on a series of
       uncambered slender pointed wings with sharp leading edges.
       ARC R & M 3186, Dec. 1958.

66. Wentz, W. H. Windtunnel investigations of vortex breakdown
       on slender sharp-edged wings. NASA CR-98 737, 1968.

67. Sarpkaya, T. Effect of the adverse pressure gradient on
       vortex breakdown. AIAA Journ. Vol. 12, No. 5, 602 ff,
       May 1974.

68. Brooke-Benjamin, T. The theory of vortex-breakdown phenomenon.
       Journ. Fluid Mech., Vol. 14, Part 4, pp. 593, 1962.

69. Jones, J. P. The breakdown of vortices in separated flow.
       ARC 22241, 1960.

70. Elle, B. J. On the breakdown at high incidences of the leading edge vortices on delta wings. Journ. Royal Aeron. Soc., Vol. 64, Aug. 1960.

71. Lambourne, N. C., Bryer, D. N. The bursting of leading edge vortices. ARC R & M 3282, 1962.

72. Craven, A. H., Alexander, A..J. An investigation of vortex breakdown at Mach 2. Cranfield Co A., Note Aero 158, Nov. 1963.

73. Szodruch, J. Investigation of lee side flow of slender delta wings for supersonic conditions. ILR-Mitt. 9, 1975.

74. Quincey, V. G., Callinan, J. Experiments with a Pitot rake at M = 1.6. Journ. Royal Aeron. Society, Dec. 1963.

75. Monnerie, B., Werle, H. Study of supersonic and hypersonic flow around a slender wing at incidence. AGARD CP No. 30, May 1968.

76. Szodruch, J., Squire, L. C. Pressure distribution on the suction surfaces of some delta wings at M = 3.5. ARC 35008, Jan. 1974.

77. Szodruch, J. Lee side flow field of delta wings with detached shock waves. Euromech 74 Colloquium, 1976.

78. Richards, I. C. Pressure measurements on the suction surface of a flat cone at M = 2.5. Cranfield Institute of Technology, College of Aeronautics, Co A Memo 7509, July 1975.

79. Lukasiewicz, J. Conical flow as a result of shock and boundary layer interaction on a probe. ARC R & M No. 2669, 1948.

80. Lawrence, G. C., Holdstock, A. C. Some observations of vortex bursting on the suction surface of a delta wing at M = 3.51. Students project, Aeronautics Laboratory, Cambridge University, April 1974.

81. Tracy, R. R. Hypersonic flow over a yawed circular cone. GALCIT, Memo No. 69, Aug. 1963.

82. Squire, L. C. Calculations of the pressure distribution on lifting conical wings with application to the off-design behavior of wave-riders. AGARD CP 30, May 1968.

83. Moeckel, W. E. Approximate method for predicting form and location of detached shock waves ahead of plane or axially symmetric bodies. NACA TN 1921, 1949.

84.   Cox, R. N., Crabtree, L. F. Elements of hypersonic aero-
       dynamics. English Universities Press Ltd., London 1965.

85.   Hess, J. L., Smith, A. M. O. Calculation of potential flow
       about arbitrary bodies. Progress in Aeronautical Sciences,
       Vol. 8, 1967.

86.   Güde, E. Forces applied by the engine inlet flow of VTOL
       aircraft for hovering flight conditions. ILR TN 4 (1974).

87.   Stollery, J. L., Richards, L. C. Sypersonic flow past a
       slender delta wing - on experimental study. ICAS Paper
       No. 76-24, Oct. 1976.

88.   Edward, J.B.W. Heat transfer and pressure measurements on
       the upper surface of a delta wing at incidence at Mach
       numbers between 2.0 and 3.6. RAE TR - 65 144, July 1965.

APPENDIX 1

The iteration of Mach number from the Prandtl-Meyer function for specified angle ν first requires the exact knowledge of the function $\nu = f (M)$. The first and second derivative is given in the following for $\varkappa = 1.4$:

$$\nu = \sqrt{6} \cdot \arctan \sqrt{\frac{M^2-1}{6}} - \arctan \sqrt{M^2-1}$$

$$\frac{d\nu}{dM} = \frac{5 \cdot \sqrt{M^2-1}}{M\,(M^2+5)}$$

$$\frac{d^2\nu}{dM^2} = 5\sqrt{M^2-1} \left\{ \frac{M^2\,(3-2M^2)+5}{M^2(M^2+5)^2 \cdot (M^2-1)} \right\}$$

From this it results that for $\nu = 0$ the function runs tangentially into the M-axis at $M = 1$ and has an inflection point for $M_W = 1.5812$ (at ν_W). Therefore, using the following flow diagram, any Mach number can be determined from the specified Prandtl-Meyer angle ν_B.
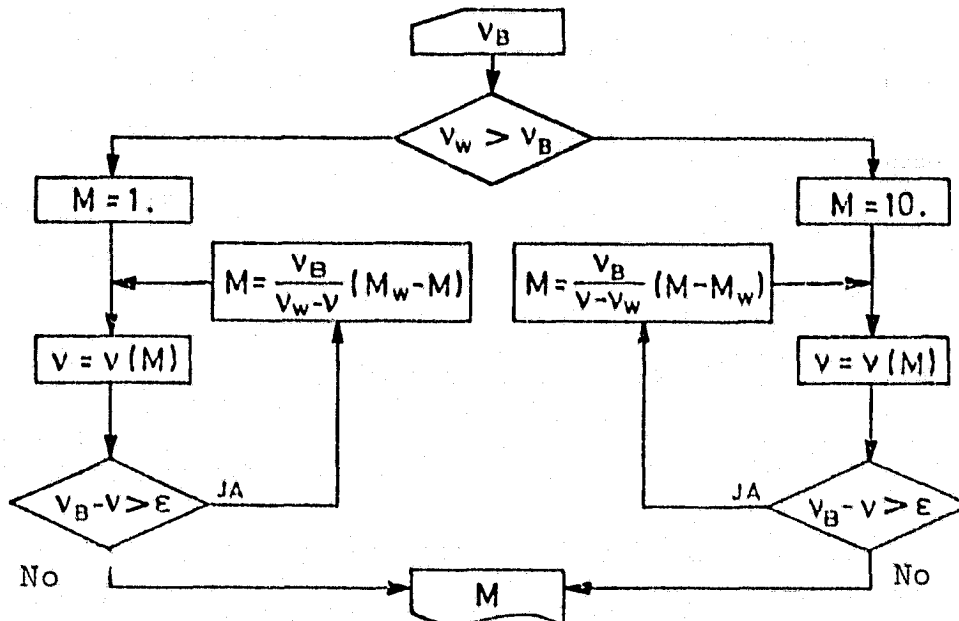
Here ε is a freely selectable accuracy constant.

APPENDIX II

The determination equation for the vector in the outer expansion range for the aerodynamic coordinate system according to equation (27) is:

$$\frac{\vec{U_2}}{|U_\infty|} = \vec{i} \left[1 + \cos \alpha \cos \Lambda \cos \Lambda_S (g(M_E) \cdot \cos \varphi - \cos \alpha_S) \right.$$
$$\left. + \sin \alpha \cos \Lambda_S (g(M_E) \cdot \sin \varphi - \sin \alpha_S) \right]$$
$$+ \vec{j} \left[\sin \Lambda \cos \Lambda_S (g(M_E) \cos \varphi - \cos \alpha_S) \right]$$
$$+ \vec{k} \left[\sin \alpha \cos \Lambda \cos \Lambda_S (g(M_E) \cos \varphi - \cos \alpha_S) \right.$$
$$\left. - \cos \alpha \cos \Lambda_S (g(M_E) \cdot \sin \varphi - \sin \alpha_S) \right]$$

APPENDIX III

Summarizing equations (36) and (37) results in an expression which only depends on the shock parameters γ and Φ:

$$\cos^2 \Phi \left(\cos^3 \gamma + \frac{a^2}{b^2} \sin^2 \gamma \cos \gamma \right) + \cos^2 \gamma \left(2 \frac{a}{b} \sin \gamma \cos^2 \Phi \right.$$
$$+ 2 \frac{c}{b} \cos \Phi \sin \Phi \right) + 2 \frac{ac}{b^2} \sin \gamma \cos \gamma \sin \Phi \cos \Phi - \frac{\varkappa+1}{2} \frac{a}{b} \sin \gamma$$
$$- \cos \gamma \left(\frac{\varkappa+1}{2} + \frac{c^2}{b^2} \sin^2 \Phi + \frac{|U_2|/|U_\infty|}{b^2 M_2^2} \right) - \frac{\varkappa+1}{2} \frac{c}{b} \tan \Phi = 0 \hat{=} \varepsilon$$

When Φ is specified, this equation is solved so that it satisfies $\varepsilon < 10^{-4}$. The corresponding Mach number component M_N can then be solved with equation (36).

112

The velocity vector the medium range in the aerodynamic coordinate system is given as follows in detail according to equation (45):

$$\frac{\vec{U_4}}{|U_\infty|} = \vec{i}\left[\cos\alpha\cos\gamma(A1+B1)+\cos\alpha\sin\gamma(g(M_{4e})\cos\varphi)\right.$$
$$\left.+\sin\alpha(g(M_{4e})\sin\varphi)\right]$$
$$+\vec{j}\left[\cos\gamma(g(M_{4e})\cos\varphi)-\sin\gamma(A1+B1)\right]$$
$$+\vec{k}\left[\sin\alpha\cos\gamma(A1+B1)+\sin\alpha\sin\gamma(g(M_{4e})\cos\varphi)-\cos\alpha\cos\varphi\right]$$

$$(45a)$$

A 1 and B 1 are given by

$$A1 = \cos\alpha\cos\gamma(a-b\tan\gamma)$$
$$B1 = \sin\alpha\cos\gamma(c-b\frac{\tan\Phi}{\cos\gamma})$$

APPENDIX V

In the case where the internal shock is to produce an additional component in the direction of the leading edge, then $\vec{U_3}\circ\vec{j}\neq 0 = -K.$. Then the velocity in the medium range is given by equation (45a), and in addition to A 1 and B 1 we have

$$C1 = (b-b\cdot K)\cos\gamma$$

Therefore, the sum (A 1 + B 1) in equation (45a) is the expanded into (A 1 + B 1 -C 1).

TABLE 1a: THEORETICAL HANDLING OF LEE SIDE FLOW.

VK type (leading edge)	Flow model	Initial equation	Solution method	Remarks	Author
SUBSONIC LEADING EDGE		Momentum theorem	Treatment of the problem in planes perpendicular to the incident flow (theory of slender bodies)	No leading edge separation	Jones [23]
		Theory of slender bodies	Fixation of vortex, with stream surfaces to the leading edge	No unique solution, no force equilibrium	Edwards [26]
		theory of slender bodies	Conformal mapping. RB: Force equilibrium for the entire system.		Brown and Michael [27]
		Theory of slender bodies	Division of the vortex – spiral-shaped part – Nucleus	Good prediction of vortex position	Mangler and Smith [28]
		Theory of slender bodies	Conformal mapping	Secondary vortex simulation by stagnation point S	Pershing [32]
		Linear theory	Analytical	Mach number influence	Squire [34]
		Theory of slender bodies	Source and vortex - distribution according to the contour. Division into a longitudinal flow and transverse flow problem.	Leading edge separation not considered	Hummel [37]
		Theory of slender bodies	Leading edge suction analogy	Mach number influence	Polhamus [35]

114

TABLE 1b: THEORETICAL TREATMENT OF LEE SIDE FLOW

VK (leading edge) / Flow model	Initial equation	Solution method	Remarks	Author
	① P.M.-Expansion ② Hyperbolic D.E. ③ Elliptical D.E.	— Characteristics Relaxation	Flow without shocks	Maslen [50]
	① P.M.-Expansion ② Shock relationships ③ Hyperbolic D.E. ④ Elliptical D.E.	— — Characteristics Relaxation	Solution without shocks and shock solution depending on angle of attack	Fowell [52]
	① P.M.-Expansion ② Uniform flow ③ Shock relationships ④ Continuity equation	— — Iteration as RD to 4 Difference methods	Shockless solution impossible shock perpendicular to surface	Babayev [53]
	① P.M.-Expansion ② Uniform flow ③ ④ Hyperbolic D.E.	— — 3-dimensional characteristics	Shock is isentropic compression in spite of this difficulties for sample calculations shockless	Beeman and Powers [55]
	Continuity equation, Momentum theorem, Energy equation	Difference method with shock front	Weak shock solution	Kutler and Lomax [56]
	① P.M.-Expansion ② Uniform flow ③ Euler equations	— — Characteristics rotational	Range of validity of elliptical D.E.: for rotational with rotation is not determined	Christophel [59]
	① P.M.-Expansion ② boundary layer ③ shock relationships ④ uniform flow	— — — —	Input of empirical values about: -- boundary layer -- shock front parameters	Cross [49]

ÜBERSCHALLVORDERKANTE

.... Parabolic line   ——— Expansion   --- Reflected expansion waves   ——— Mach cone   === Shock

115

TABLE 2: SUMMARY OF MOST IMPORTANT EXPERIMENTS ON LEE SIDE FLOW

Column groups: Model values (Sweep angle $\Lambda[°]$, Relative height h/l, Top side shape: Flat / Delta / Cone) — Test values (Reynolds No. Re_∞ [1/m], L.E. type UVK, Mach number M_∞, Shock type: Attached / Separated, Incidence angle $\alpha[°]$) — Measured value (Pitot stat., Pressure, Temp.)

References	Re_∞ [1/m]
Gapcinski [21]	1.1×10^7
Lee [22]	1.5×10^5
Fellows + Carter [18]	Subsonic L.E.
Greenwood [19]	4×10^5
Edwards [88]	6×10^6
Dieugge + Larson [14]	–
Thomann [15]	2×10^6
Monnerie + Werle [75]	4×10^5
Bannik + Nebbelink [38]	5×10^7
Squire [41–42]	1.1×10^7
Rao + Whitehead [5]	8×10^6
Collis [48]	3.3×10^6
Fowell [52]	
Cross [49]	3×10^6
Helner [8,43]	2.3×10^7
Whitehead + Rao [6]	2×10^7
Miyazawa [58]	6×10^7
Morris + Couch [20]	1×10^7
Rein [46]	9×10^5
Alexander + Craven [72]	4.5×10^6
Lawrence + Holdstock [80]	7×10^6
Richards [78]	9×10^6
This report	7×10^6

Subsonic leading edge   Supersonic leading edge

a) attached flow   b) Leading edge separation   c) attached flow   d) shock-induced separation
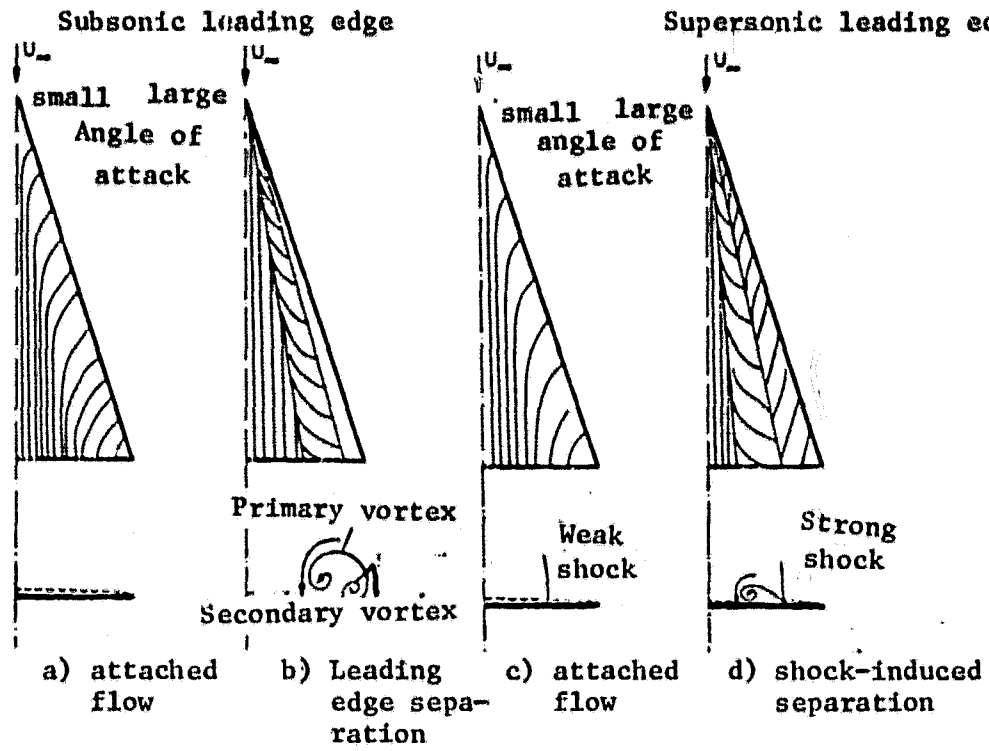
Fig. 1. Flow models on the lee side of slender delta wings.

Mach number perpendicular to leading edge M_N
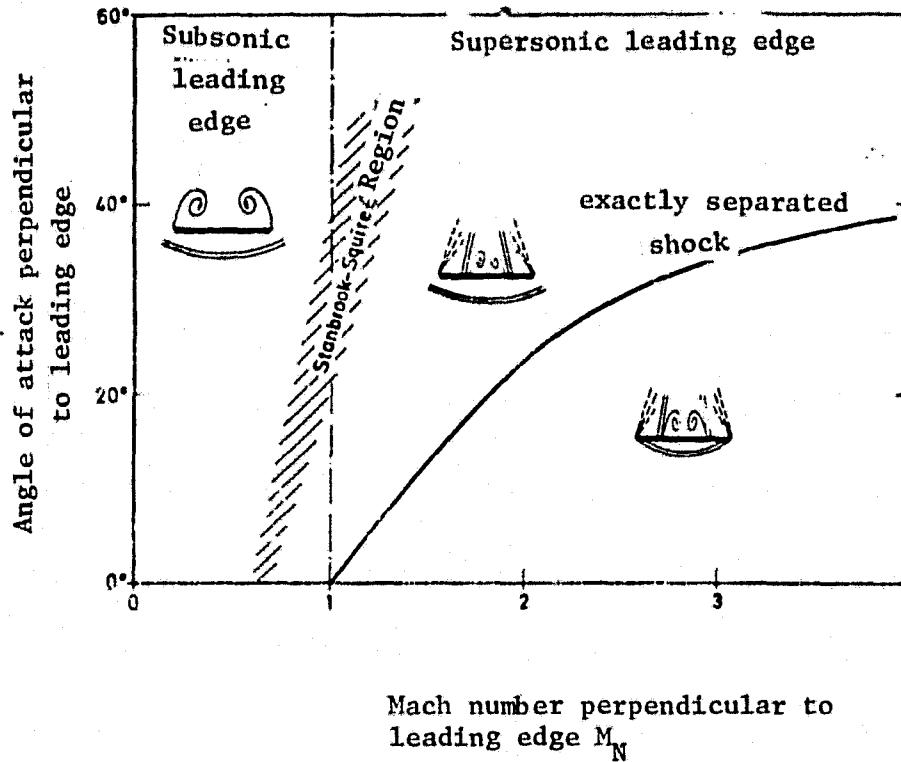
Fig. 2. Flow regions over the thin flat delta wing.
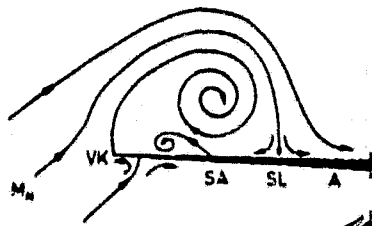
Section perpendicular to leading edge (VK

A - attached flow
SL- separation line
SA- secondary separation
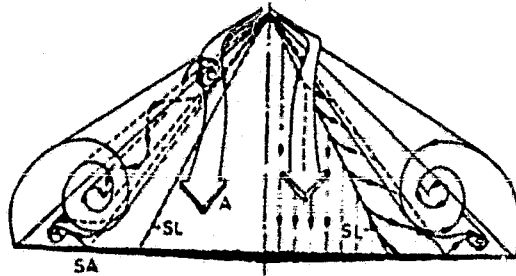
Vortex formation and

stream line course
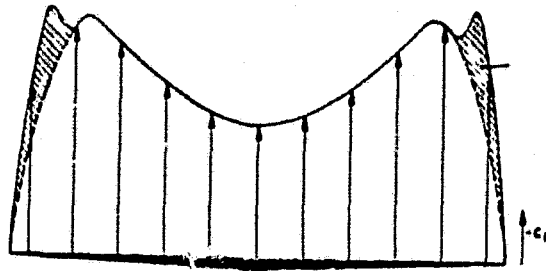
Pressure distribution
Pressure part of secondary vortex

Fig. 3.   Lee side flow over slender delta wing with subsonic
          leading edge.

Section perpendicular to leading edge (VK
A - attached flow
SL - separation line
SA - secondary separation
VS - leading edge shock

Vortex formation and
stream line course

Pressure distribution
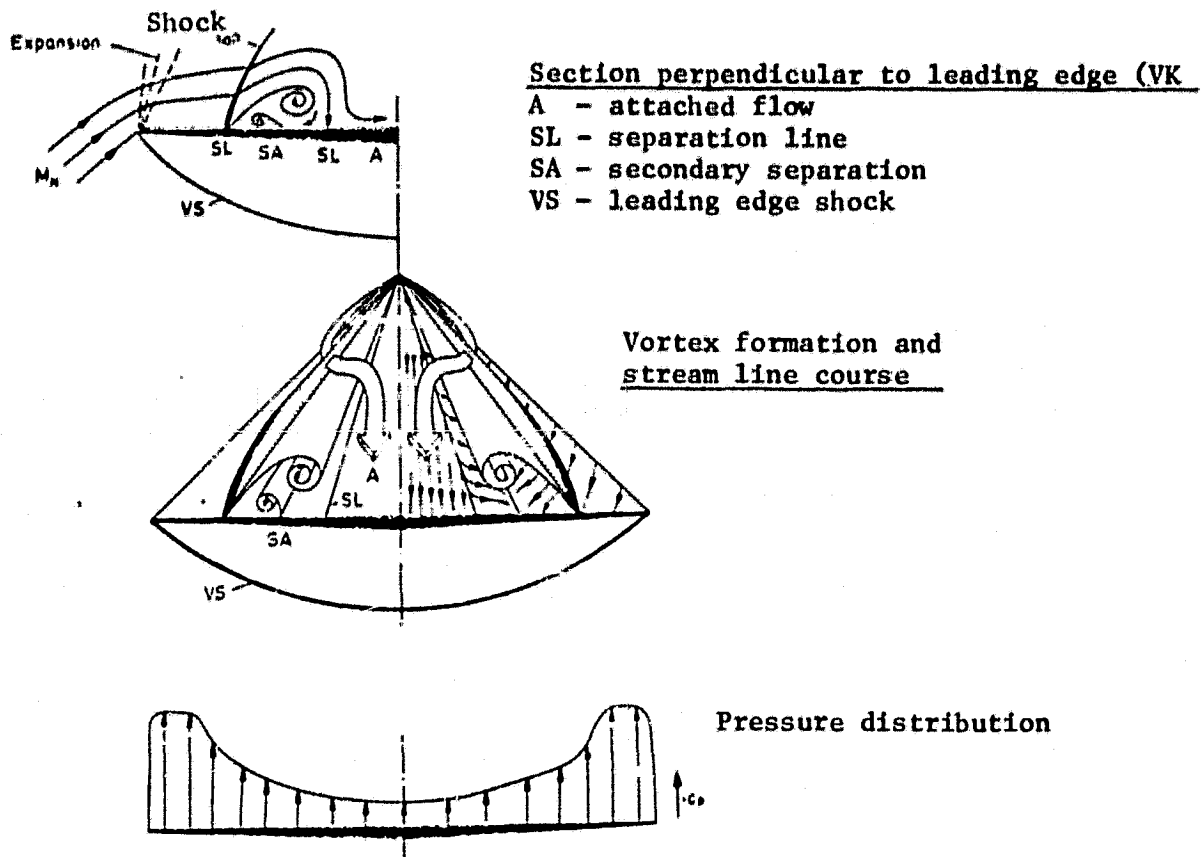
Fig. 4.   Lee side flow over slender delta wing with supersonic
          leading edge.
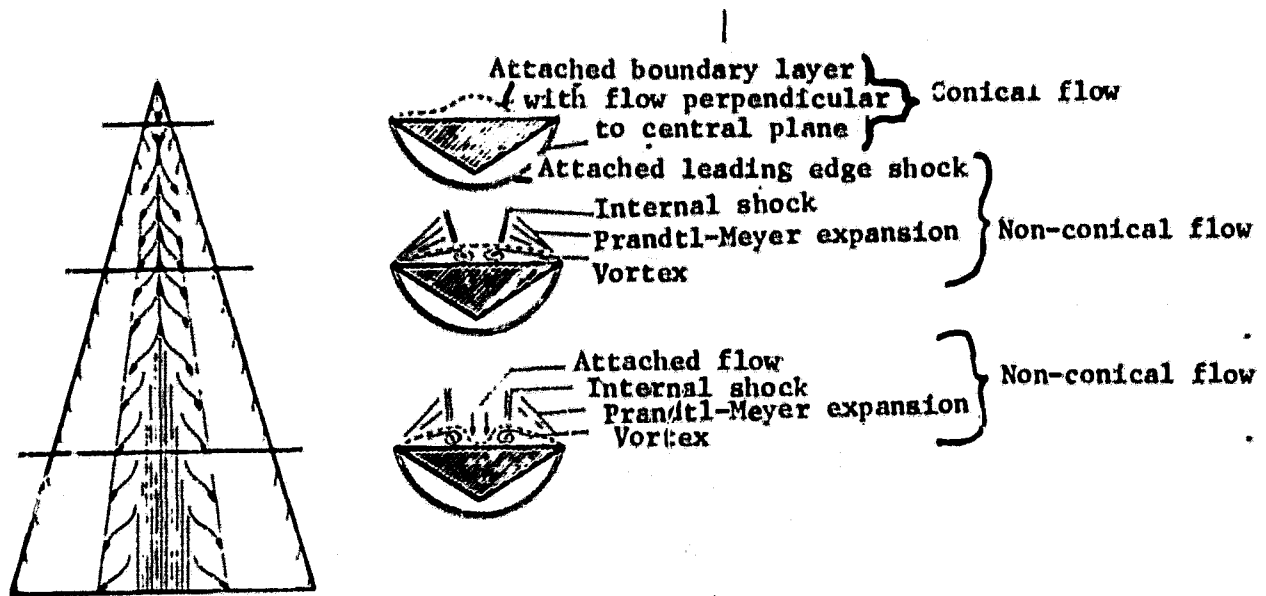
Fig. 5. The hypersonic flow model of Whitehead/Heftner/Rao [6].
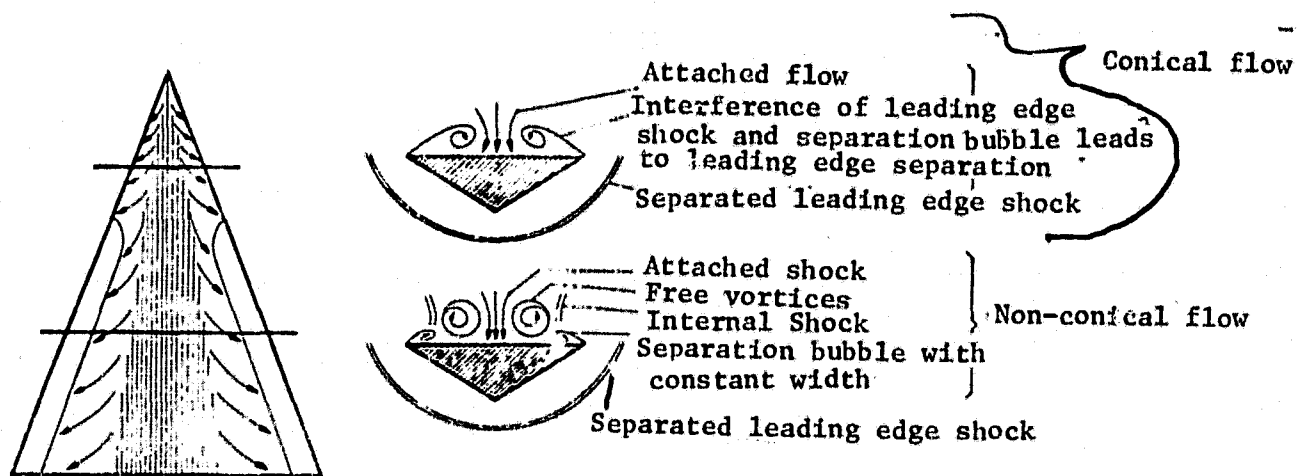
Fig. 6. The supersonic flow model of Rein [46] for separated
leading edge shock.
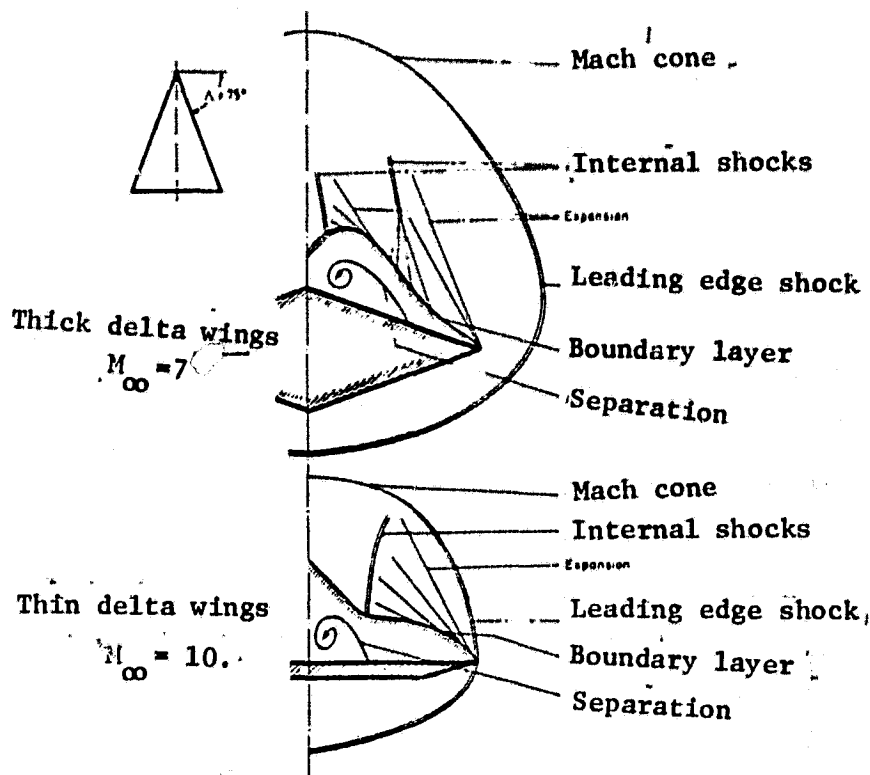
Fig. 7. Flow models for delta wings in the hypersonic regions for medium angles of attack.
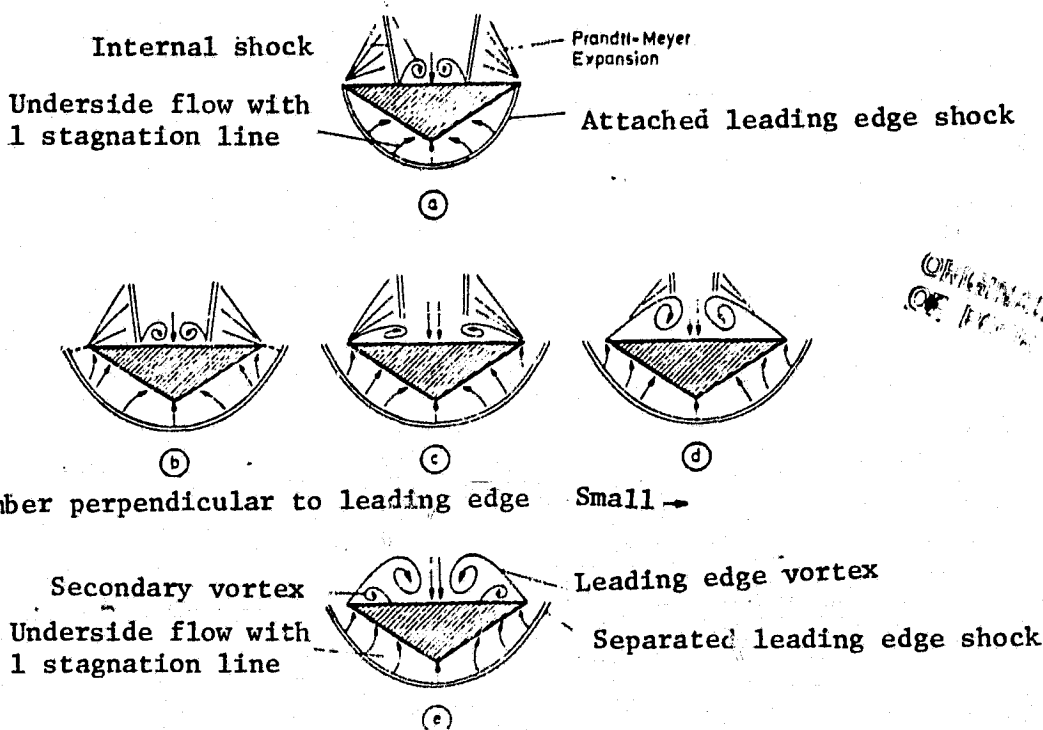
Fig. 8. The transition from shock-induced separation to leading edge vortex formation.
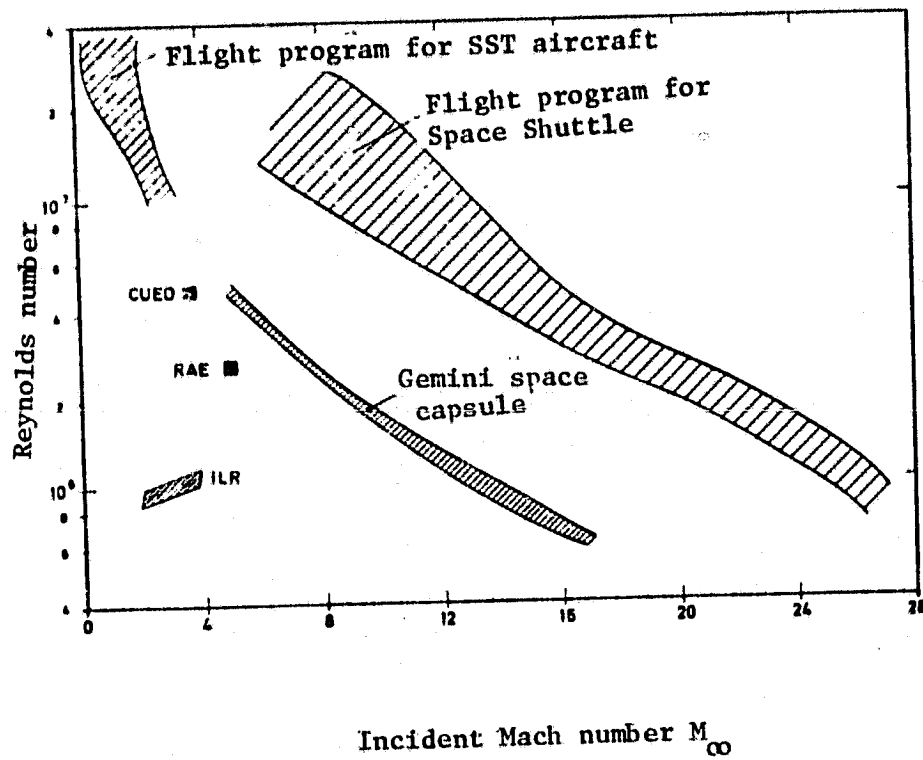
Fig. 9. Real flight ranges compared to wind tunnel tests.

Slenderness $s/1 = 0.31$

1 Convex delta model with
  leading edge angle $\psi = 55^o$
2 Flat delta model with
  leading edge angle $\psi = 40^o$
3 Flat cone model with
  leading edge angle $\psi = 75^o$

Cross-section shapes

Model 1
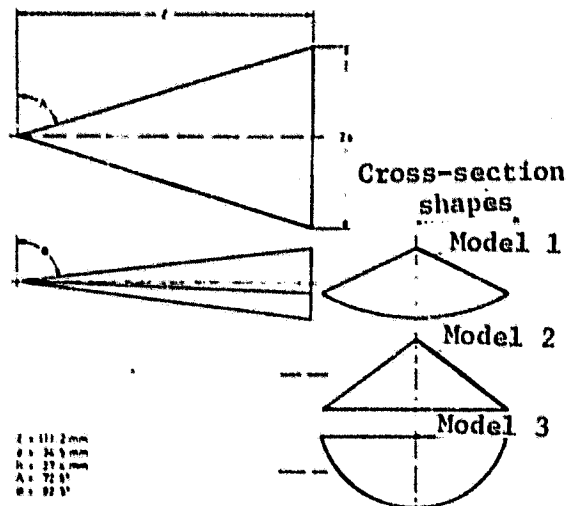
Model 2

Model 3

Fig. 10. Wind tunnel Model I
          (CUED, RAE)

Slenderness $s/1 = 0.30$

4 Flat delta model with
  leading edge angle $\psi = 38.9^o$
5 Flat cone model with
  leading edge angle $\psi = 75^o$
6 Nonweiler wave rider with
  leading edge angle $\psi = 39.5^o$
  (initial parameter $M_o = 2$)

Cross-section shapes

Model 1
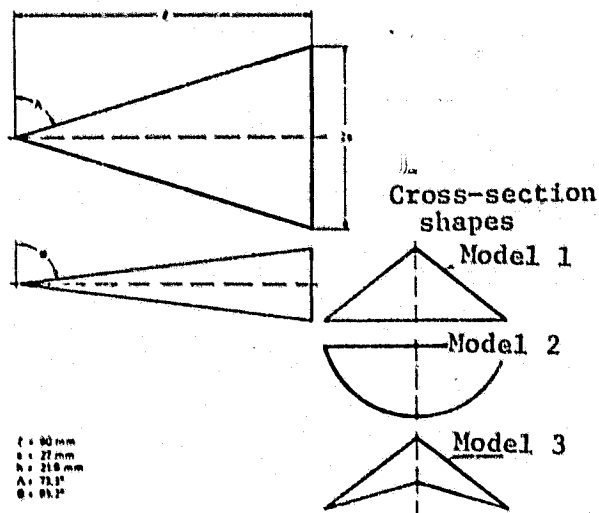
Model 2

Model 3

Fig. 11. Wind tunnel Model II
          (ILR)

123

Slenderness s/1 = 0.3
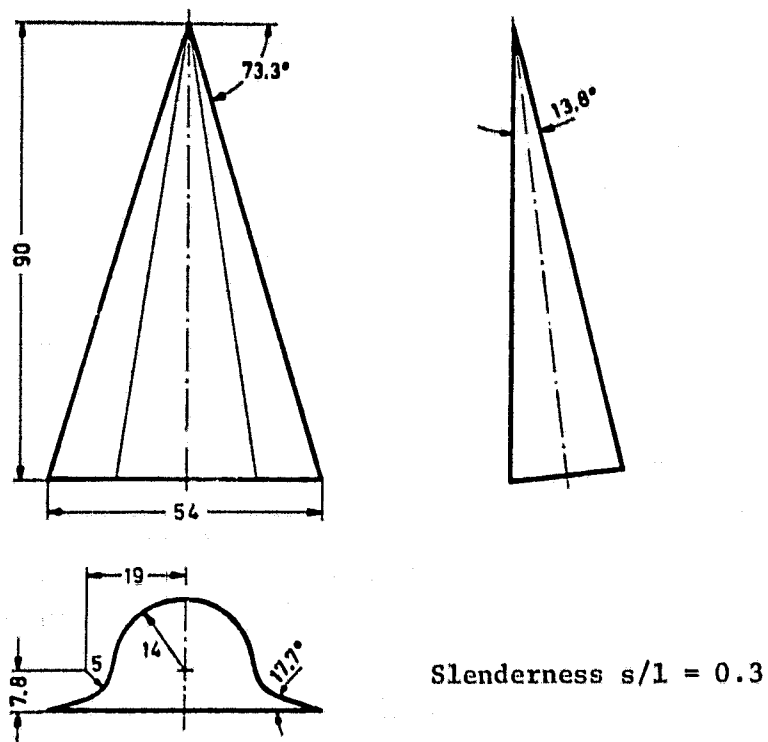
Fig. 12.   Modified cone model (ILR)

Cambridge wind
tunnel

Section A-A

RAE wind
tunnel

Section A-A

ILR wind
tunnel
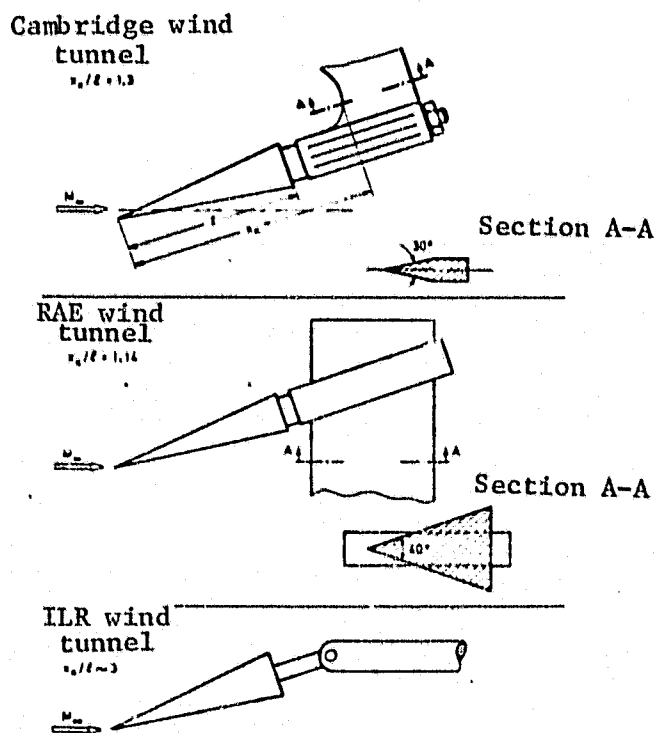
Fig. 13.   Model suspension in
various wind tunnels
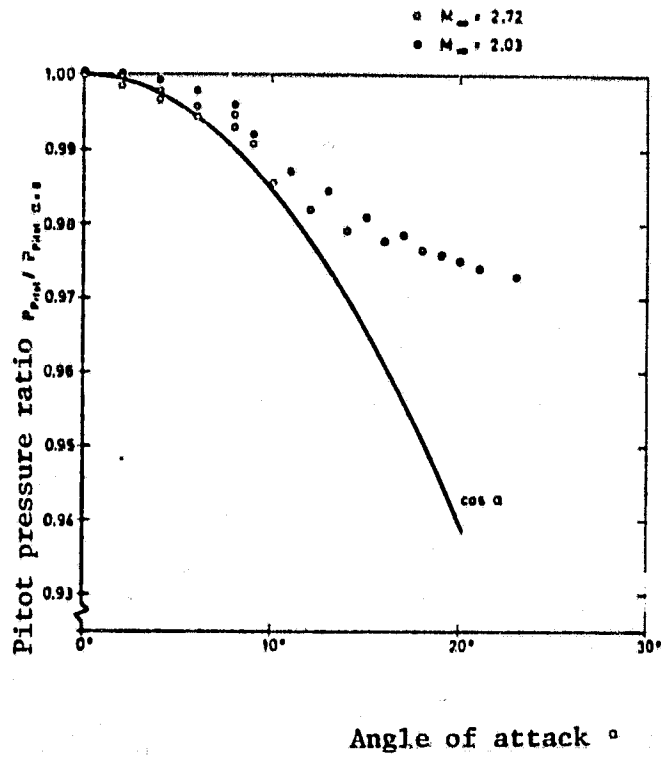
Fig. 14. Pitot probes, cali-
bration as a function
of incident flow angle.

Flow field in the
Tranverse plane
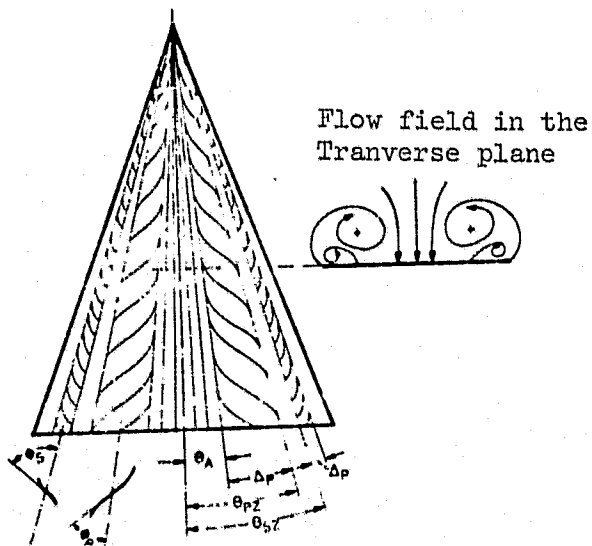
θ_A = position of attachd flow
θ_{PZ} = primary vortex center
θ_{SZ} = secondary vortex center
$\bullet_P$ = primary vortex intensity
$\bullet_S$ = secondary vortex intensity
Δ_P = primary vortex parameter
Δ_S = secondary vortex parameter

Fig. 15. Definition of oil film
image evaluations
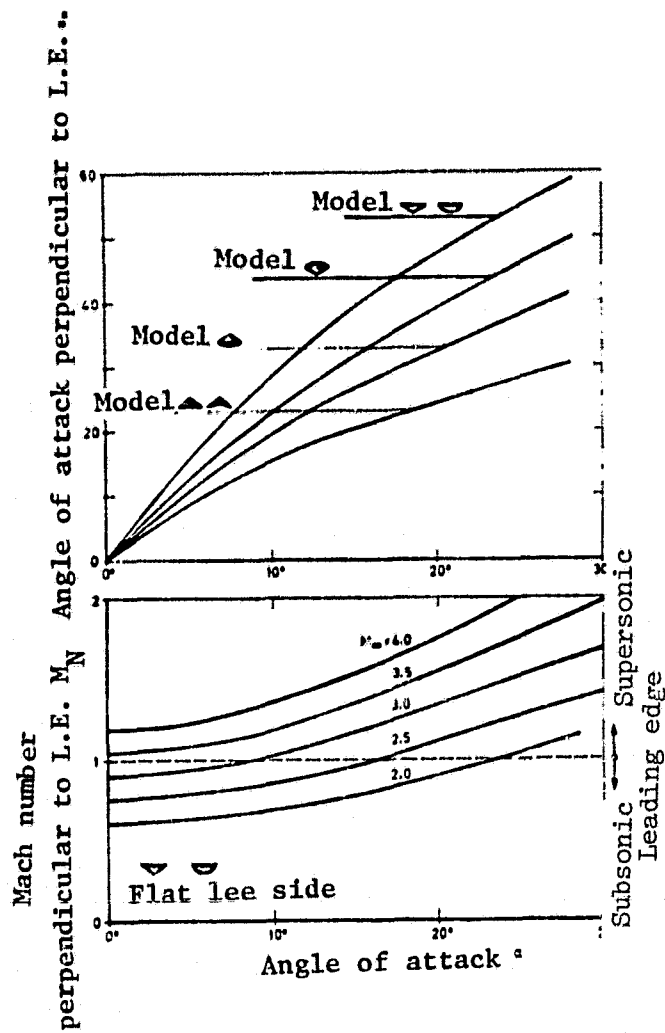
Fig. 16. Angle of attack and Mach number perpendicular to leading edge for delta wings with different cross-section shapes.
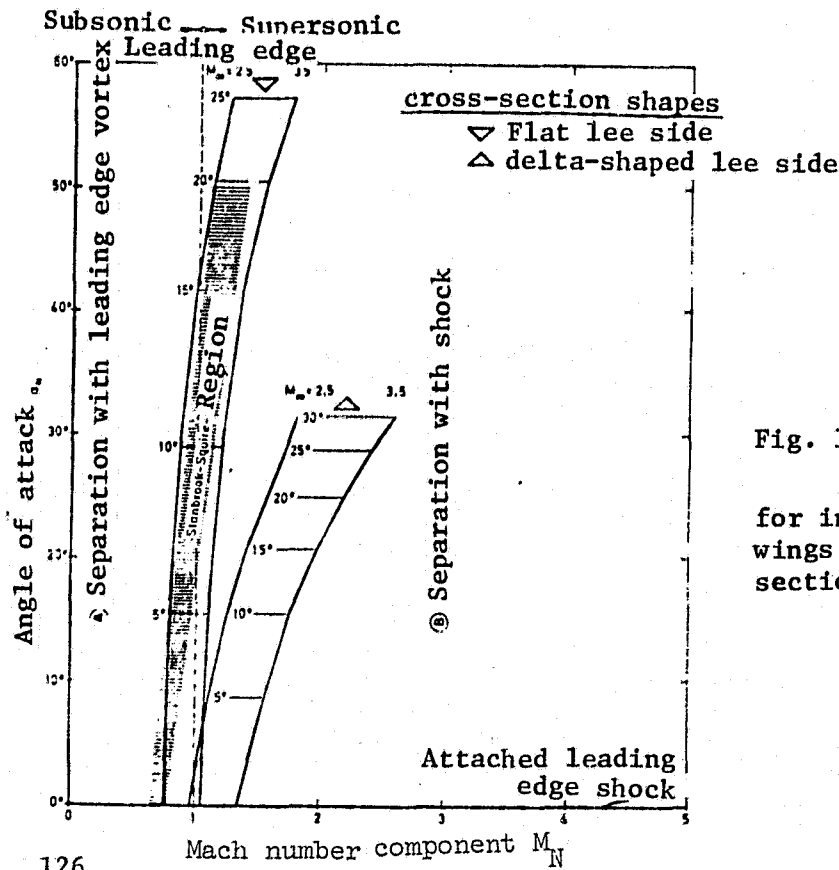
Fig. 17. α_N, M_N diagram

for investigations of delta wings with different cross-section shapes.

126

Fig. 18. Isobars on delta-
shaped lee side of
the Model I,

$M_\infty = 3.5$

Secondary vortex

Oil film Primary vortex
Attached flow

Schlieren

Schlieren

Pitot isobars

Pressure distribution

A – attachment line
PZ – primary vortex center
SZ – secondary vortex center
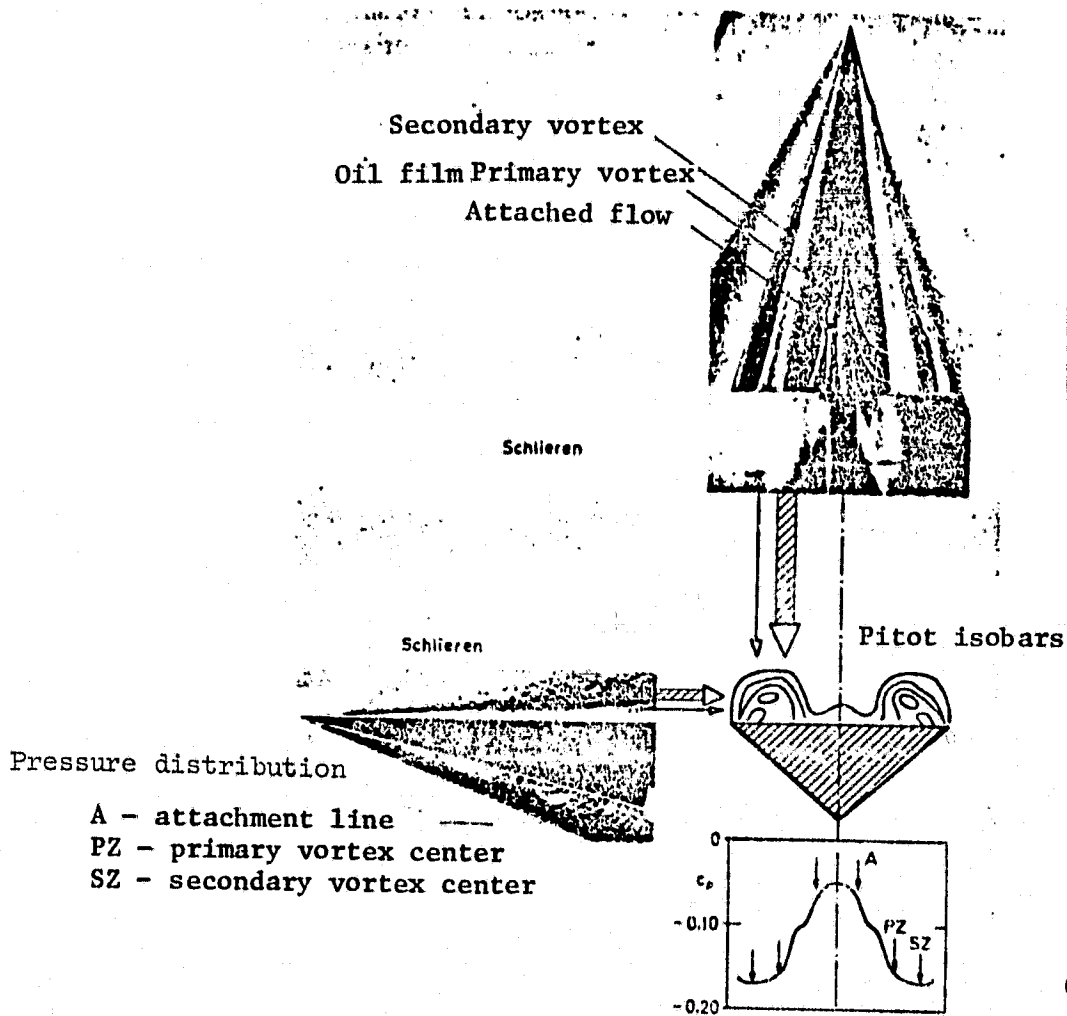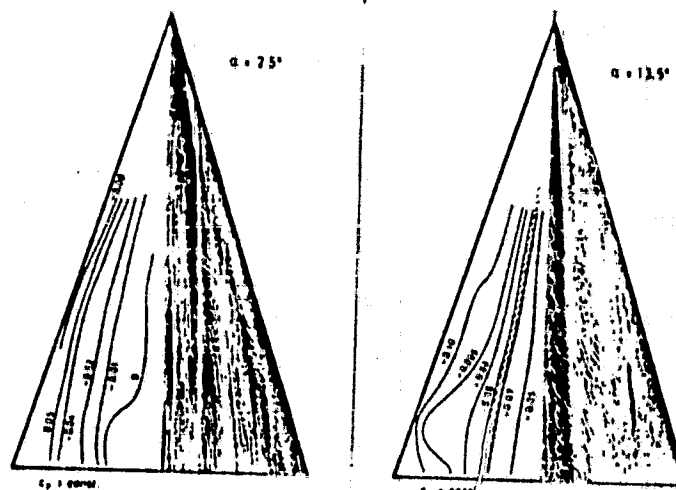
Fig. 19. Flow field analysis over the flat lee side of the delta
wing at $\alpha = 10^\circ$, $M_\infty = 2.5$
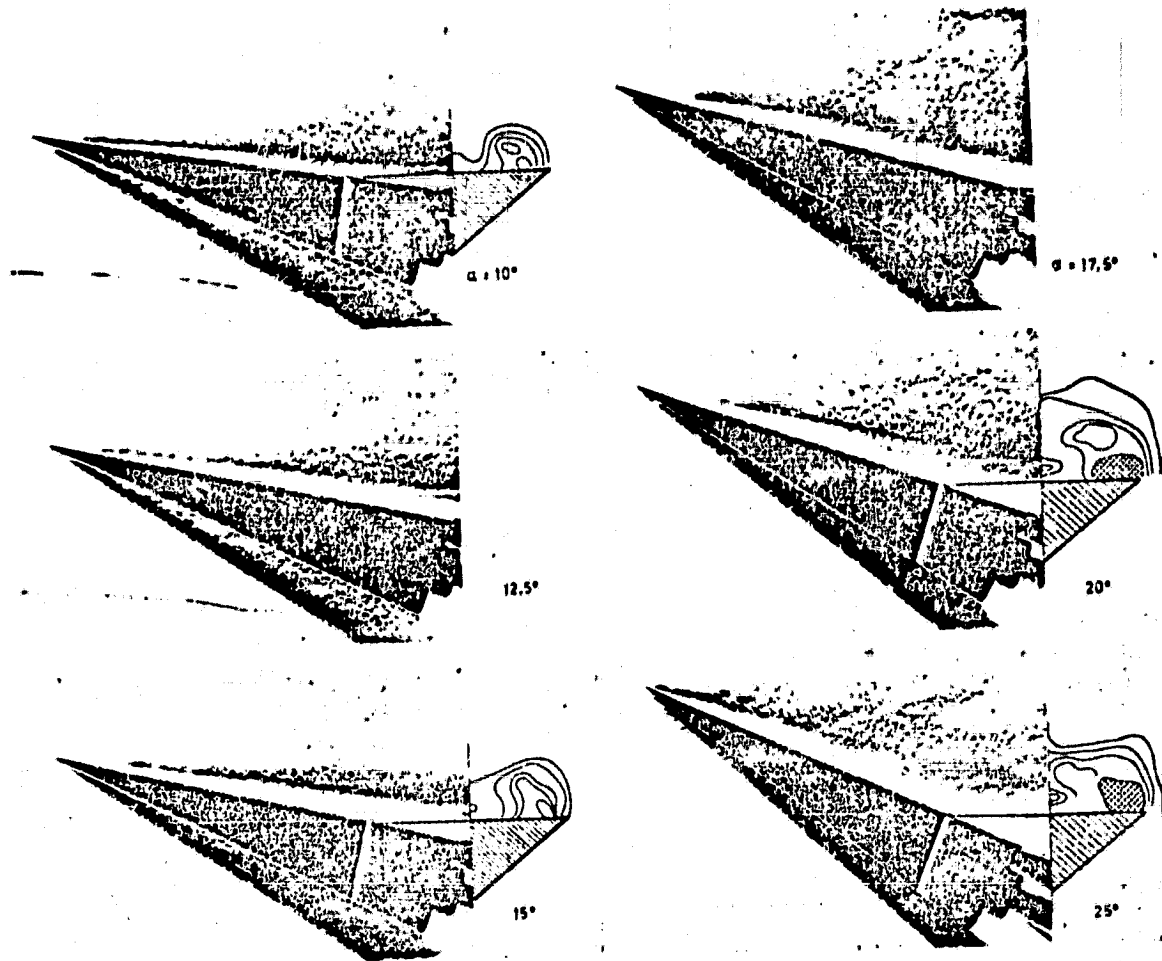
Fig. 20a and b. Schlieren photographs for flat lee side of
delta wing for different angles of attack
M_∞ = 2.5.
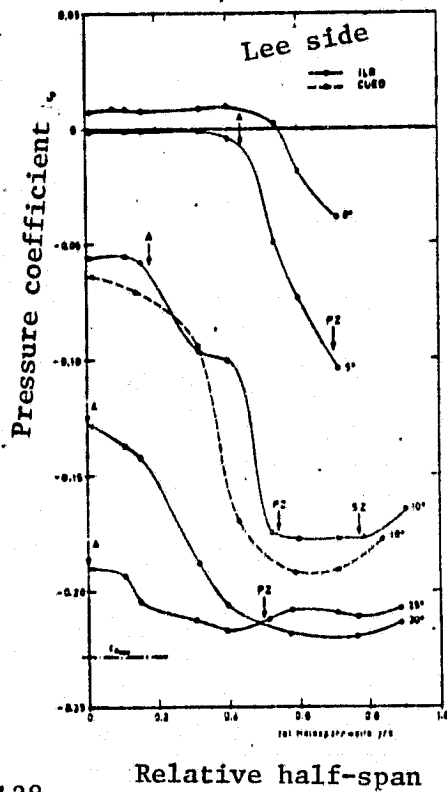
Fig. 21. Pressure coefficients over span
for different angles of attack
M_∞ = 2.5.
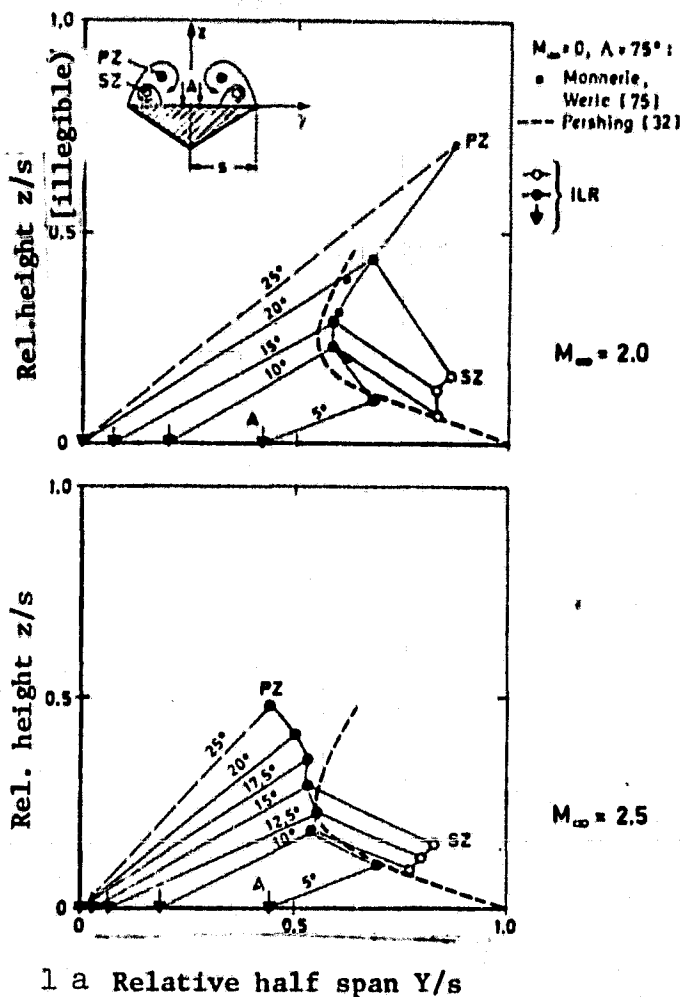
Fig. 22. Position of primary (PZ) and secondary (SZ) vortex over the delta wing.

1 a Relative half span Y/s
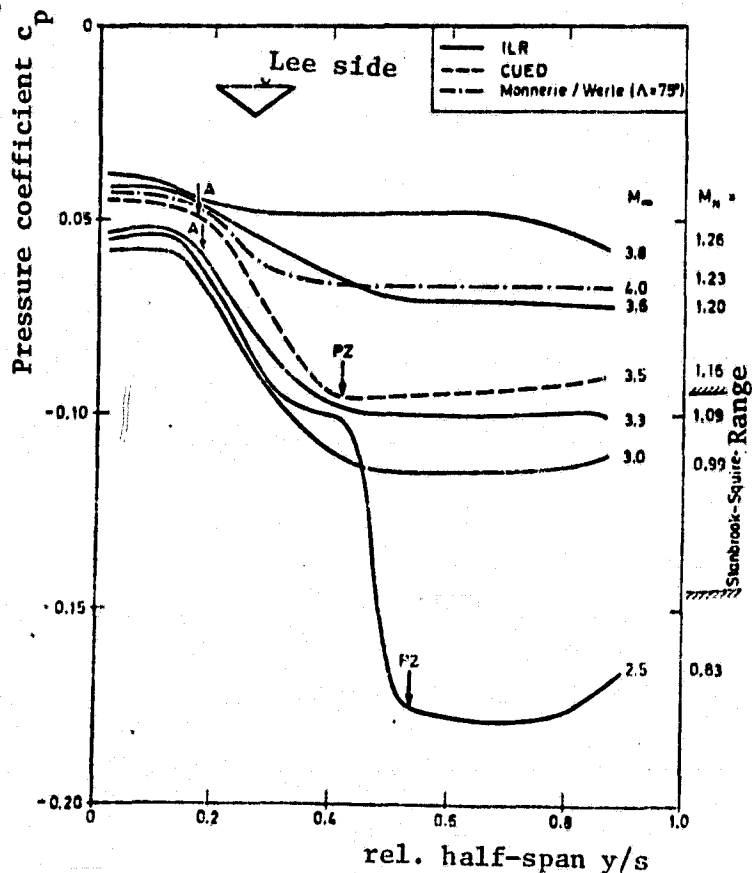
Fig. 23. Pressure coefficients over span for different Mach numbers,

$$\alpha = 10°$$
$$(\alpha_N = 20°)$$

Normal Mach No. M_N
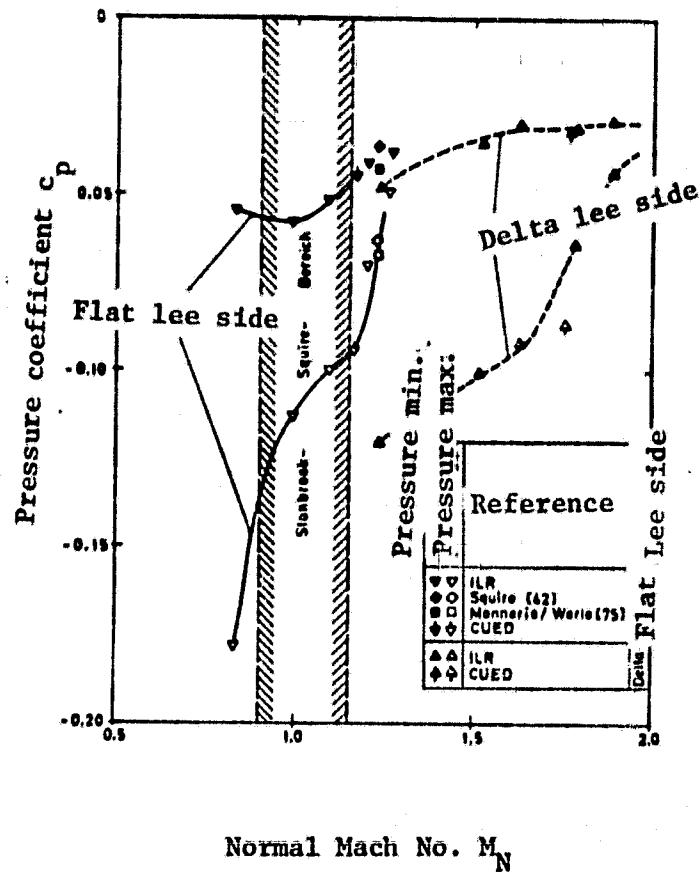
Fig. 24. Changes of minimum and maximum pressure on lee side of delta wings
as a function of Mach number, $\alpha = 10°$
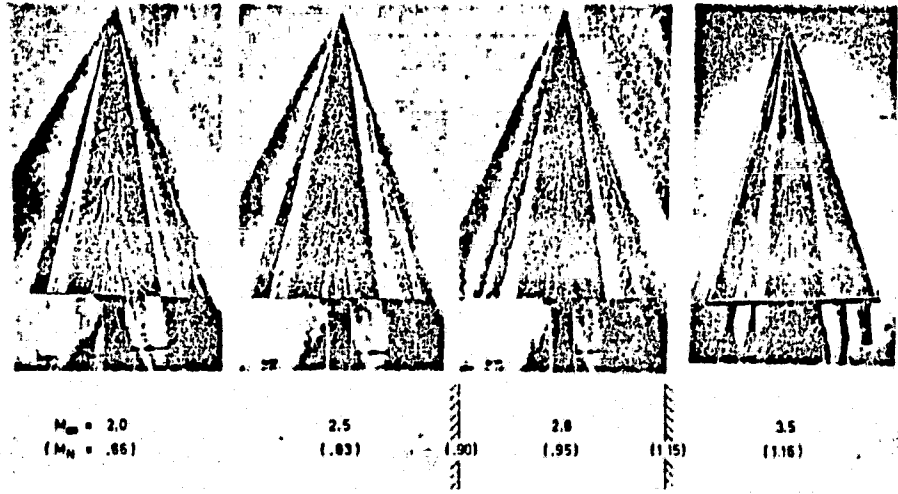
Fig. 25. Oil film and Schlieren photographs with the flat lee side for
different Mach numbers, $\alpha = 10°$

130
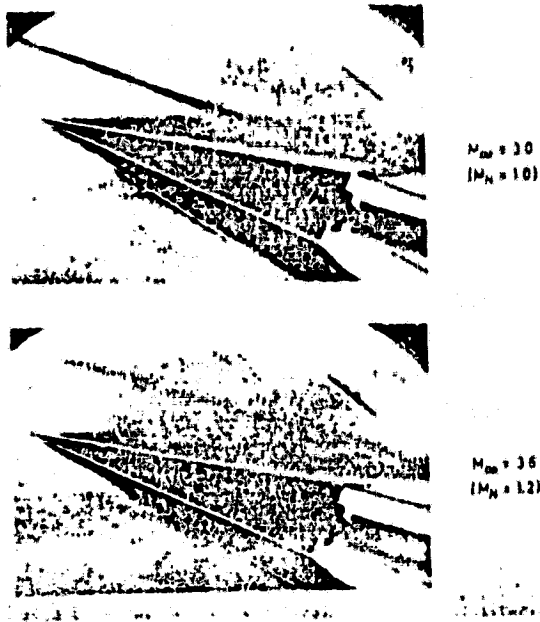
Fig. 26. Vortex formation over flat lee side for different Mach numbers

$$\alpha = 10° \; (\alpha_N = 29°)$$
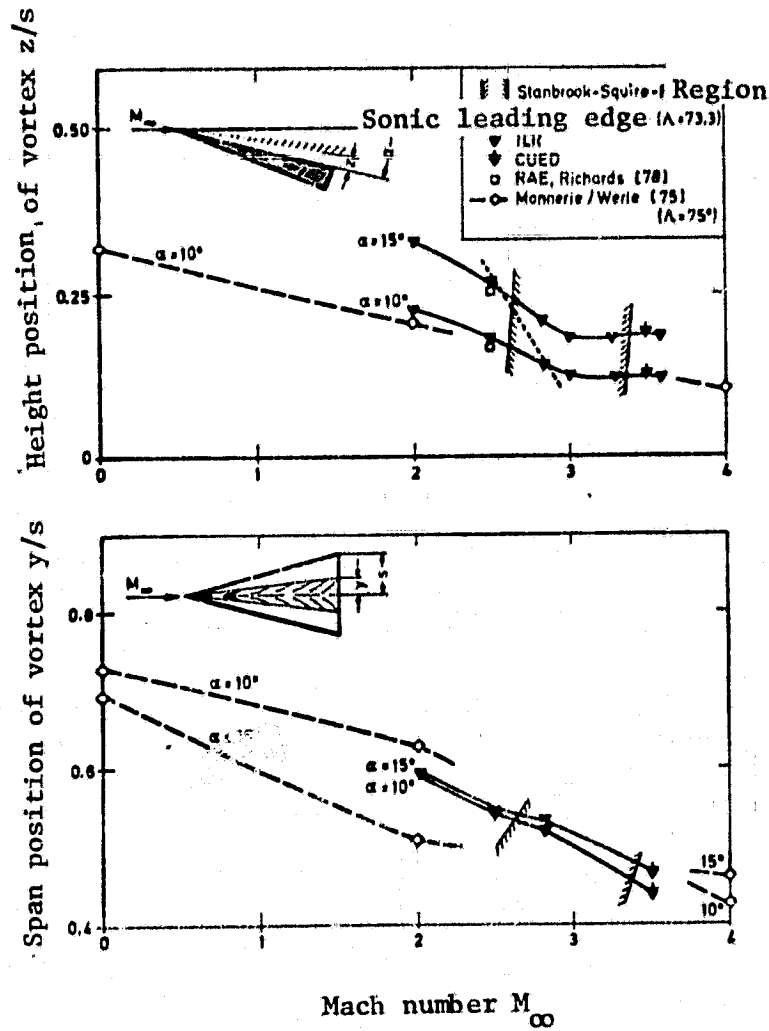
Fig. 27. Vortex positions when crossing the Stanbrook-Squire region

Oil film   Dead water region
Vortex region
Attached flow.

Schlieren

**Fig. 28. Flow field analy-
sis over flat lee
side of the delta
wing at**

$$\alpha = 10^{\circ} \text{ , } M_{\infty} = 3.5$$

Pitot isobars

Pressure distribution

(A – attachment line
(W – vortex separation line)

c_p

Vacuum

Ölfilm

Internal shock

Expansion

Pitot pressure ratio 1 $p_r/p_{r_{\infty}}$

Attached flow

rel. height z/s

Separation bubble

rel. span y/s
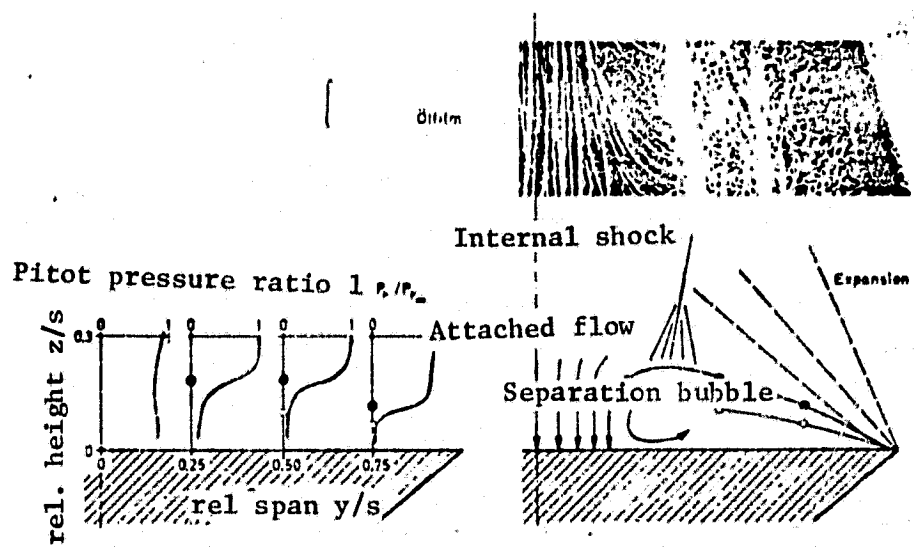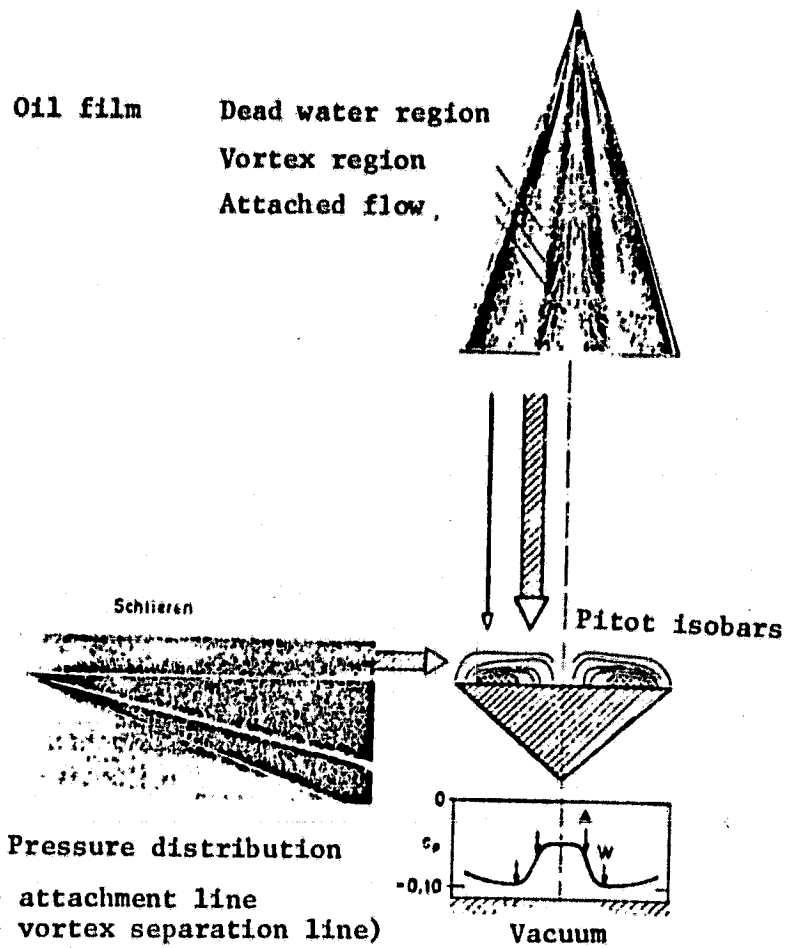
Fig. 29. Experimentally determined flow model, $M_{\infty} = 3.5$ $\alpha = 10^{\circ}$

132
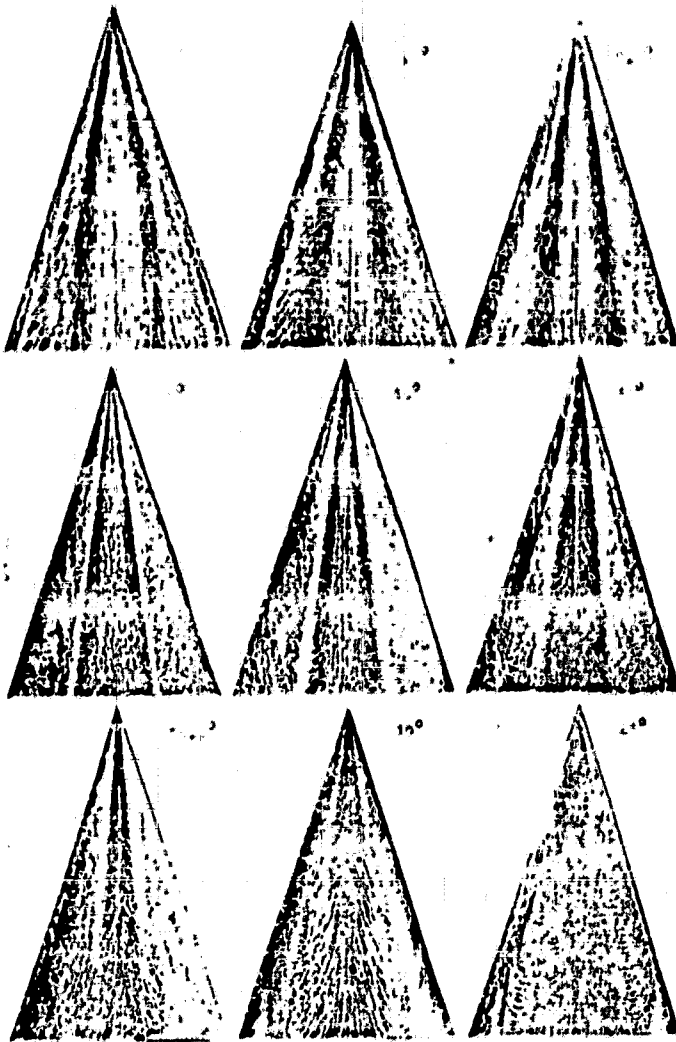
Fig. 30. Oil film photographs
on the flat lee side
of the delta wing
for different angles
of attack, $M_\infty = 3.5$.
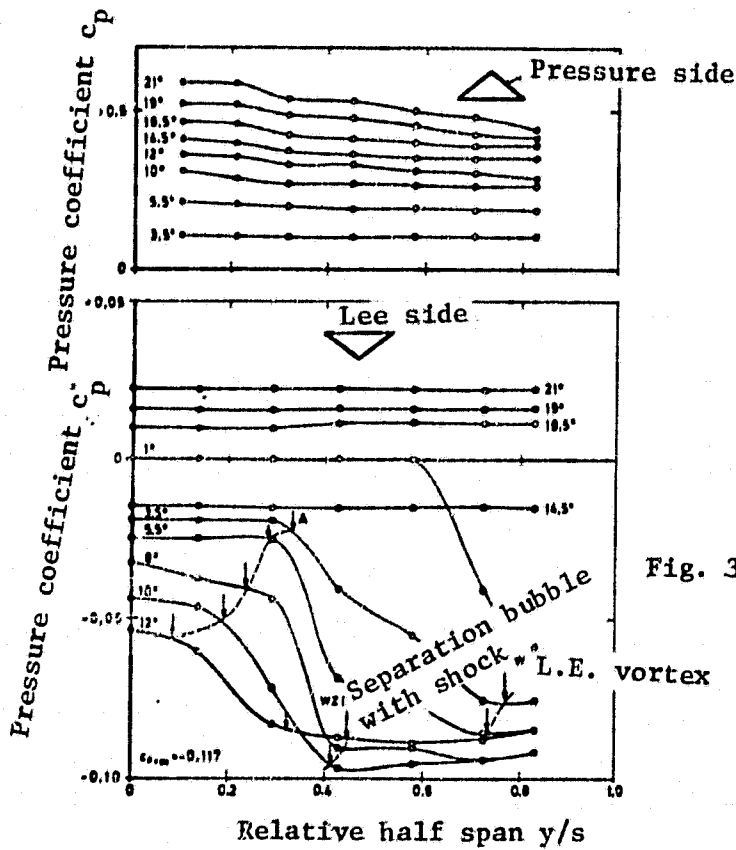
Fig. 31. Pressure coefficients over
span for different angles
of attack, $M_\infty = 3.5$.

Relative half span y/s

133
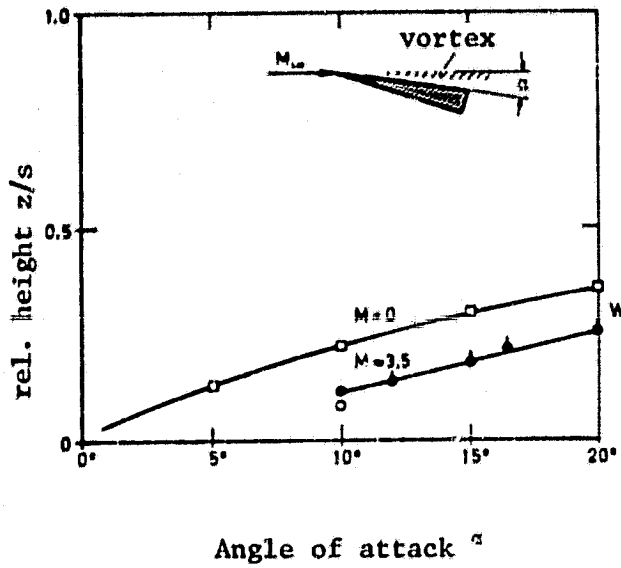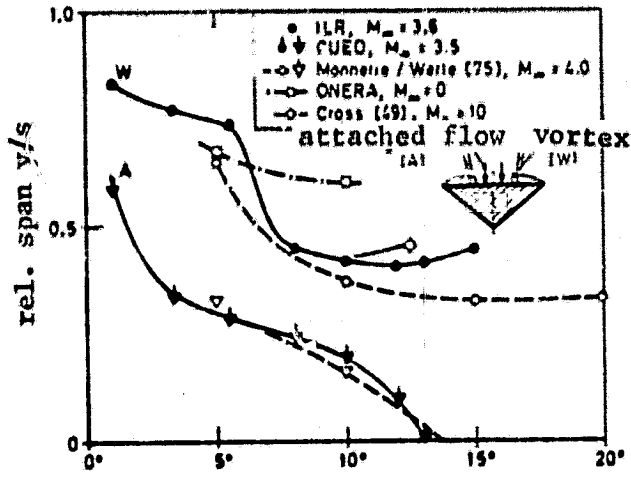
Fig. 32. Vortex position for different angles of attack
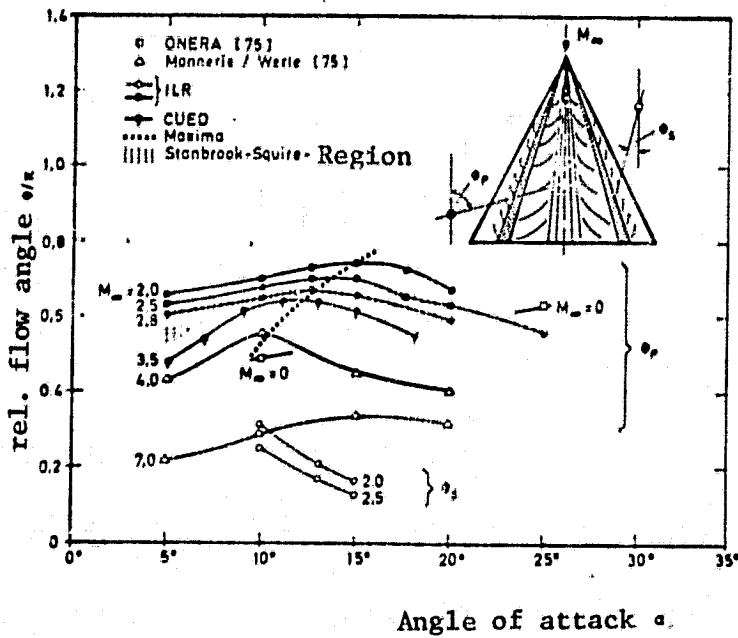
Fig. 33. Vortex intensity represented by delta flow angle in the oil film photograph for different Mach numbers

Legend:

▨ Stanbrook–Squire limit

▫ Expansion for small α

-·- Expension for large α

--- Squire [41-42] for thick wing $= 30°$

——— Symmetry plane shock

-··- Transition: separation with shock to separation induced by shock

,, Strong, weak shock

˝ Expansion

⸰⸰ Vortices, weak circulation
Attached flow

Attached shock $(\psi = 39.5°)$
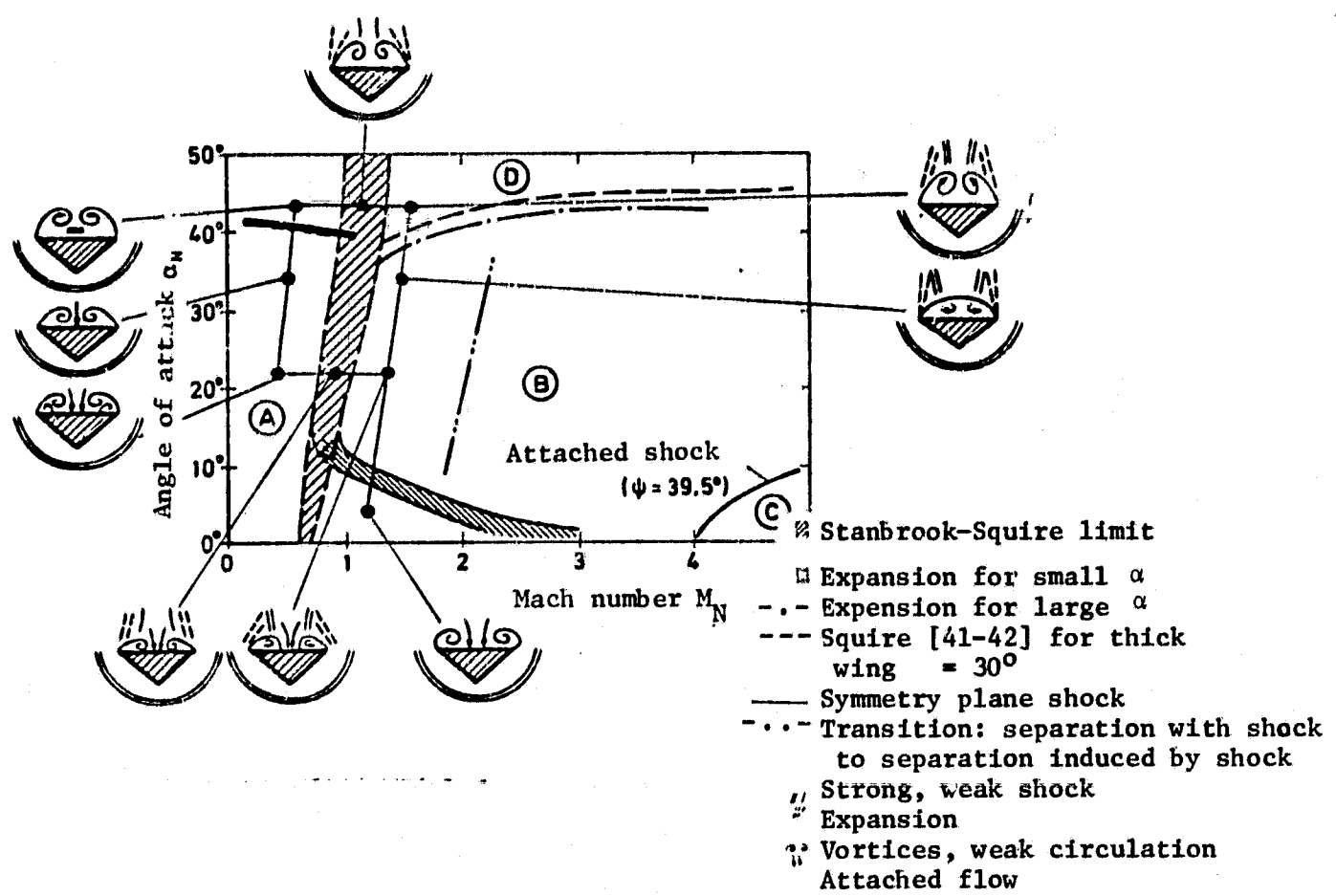
Fig. 34. Regions and models of the flow over the flat lee side of thick delta wings.

Pressure distribution

Oil film and Schlieren

Pitot isobars

Flow model
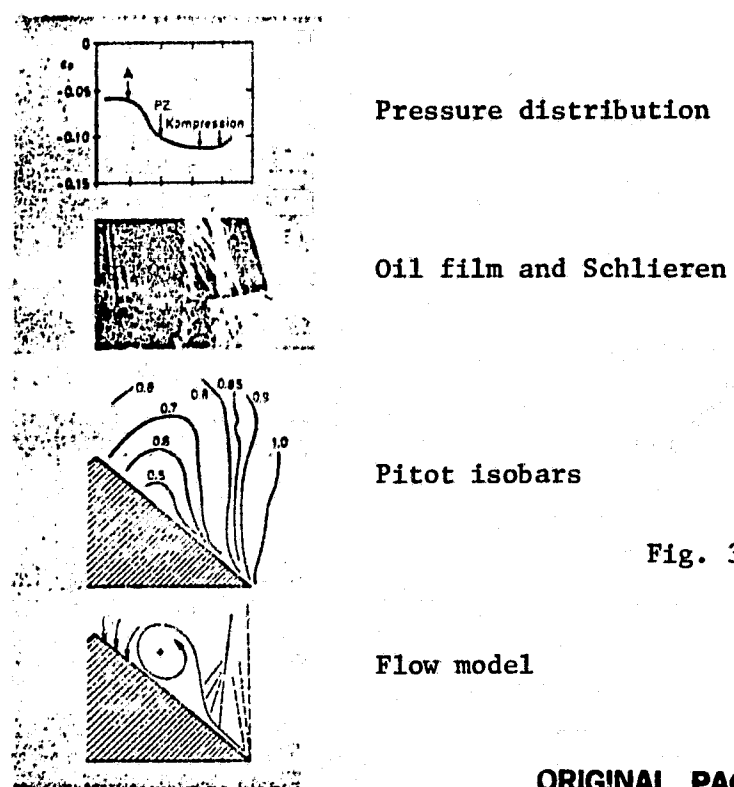
Fig. 35. Collection of experiments on the delta-shaped lee side
$M_\infty = 2.5, \alpha = 10°$
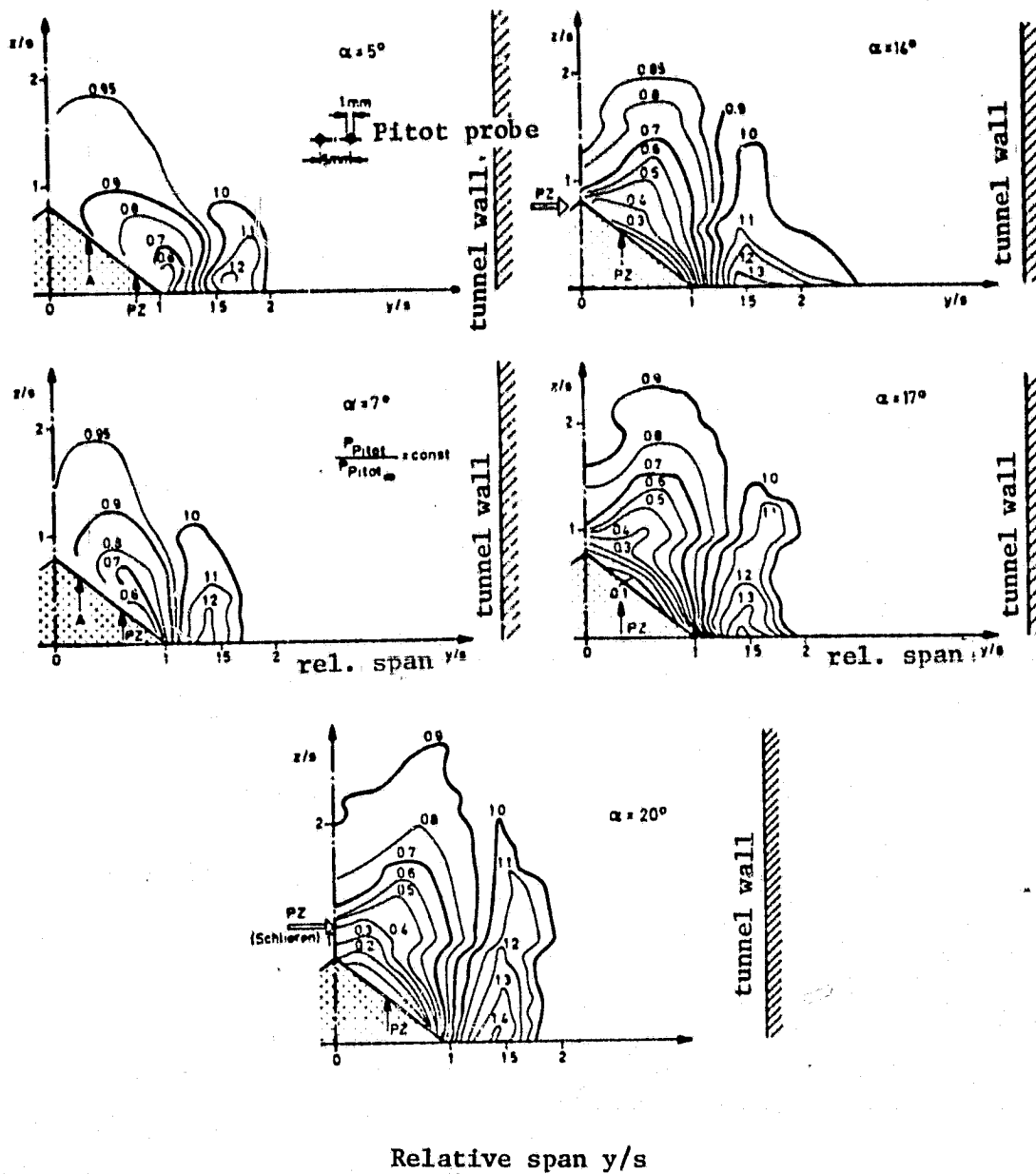
Fig. 36.   Pitot isobars on the top side of a delta wing for different angles
of attack.   Measurement plane $x/l = 0.8$, $M_\infty = 2.6$ ($M_N = 1.39$)
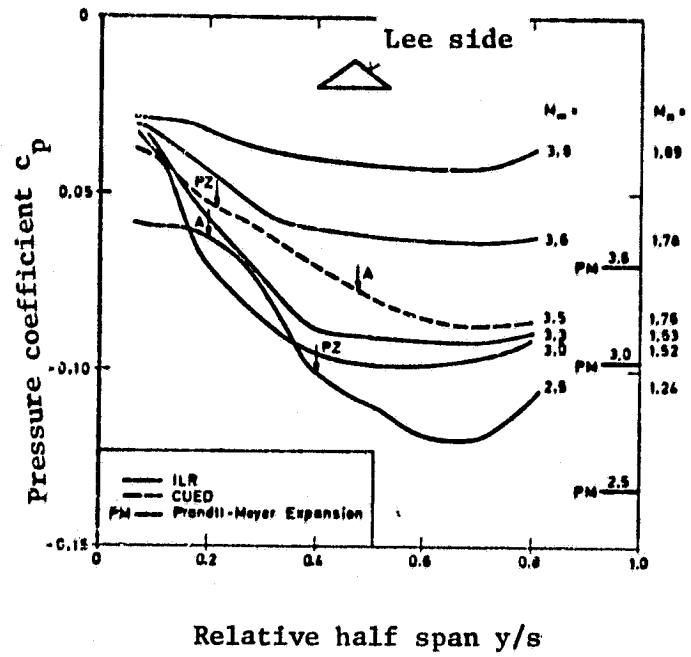
Fig. 37. Pressure coefficients over span for different Mach numbers
$\alpha = 10^{\circ}$ ($\alpha_N = 17^{\circ}$)
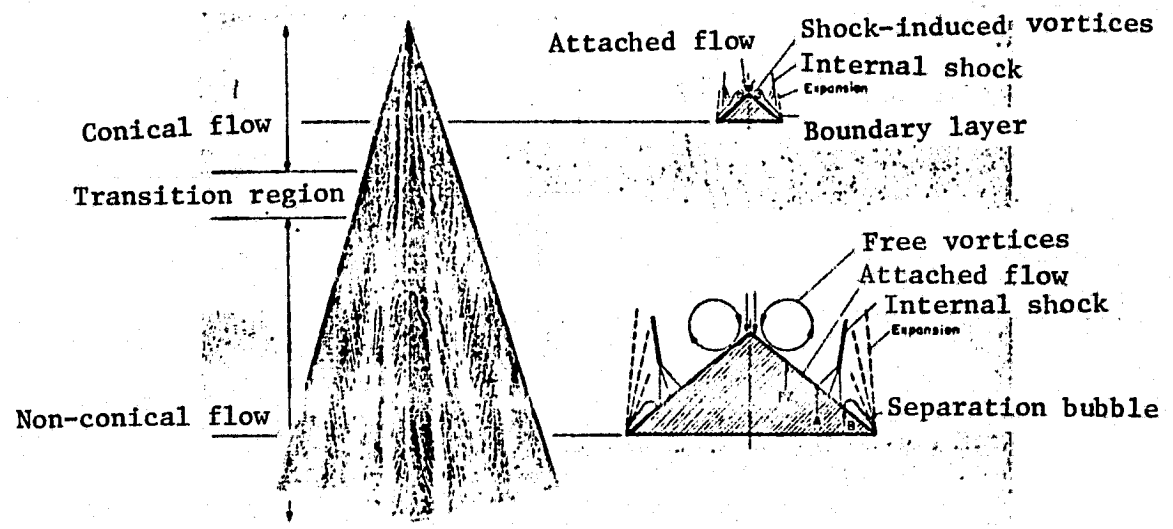
Fig. 38. Model of the flow over the delta-shaped lee side for the example
of $M_{\infty} = 3.5$ and $\alpha = 10^{\circ}$
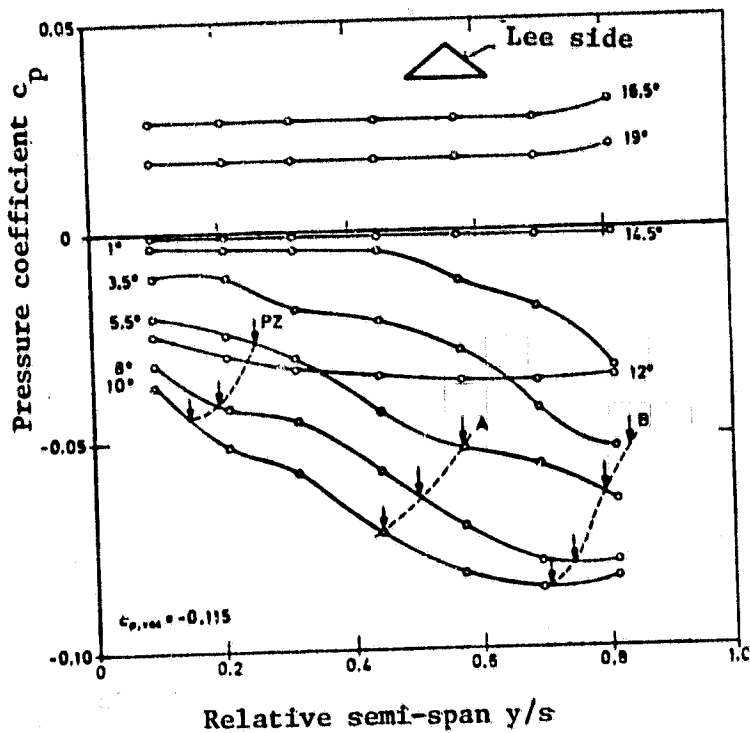
Fig. 39. Pressure coefficients over span for different angles of attack, M_∞ =3.5
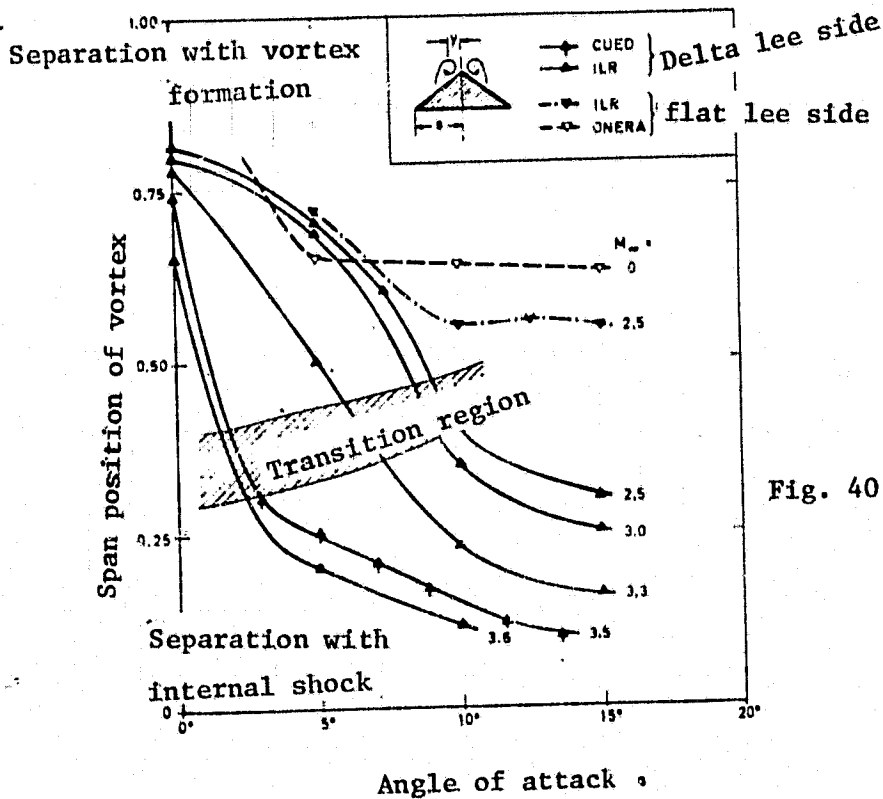
Fig. 40. Position of vortex center as a function of angle of attack.
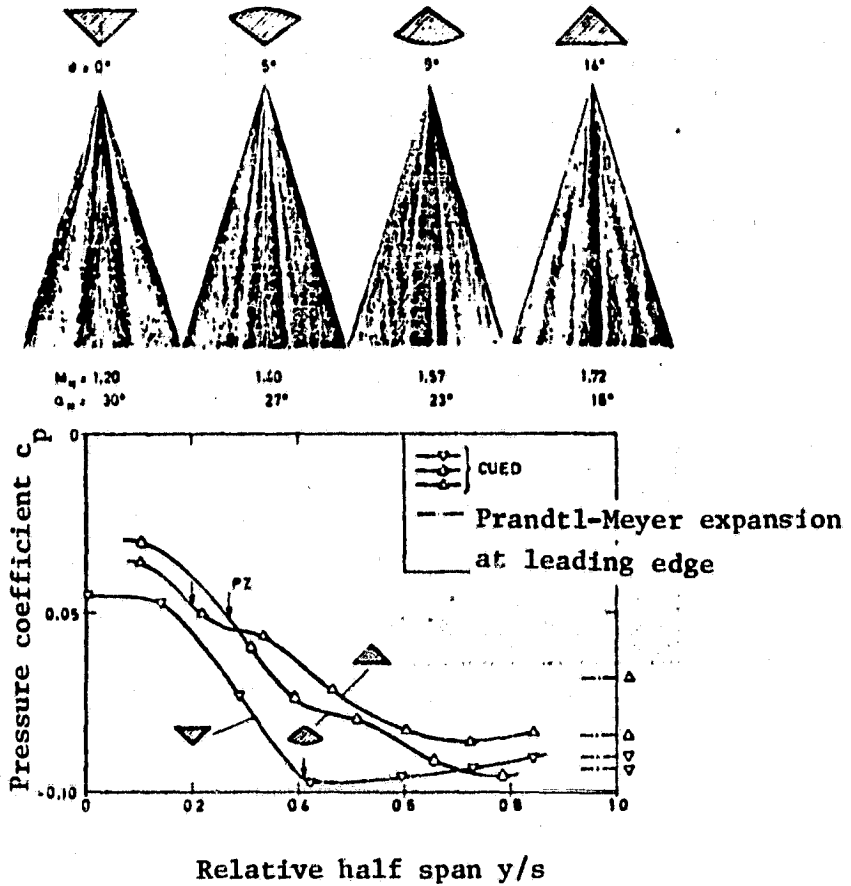
Fig. 41. Oil film photographs and pressure distributions with different
top side shapes and fixed incident flow conditions

$$M_\infty = 3.5 \text{ , } \alpha \sim 10°$$
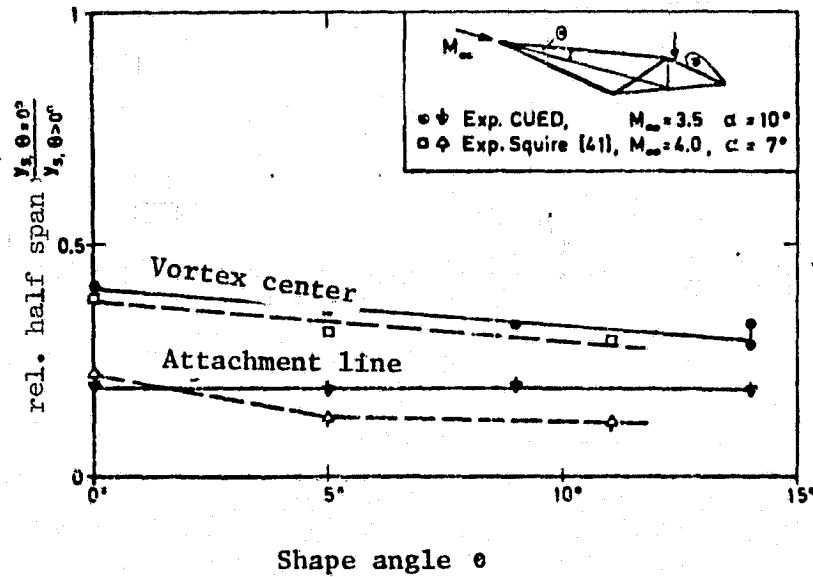
Fig. 42. Position of vortex center and attachment line as a function of
shape parameter Θ'

Olfilm

p^*_{52} ^{42} Shock (separation)
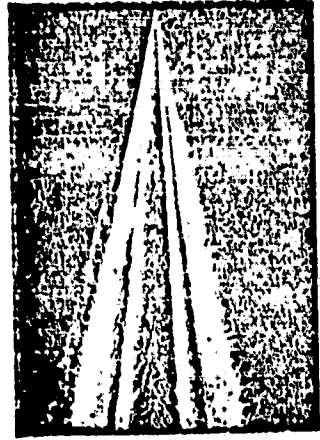
Fig. 43: Influence of extreme leading edge angles for the example of the cone model, $M_\infty = 2.6$

$\alpha = 12°$

$\frac{P_p}{P_{p_\infty}} = const$

Pitot isobars

primary — vortex

secondary — shock

Expansion

stagnation points

Flow model M_N

Lee side

1st measurement
2nd measurement

primary vortex
secondary shock
Expansion

$\alpha = 10°$ M_N

separated flow
(M≥1)
shock
Expansion

$\alpha = 30°$ M_N

$c_{p_{vac}} = 0.1526$

0°
10°
15°
20°
30°
25°

Pressure coefficient c_p

+0.10
+0.05
0
-0.05
-0.10
-0.15

0   0.2   0.4   0.6   0.8   1.0

Rel. semi-span y/s
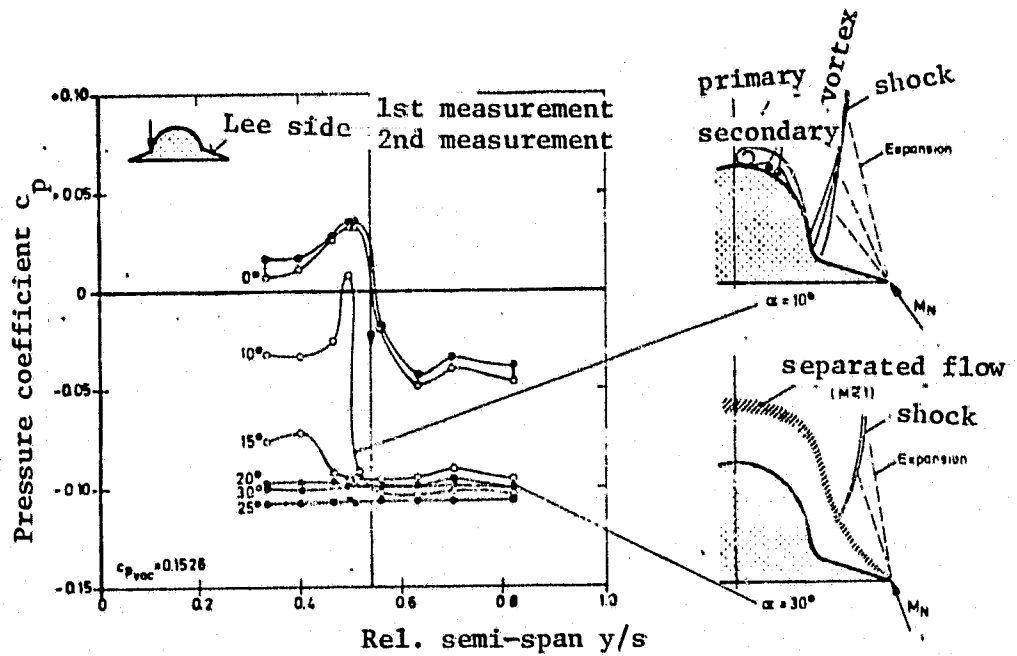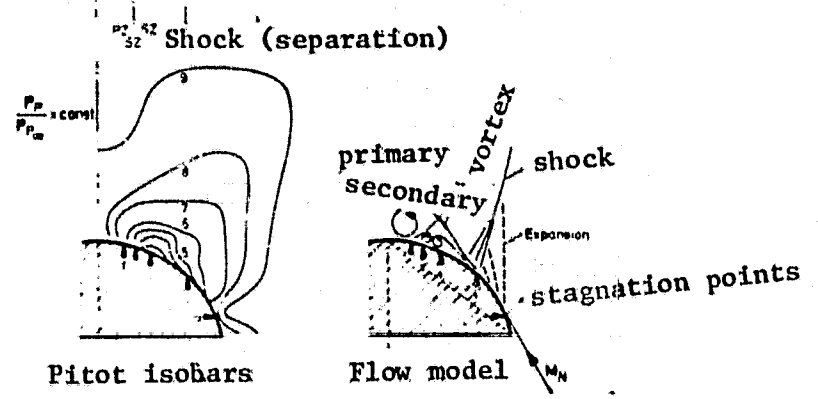
Fig. 44. Flow around the modified cone model shown with pressure distributions and flow models, $M_\infty = 3.06$.

Fig. 45. Comparison of flow fields of two delta wings with identical lee side but different bottom side shape $M_\infty = 2.6$.

Wave rider   Delta model
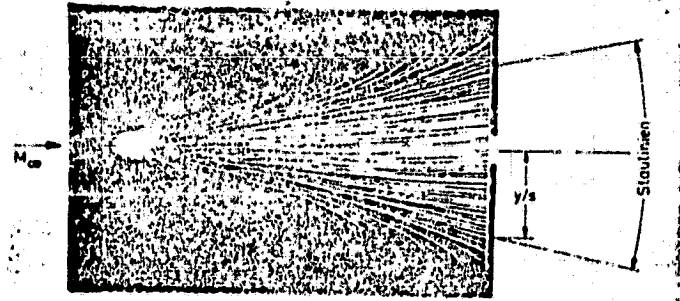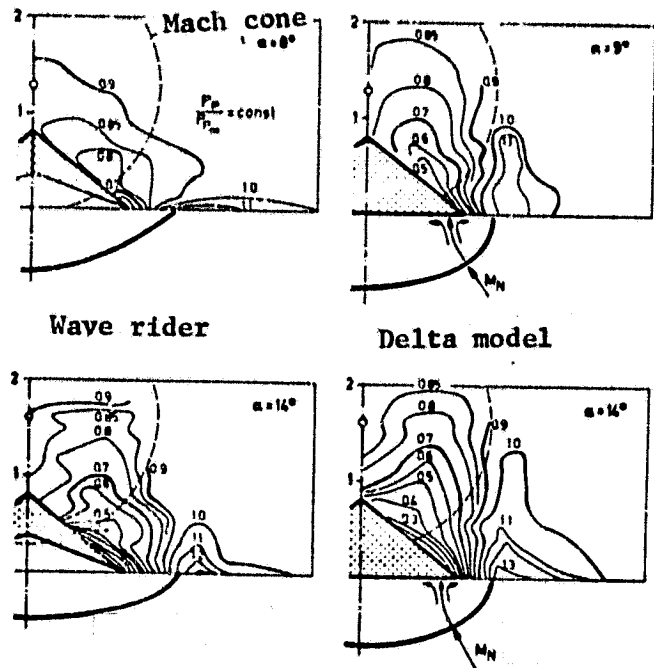
Fig. 46. Position of stagnation lines on the flat pressure side of the delta wing in the region of separation with internal shock.

Leading edge vortex (1 stagnation line)

Separation with internal shock (2 stagnation lines)

Attacned leading edge shock (1 stagnation line)

Mach No. M_∞

141
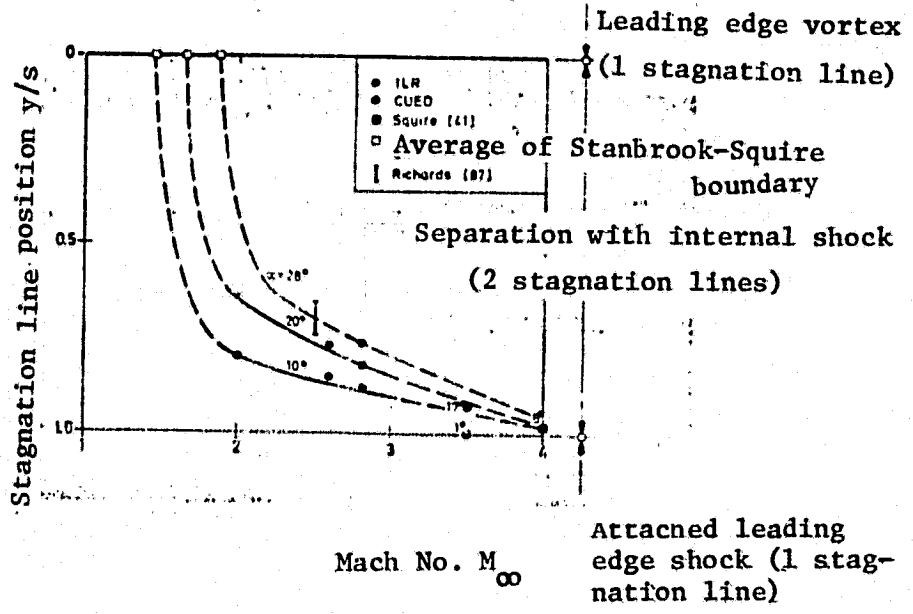
Fig. 47. Vortex intensity as a function of angle of attack, $M_\infty = 3.5$.
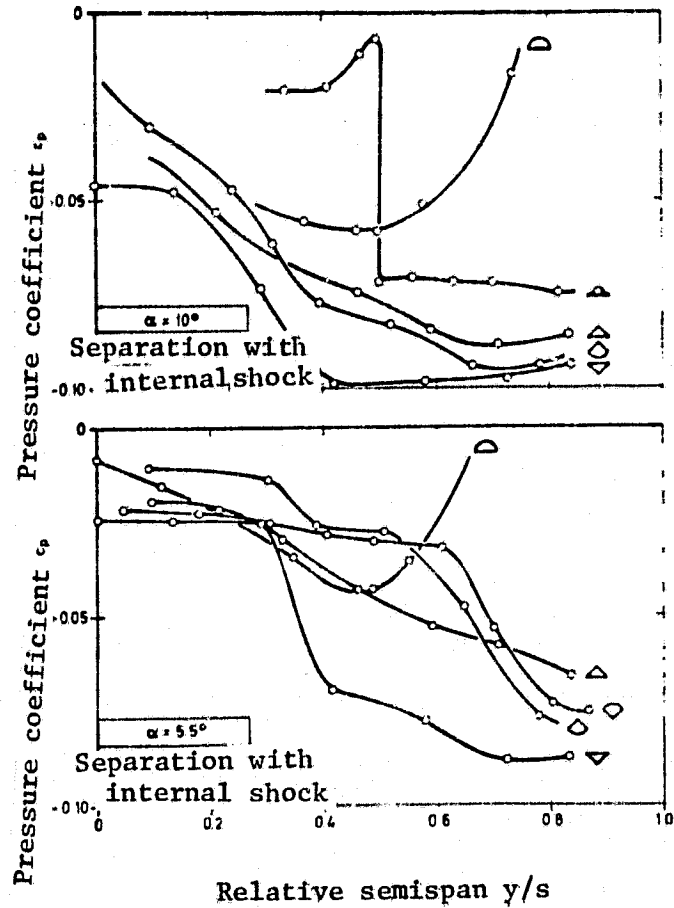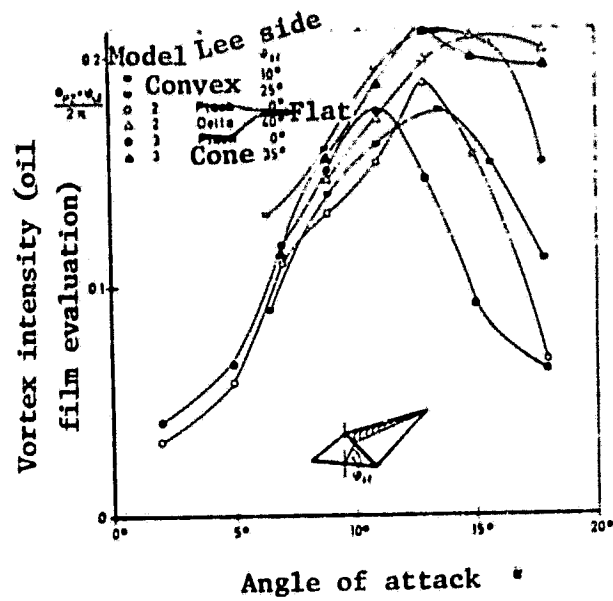
Fig. 48. Comparison of pressure distributions on the lee side with different cross-section shapes, $M_\infty = 3.5$.
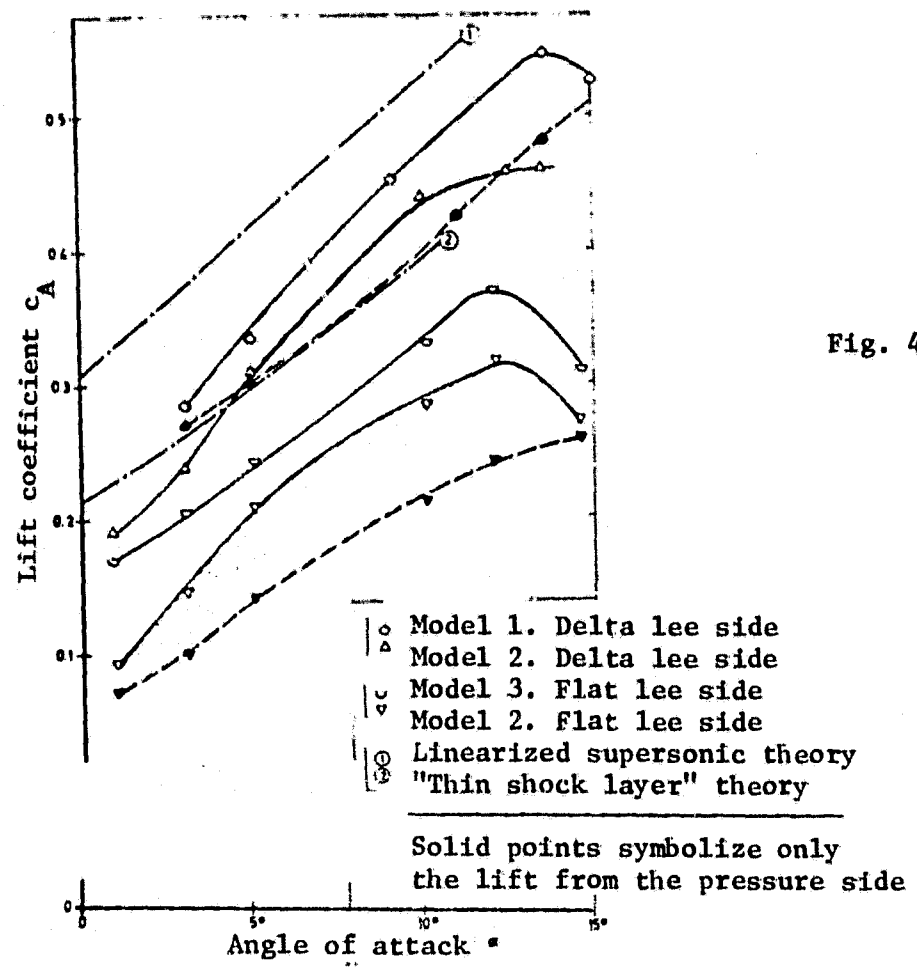
Fig. 49. Lift coefficients of various delta wings, $M_\infty = 3.5$

Legend for Fig. 49:

○	Model 1. Delta lee side
△	Model 2. Delta lee side
∪	Model 3. Flat lee side
▽	Model 2. Flat lee side
⊕	Linearized supersonic theory
⊕	"Thin shock layer" theory

Solid points symbolize only the lift from the pressure side

Height position

Span position

Height & span positions

—○— ILR·meas. [73] ○—○ Brown·Michael [27]
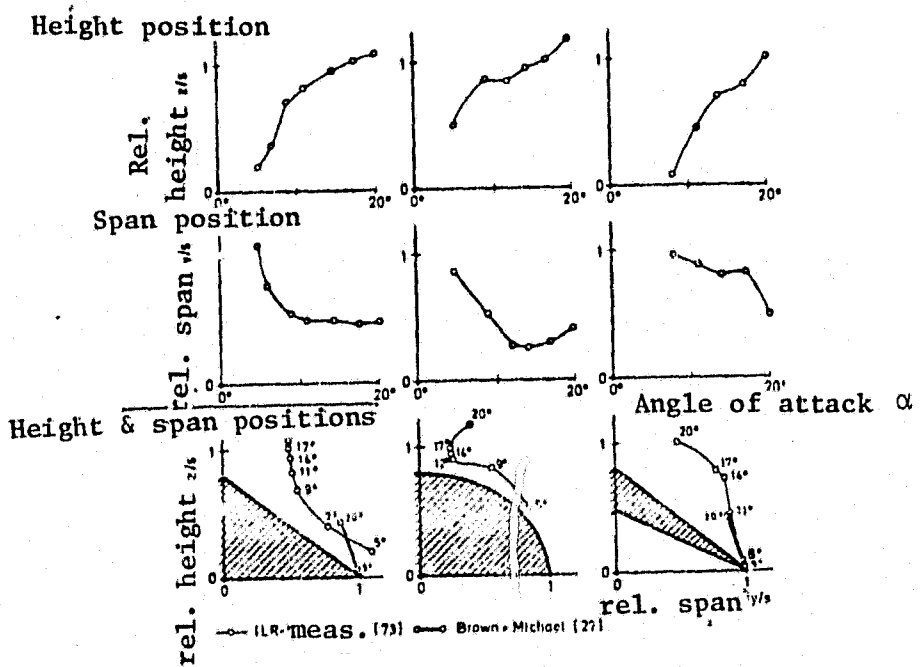
Fig. 50

Position of vortex centers for different delta wings, $M_\infty = 2.6$
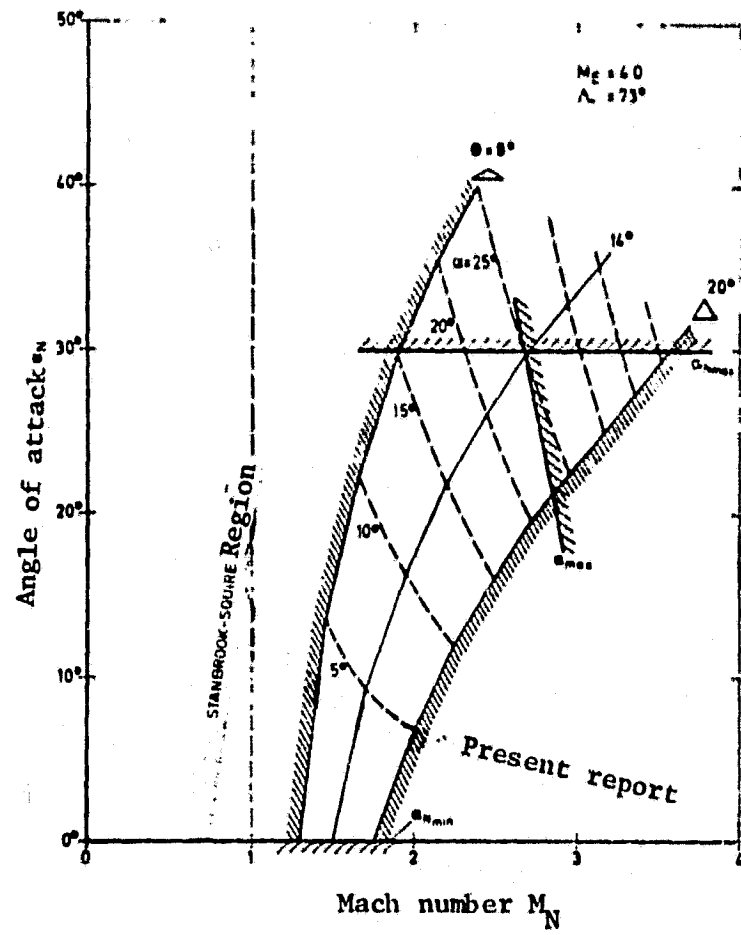
Fig. 51. Restrictions for the design of the top side of a delta wing for cruise flight.
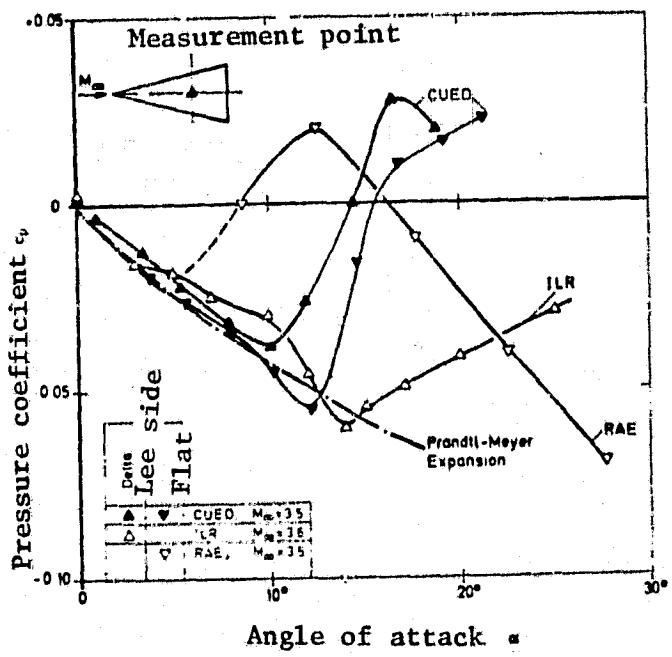
Fig. 52. Pressure coefficients of the symmetry plane as a function of angle of attack for different delta wings,

$$M_{\infty} \sim 3.5$$

Cross-section plane A-A
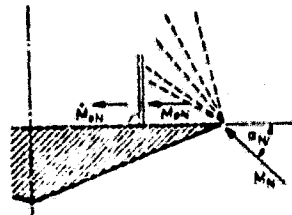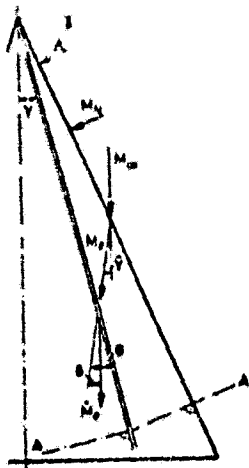
Fig. 53. Geometry of the simplified lee
side flow model.

Leading edge shock

Expansion

Internal shock

Fig. 54. Flow Model

Mach cone
Boundary layer
thickening
Circulation

Internal shock

Expansion

Boundary layer

Base point of internal shock

Leading edge shock

Section A-A

Angle of attack and model values

M_∞, α, Λ, Ψ, γ_i

Leading edge type

Sonic – L.E.

Subsonic – L.E.

Stop

Supersonic L.E.

Leading edge shock

Attached shock

separated shock

Approx. solution for shock position and shape

Flow perpendicular to leading edge

Oblique shock relationships

Approx. solution for boundary layer

$GS = f(M_\infty, \alpha)$

Flow perpendicular to leading edge

Prandtl-Meyer expansion over B.L.

First characteristic, which has to intersect the internal shock

Initial point of internal shock

Iteration of internal shock

Influencing of shock intensity

Boundary layer thickening behind internal shock

Mach number component behind internal shock

Supersonic

Subsonic

Prandtl-Meyer expansion over B.E.

Panel method

Flow components perpendicular to symmetry line

$V_i = 0$

$V_i \neq 0$

Output

Fig. 55. Macro-flow diagram for calculating lee side flow.

146
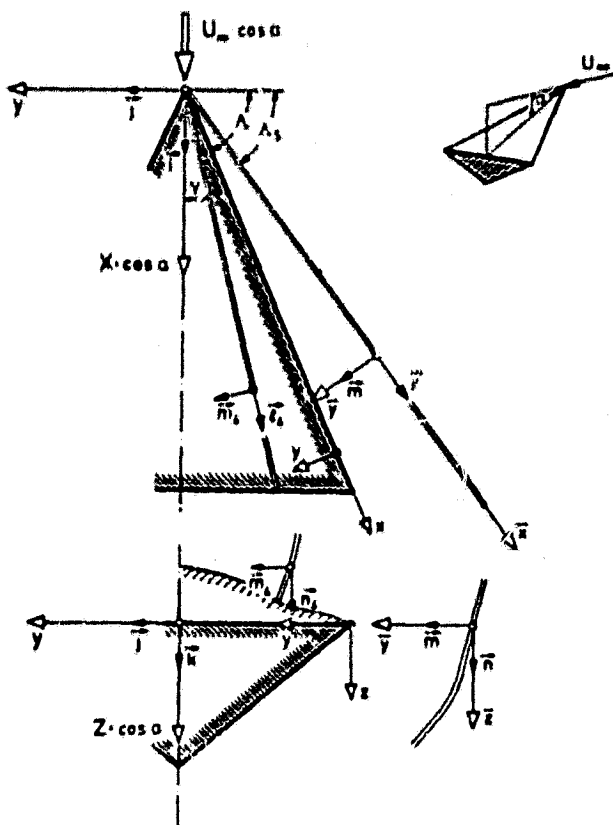
Fig. 56. Coordinates and unit vector system.

Thickness parameter C
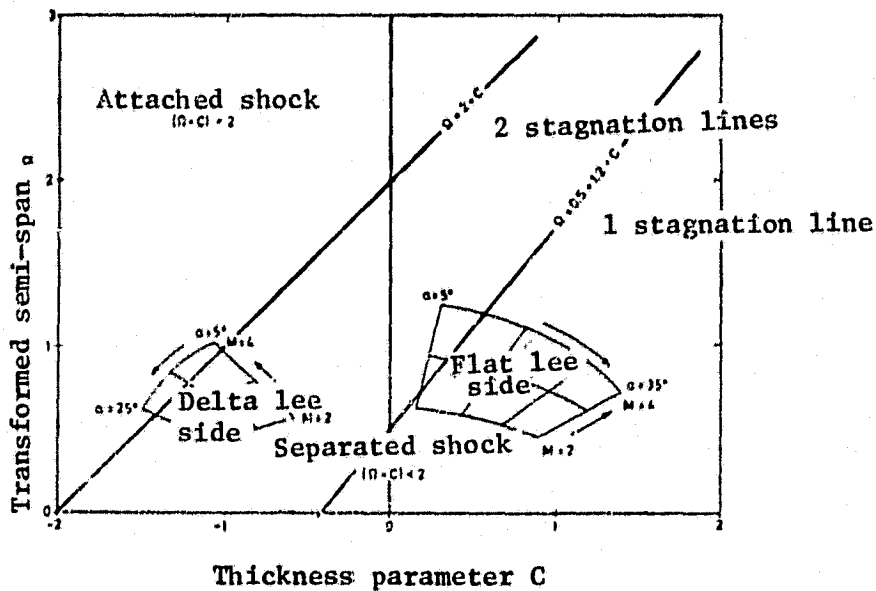
Fig. 57. Flow region represented in the $C = f(\Omega)$ diagram for the "flat delta models."
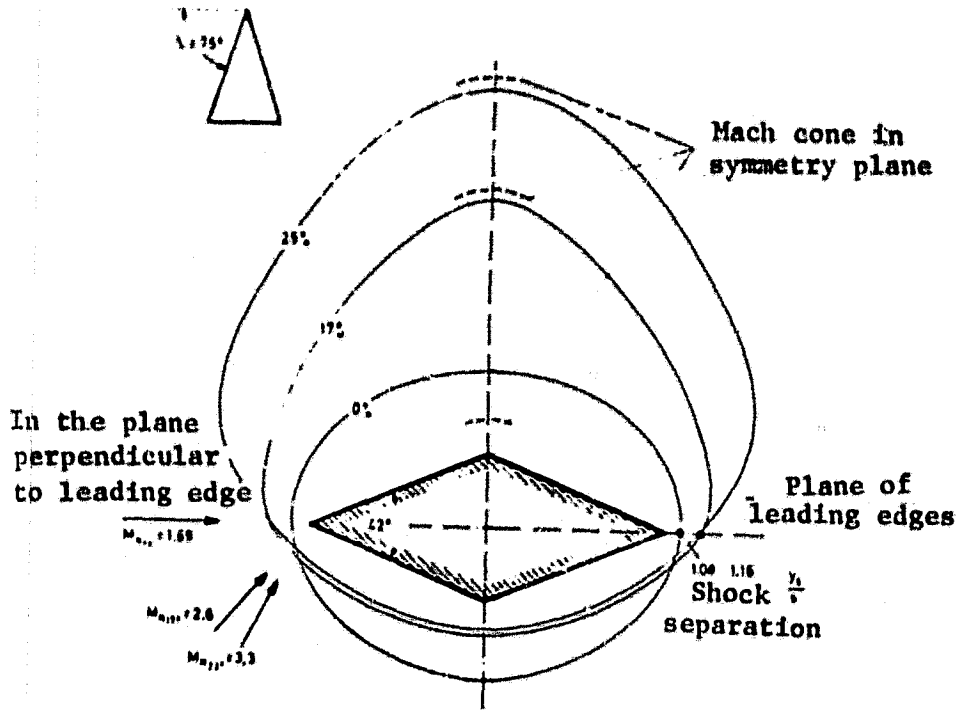
Fig. 58. Leading edge shock profiles for different angles of attack, $M_\infty = 7.0$

Mach cone in symmetry plane

In the plane perpendicular to leading edge

Plane of leading edges

Shock separation

* Measured towards the plane of the leading edges
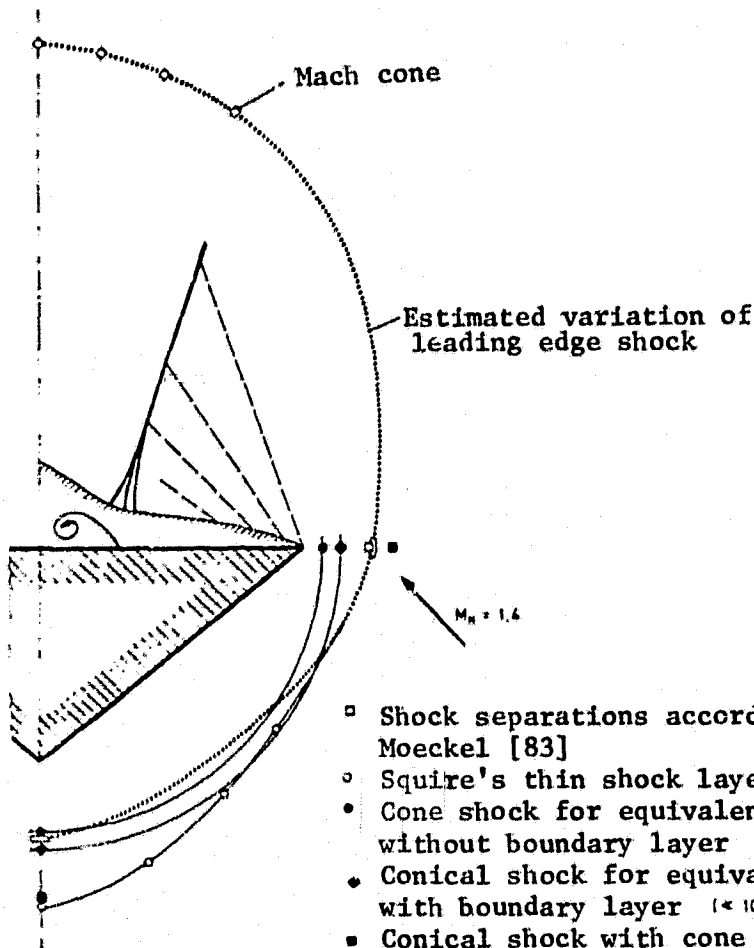
Fig. 59. Profile of leading edge shock compared with different theories, $M_\infty = 3.5$
$\alpha = 15°$

Mach cone

Estimated variation of leading edge shock

□ Shock separations according to: Moeckel [83]
○ Squire's thin shock layer theory (82)
● Cone shock for equivalent rotational body without boundary layer (≃ 9.1°)
◆ Conical shock for equivalent revolution body with boundary layer (≃ 10.5°)
■ Conical shock with cone angle (≃ 14.3°)
▭ Schlieren photographs

/140
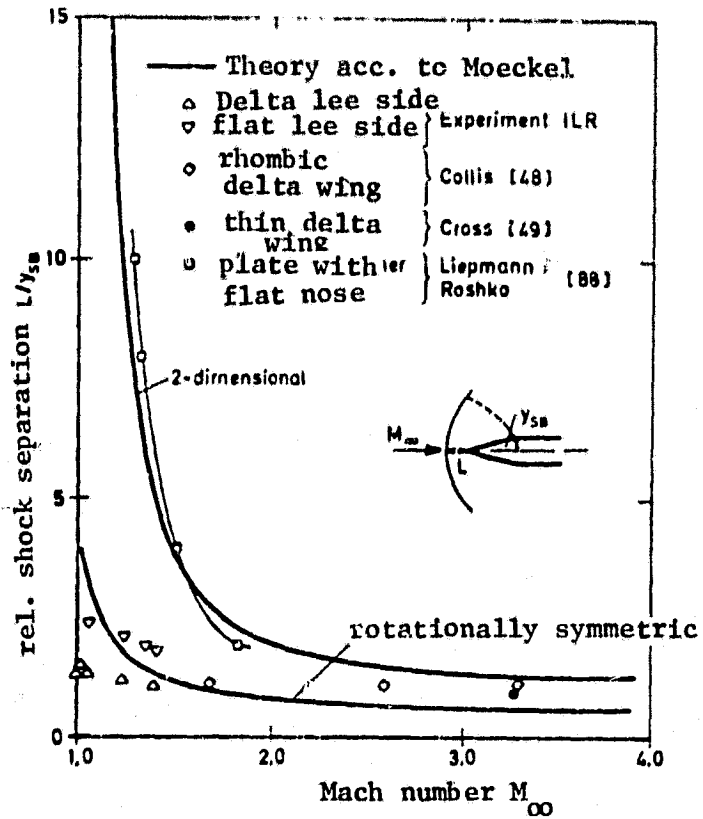
Fig. 60. Separation of the separated leading edge shock as a function of Mach number.
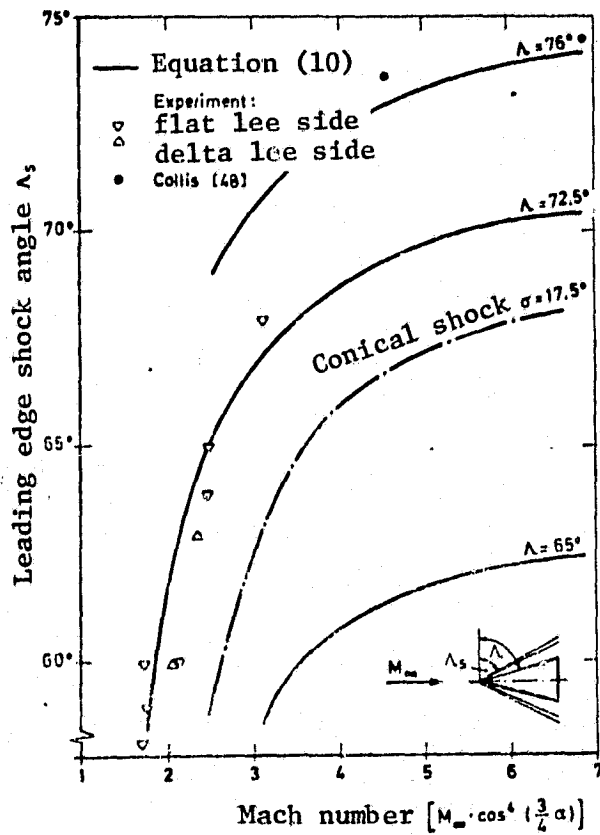
Fig. 61. Angle of leading edge shock as a function of Mach number.

149
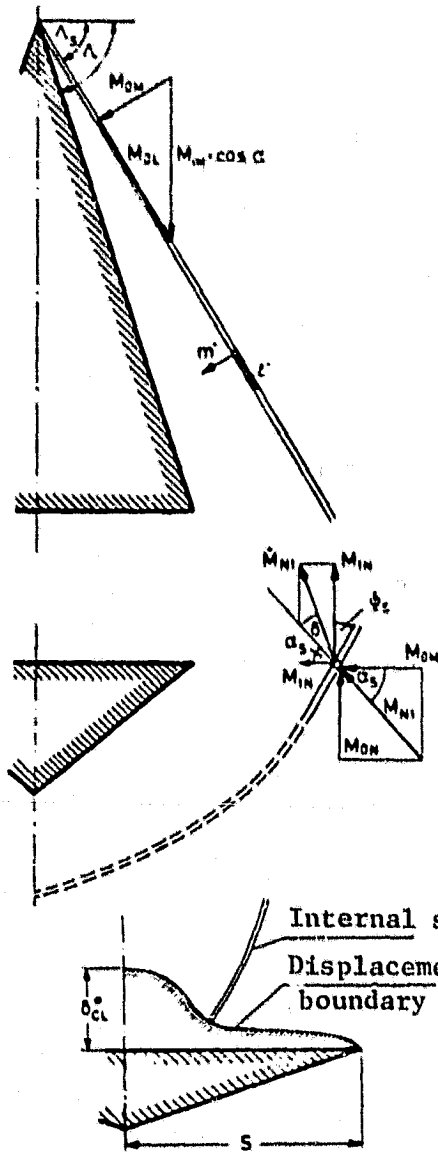
Fig. 62. Geometry for the separated leading edge shock.
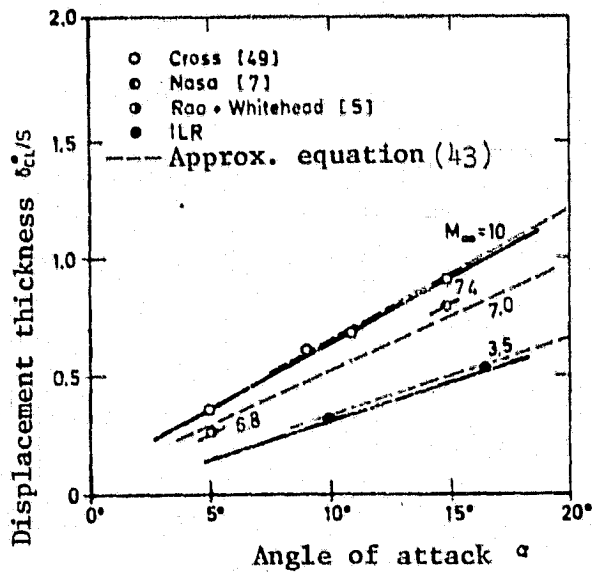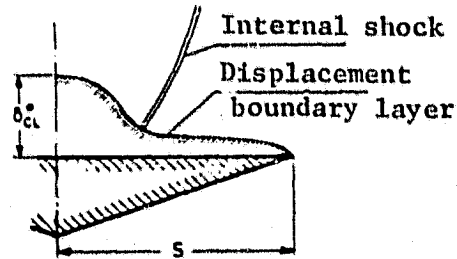
Fig. 63. Thickening of the boundary layer behind the internal shock from various experiments.

150
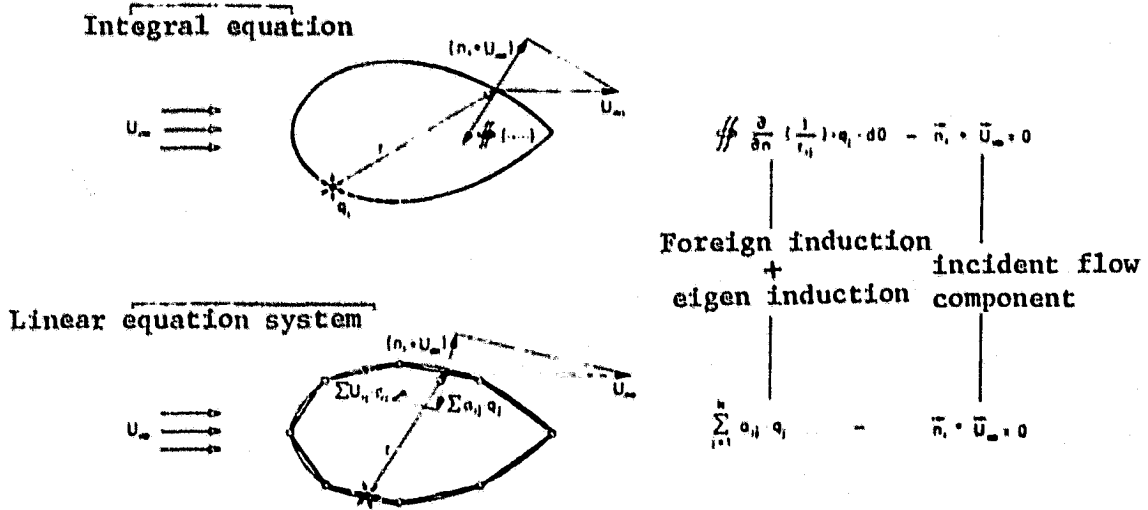
Fig. 64.   Solution of the displacement problem using the Panel method.
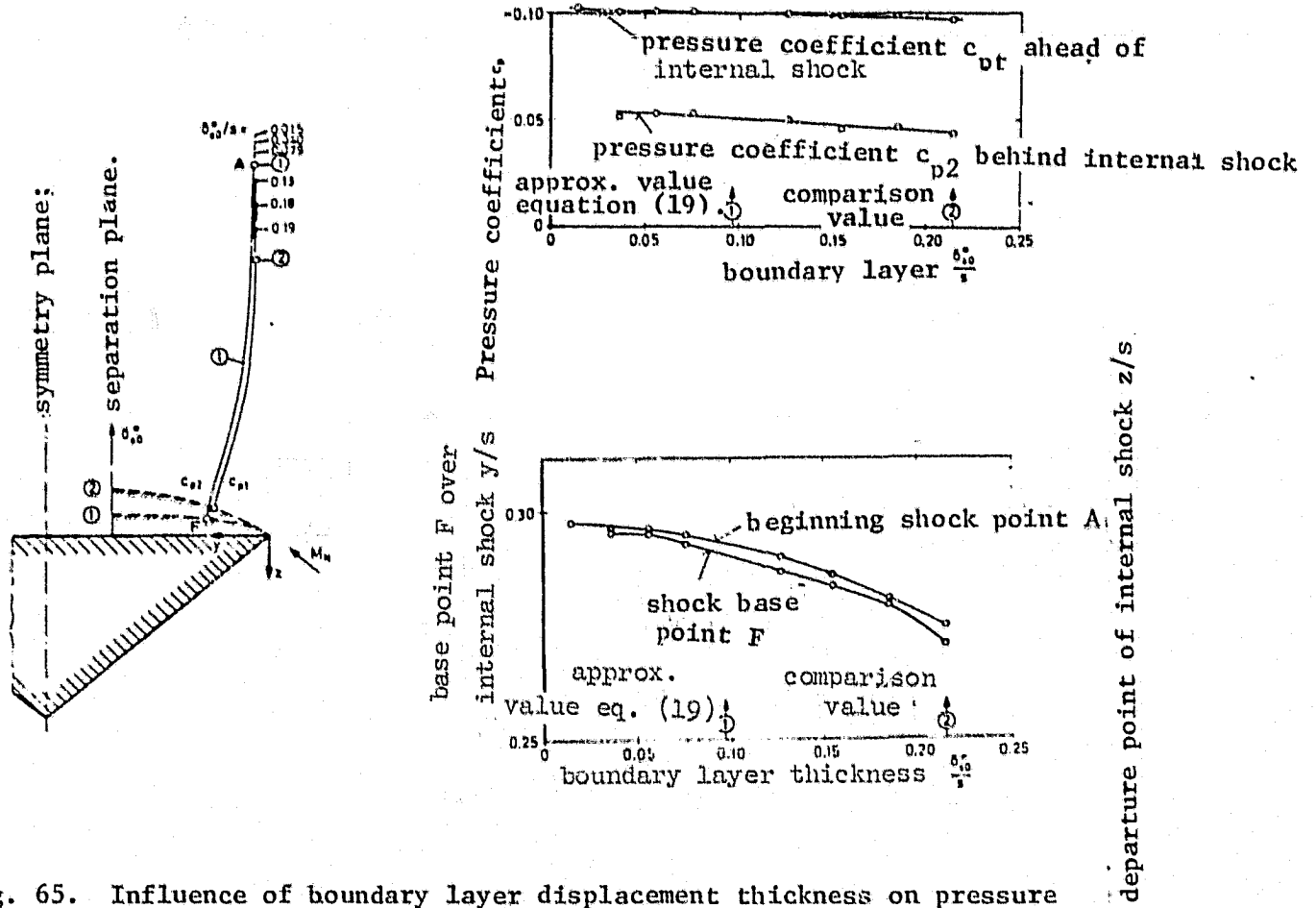
Fig. 65.   Influence of boundary layer displacement thickness on pressure
coefficients and position of internal shock, $M_\infty = 3.55$,
$\alpha = 15°$
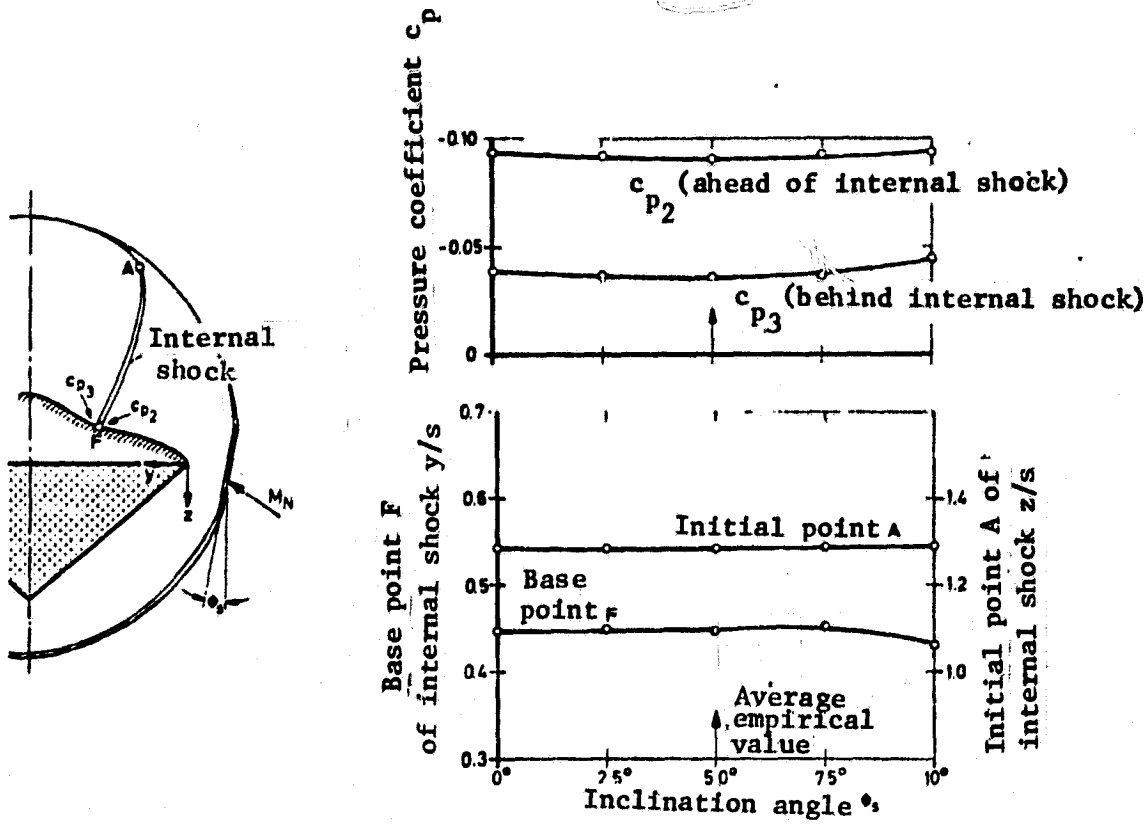
Fig. 66: Influence of inclination angle Φ_s of leading edge shock on pressure coefficients and position of internal shock, $M_\infty = 3.55$, $\alpha = 14.5°$
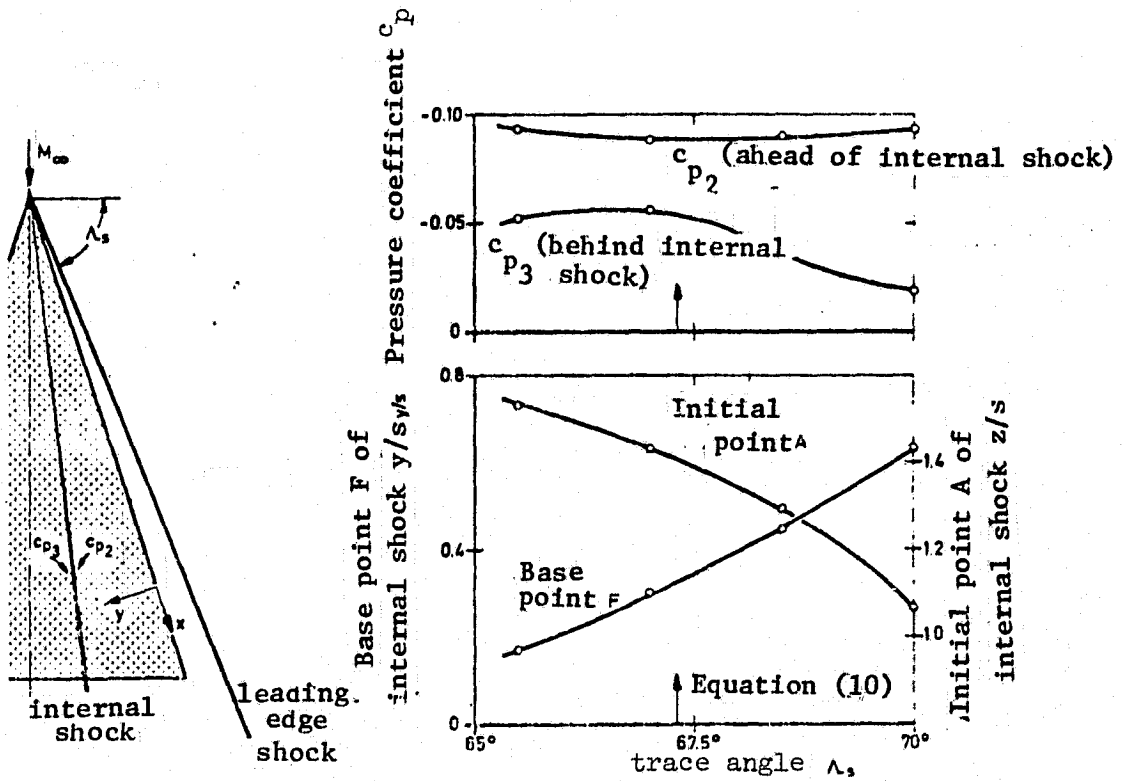
Fig. 67: Influence of trace angle Λ_s of the leading edge shock on pressure coefficients and position of internal shock, $M_\infty = 3.55$, $\alpha = 14.5°$
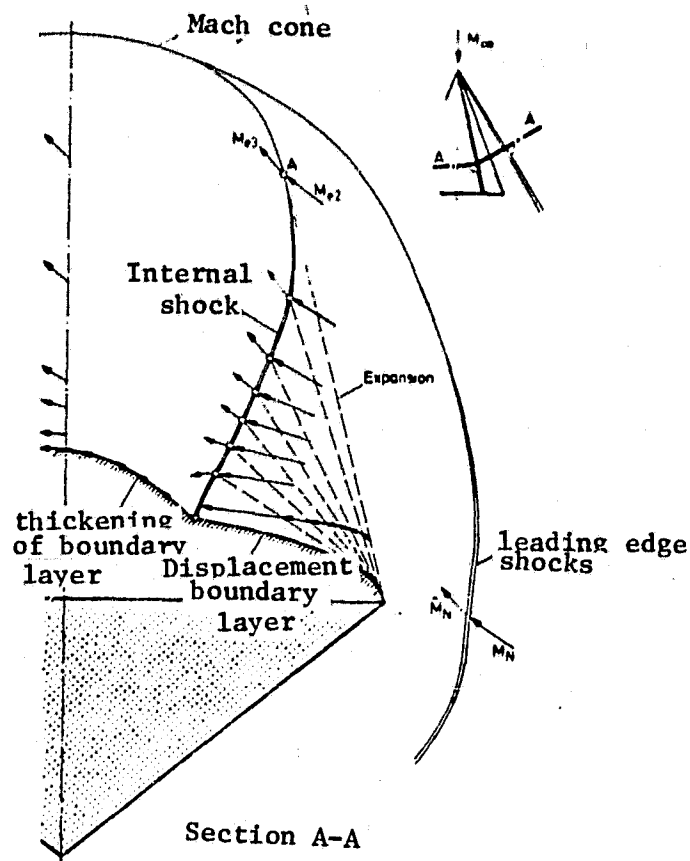
Fig. 68. Theoretically determined flow field on the lee side of the delta wing $M_\infty = 3.55$, $\alpha = 14.5^\circ$, $\Lambda = 72.5^\circ$
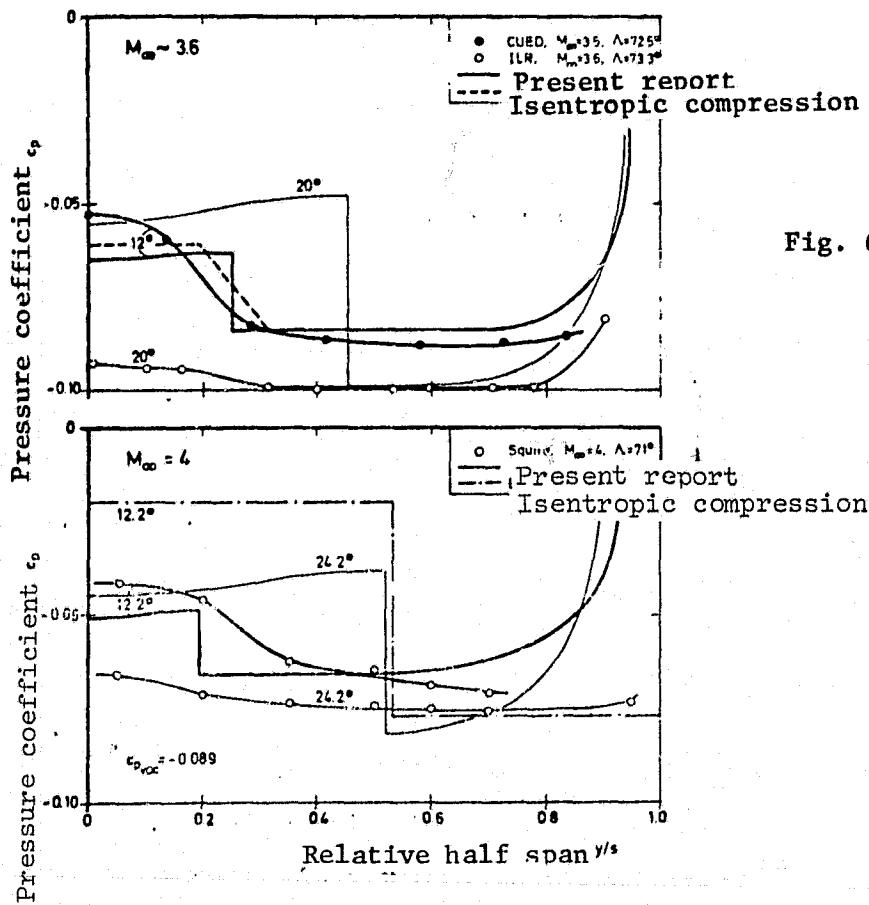

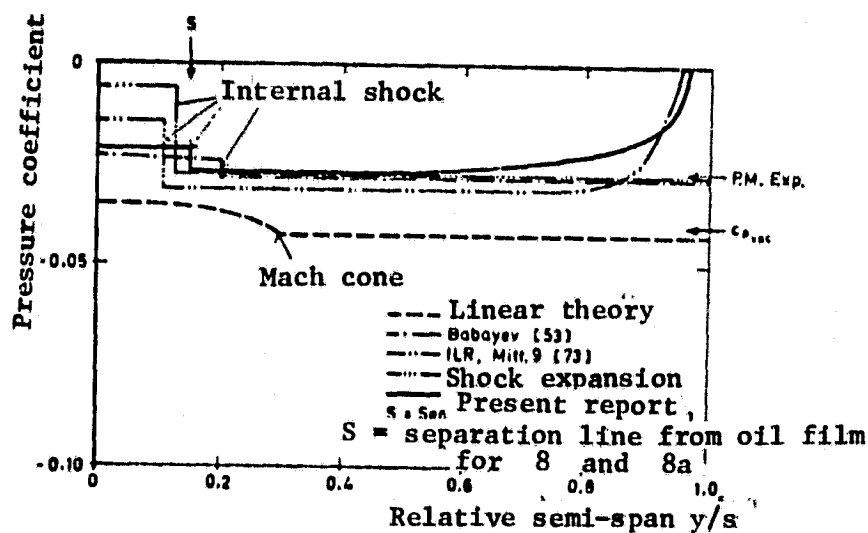Fig. 69. Comparison of theory and experiment: pressure coefficients over the span.

153

Fig. 70. Comparison of lee side theory, $M_\infty = 6.0$,
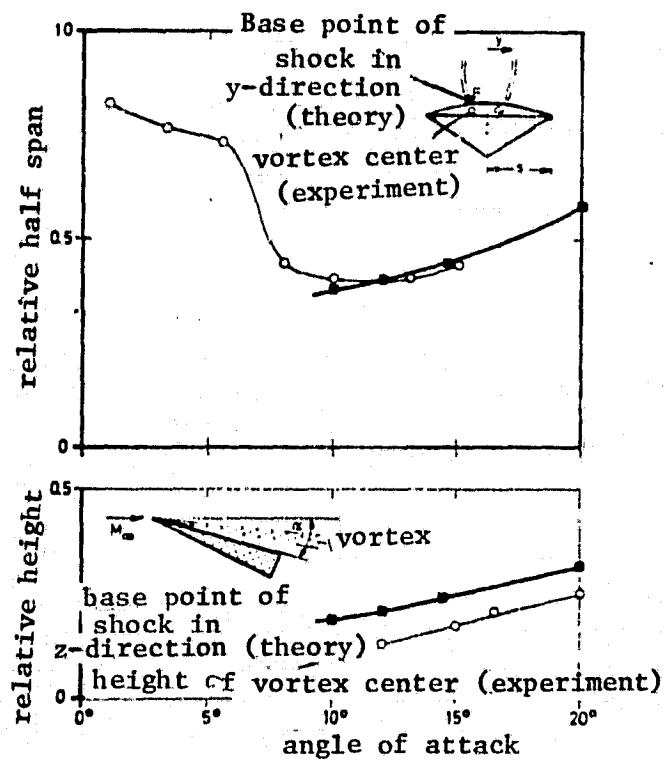sweep angle $\Lambda = 60°$,
angle of attack $\alpha = 7°$

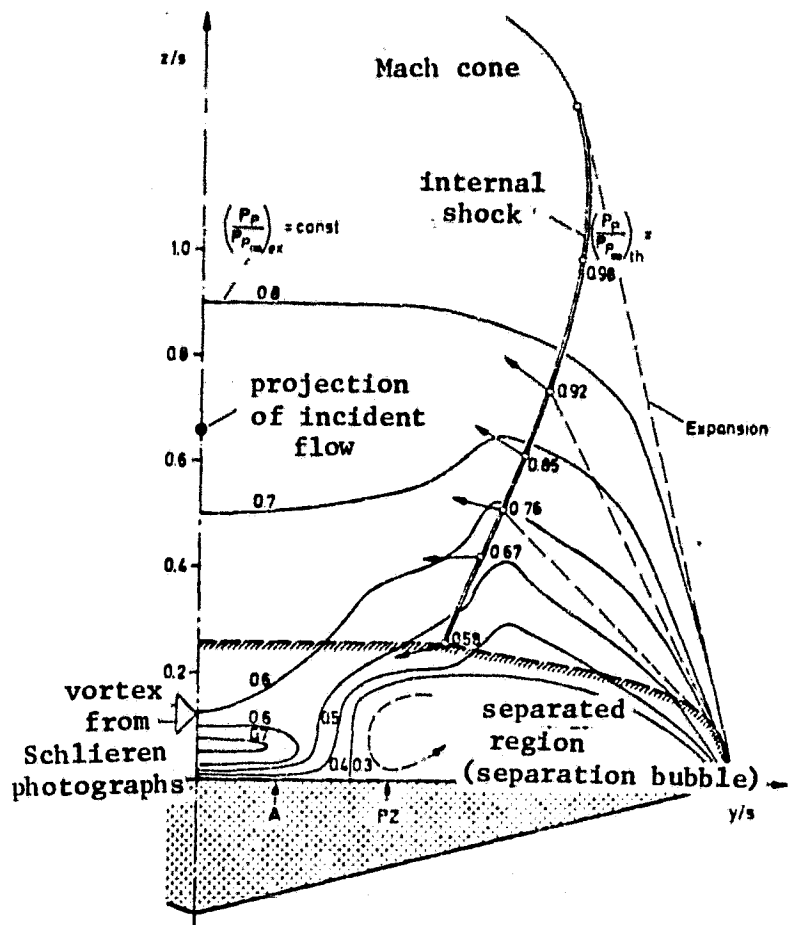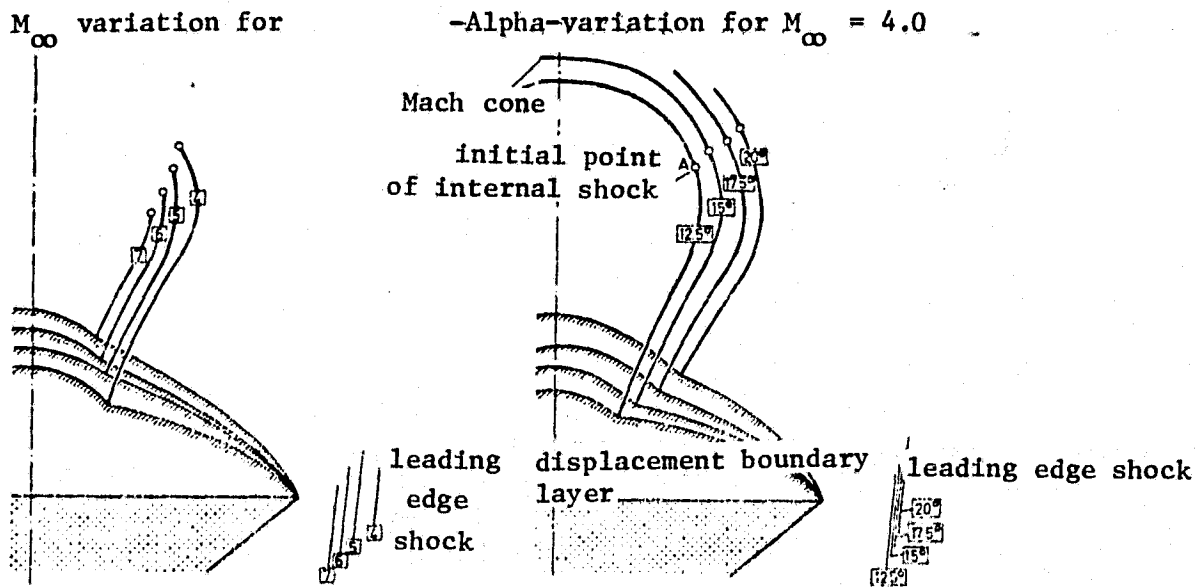Fig. 71. Vortex positions compares with theory and experiment,
$M_\infty = 3.5$, $\Lambda = 72.5$

Fig. 72: Comparison theory - experiment: Pitot isobars measurement of Monnerie and Werla, $M_\infty = 4.0$, $\alpha = 10°$, $\Lambda = 75°$

Fig. 73. Influence of Mach number and angle of attack variation on the flow field of the lee side of delta wings with $\Lambda = 72.5°$

PREVIOUS REPORTS WHICH HAVE BEEN PUBLISHED (ISSN 0341-0587):

1. Johannes Wiedemann, Michael Glahn: Disc or membrane with a
    hole and applied plaster with stress in all directions
    (Berlin 1974), ISBN 37983 0531 5.

2. Manfred Ziegner: Theoretical and experimental investigation
    of the aerothermodynamic monitoring of aviation jet engines
    (Berlin 1974), ISBN 3 7983 0532 3.

3. Joachim Wernicke: Experimental investigations of a new digital
    angular actuator (Berlin 1974), ISBN 3 7983 0535 8.

4. Klaus-Dieter Pautz: Air tolerant actuators (Berlin 1974),
    ISBN 3 7953 0539 0.

5. Klaus Hünecke: A calculation method for separated flow over
    slender sweptback wings (Berlin 1974), ISBN 3 7983 0541 2.

6. Dieter Dey, Uwe Kirchhoff: Description possibilities for
    multiple variable regulation properties of human beings for
    vehicle driving (Berlin 1975), ISBN 3 7983 0547 1.

7. Michael Glahn: Influences of viscoelasticity on adhesive com-
    pounds (Berlin 1975), ISBN 3 7983 0545 5.

8. Robert Gasch: A contribution for the treatment of the dynamic
    behavior of a rotating shaft with a notched cross-section
    (Berlin 1975, ISBN 3 7983 0551 X.

9. Separation and wind feedback of radial wall jets (Berlin 1975),
    ISBN 3 7983 0552 8.

10. Frank Köhler: A semi-analytical approximation method for de-
    termining the unsteady temperatures in skin-step compounds
    (Berlin 1975), ISBN 3 7983 0553 6.

11. Klaus Knothe/Walter Kik: LINDA 1 - A program system for in-
    vestigating the dynamic behavior of track vehicles (Berlin
    1976), ISBN 3 7983 0560 9.

12. Wolfgang Holzapfel. Laser devices and optoelectrical systems
    in flight control and satellite technology (Berlin 1976),
    ISBN 3 7983 0561.

13. Christoph Haberland, Frank Köhler. Semi-analytical calculation
    of unsteady temperatures in skin step compounds for arbitrary
    heating over time (Berlin 1976), ISBN 3 7983 0562 5.

14. Leonidas Kamarinopoulos. Application of Monte Carlo methods
    for determining liability characteristics of technical systems
    (Berlin 1975), ISBN 3 7983 0563 3.

15. Johannes Wiedemann, Curt Kranz: Effects of an adhesive plaster on notch stress intensity and dynamic strength of a disc with a notch (Berlin 1976), ISBN 3 7983 0567 6.

16. Christoph Haberland, Frank Köhler. Calculation of unsteady thermal stresses in skin-step units for heating limited in time (Berlin 1976), ISBN 3 7983 0568 4.

17. Alfred Hofler. Form optimal light construction frames by using an evolution strategy (Berlin 1976), ISBN 3 7983 0569 2.

18. Hans-Jürgen Deeg. Theoretical an experimental investigations of pressure shafts in gas-solid flows (Berlin 1976), ISBN 3 7983 0571 4.

19. Joseph Sternberg. Investigations of crack propagation and crack strength in sheet metal made of Al Cu Mg 1 and Al Zn Mg Cu 1.5 with dynamic bending stress (Berlin 1977), ISBN 3 7983 0584 6.

20. Klaus D. Kricke. The situation of air traffic compared to ground vehicles with special consideration of energy problems (Berlin 1977), ISBN 3 7983 0588 9.

21. Hans J. Sternfeld. Performance and heat transport of high-energy rocket engines with thrust variation (Berlin 1977), ISBN 3 7983 0590 0.

22. Christoph Haberland, Wolfgang Nitsche. Investigations of the influence of a hydrodynamic starting section on the heat transfer to flat channel walls (Berlin 1977), ISBN 3 7983 0591 9.